University of Naples Federico II
Polytechnic and Basic Sciences School

Department of Chemical Sciences

Ph.D. in Chemical Sciences

G-quadruplex-forming aptamers for diagnostics and theranostics in anticancer strategies

PhD student:
Dr. Ettore Napolitano

Advisor
Prof. Daniela Montesarchio

Examiner
Prof. Luigi Petraccone

XXXV Cycle 2019-2022
Coordinator: prof. Angela Lombardi

“Se ho visto lontano è perché sono salito sulle spalle dei Giganti”
(Isaac Newton)

Contents

Summary

In this PhD thesis, I focused on the development of innovative tools based on G-quadruplex forming oligonucleotide aptamers recognizing specific proteic markers for early detection and treatment of tumours and/or inflammations.

In the first part of this work, I investigated V7t1 and 3R02, two G-quadruplex forming aptamers well known to recognize the Vascular Endothelial Growth Factor 165 ($VEGF_{165}$) – an angiogenic protein, overexpressed in cancer cells, involved in growth and metastases of solid tumours – in their interaction with a novel cyanine dye, designed as an analogue of thiazole orange, here named CyOH. With an in-depth biophysical analysis comprising techniques like gel electrophoresis, circular dichroism (CD), UV-vis and fluorescence spectroscopy, I demonstrated that CyOH was able to interact with the two selected aptamers, giving in both cases a marked fluorescence light-up exclusively when bound to their dimeric forms. Interestingly, both V7t1 and 3R02 recognized $VEGF_{165}$ with higher affinity in the conditions that allowed them structuring into dimeric G-quadruplexes, *i.e.* after simple dilution in a Na^+-rich pseudo-physiological buffer, mimicking the extracellular environment, without any thermal treatment. Moreover, the fluorescent light-up of the probe was unaltered when the dimeric aptamer-CyOH complexes bound to the target protein. These complexes, tested on MCF-7 cancer cells using non-tumorigenic MCF-10A cells as control, showed an efficient internalization and colocalization with a fluorescently-labelled anti-VEGF-A antibody, which allowed both recognition and detection of the target. Our experiments clearly showed the potential of the studied systems as tools for anticancer theranostic strategies, combining the therapeutic potential of the G-

quadruplex forming anti-VEGF aptamers with the diagnostic efficacy of the selective fluorescence light-up produced by CyOH. Novel V7t1 modified aptamers carrying pyridine-containing ligandosides were also synthesized with the aim of favouring the VEGF recognition after metal-induced dimerization. Biophysical characterization was carried out, obtaining preliminary results. However, a deeper analysis will be necessary to find the best conditions to reach the set goal.

In the second part of the thesis, I focused on the development of aptameric systems selective for High-Mobility Group Box 1 (HMGB1), a cytokine involved in the pathogenesis of various inflammatory and immune diseases, as well as cancer. In the search for novel, effective anti-HMGB1 aptamers, we relied on the SELEX (Systematic Evaluation of Ligands by EXponential enrichment) technology, identifying 14 G-quadruplex forming aptamers from a properly designed library of guanine-rich oligonucleotides. By using UV-vis spectroscopy, CD, gel electrophoresis and size exclusion chromatography techniques, we demonstrated that the selected sequences, in pseudo-physiological conditions mimicking the extracellular environment, were able to fold into stable G-quadruplex structures, showing high polymorphism both in terms of G-quadruplex topology (parallel and hybrid G-quadruplex conformations typically coexist) and molecularity (both monomeric and dimeric species were found). In properly designed binding assays, some of these oligonucleotides showed very high affinity against the target HMGB1. Moreover, *in vitro* cellular assays on NIH3T3 fibroblasts showed, for these aptamers, an ability to inhibit the protein-induced cell migration directly related to their affinity for the target protein. Interestingly, in accordance with the findings obtained in the first part of this thesis, the best conditions for protein inhibition were the ones allowing the aptamers to adopt dimeric G-

quadruplexes, *i.e.* dilution in a Na^+-rich pseudo-physiological buffer without any thermal treatment. This is particularly interesting because it goes against the dogma of the "annealing procedure" typically used in literature to let the aptamers correctly fold into the specific three-dimensional shape for target interaction. Particularly valuable were the results obtained on the so-called L12 aptamer, whose dimeric form proved to be very active as HMGB1 inhibitor in chemotaxis assays (IC_{50} values in the low nM range), providing a useful lead candidate for future *in vivo* studies.

Chapter 1-Introduction

1.1 Main structural features of G-quadruplexes

For many decades, DNA was generally considered as a uniform right-handed double helix, built of AT and GC base pairs, as was originally discovered by Watson and Crick (1), called B-form. It was later found that DNA can adopt, in addition to the major B-form, many other structures involved in critical physiological processes (2), including the left-handed Z-DNA, various kinds of hairpins and slipped structures, parallel-stranded double helixes, various kinds of triplexes, guanine quadruplexes, intercalated cytosine tetraplexes and other less well characterized structures, overall identified as non-canonical DNA structures (3). DNA is a dynamic molecule, whose structure depends on the underlying nucleotide sequence and is influenced by the environment and the overall DNA topology. In particular, it has been established that non-canonical DNA structures formation occurs in particular during replication and transcription, which involve DNA unwinding and formation of single tracts (2). Furthermore, DNA secondary structures can regulate gene expression, interactions with proteins and have an impact on genomic stability, DNA repair and damages (4). Many of these non-canonical structures have shown their correlation with diseases like cancer and genetic disorders, hence making them an extremely striking target for structure-selective drug design and therapeutic application.

G-quadruplexes (G4s) play a major role in this context due to their distinctive structural characteristics and crucial functions in fundamental physiological processes. G4s are non-canonical nucleic acid structures formed by single stranded guanine (G)-rich DNA or RNA sequences, such as telomeric nucleic acids at linear chromosome ends. G4s comprise two or more stacks of G-quartets, which are square planar structures formed by four guanine bases

through Hoogsteen hydrogen bonding (5, 6). A typical unimolecular G4-forming sequence has four or more G-rich tracts connected by several loop sequences, including from one to typically seven nucleotides, which can be defined as 5'-$GGGN_{1-7}GGGN_{1-7}GGGN_{1-7}GGG$-3' (for three stacks of G-quartets). G4 structures are stabilized by monovalent cations, such as K^+ and Na^+ (7, 8), which neutralize the electrostatic repulsion of the negative charges of the oligonucleotide backbones both by forming tight ion pairs with the phosphates and, even more distinctly, by binding the oxygens at 6 position of the guanines in the internal channel formed by the stacked G-quartets (Figure 1).

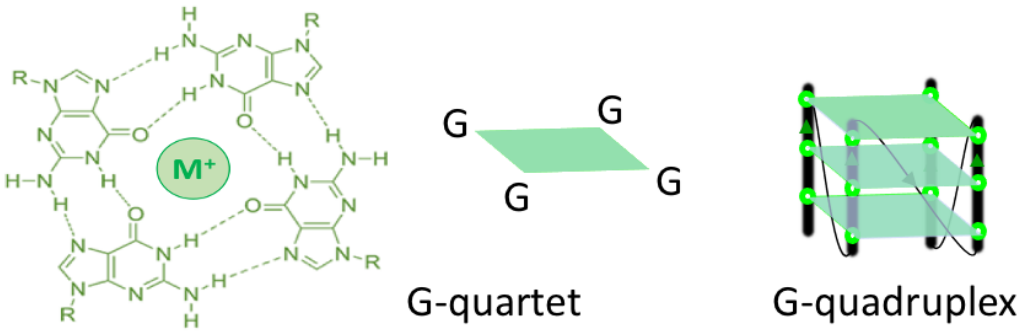

Figure 1. Structure of a G-quartet and of a monomolecular G-quadruplex.

G4s are widely polymorphic, since they can be formed by one, two, or four separate strands of DNA or RNA (9) (Figure 2).

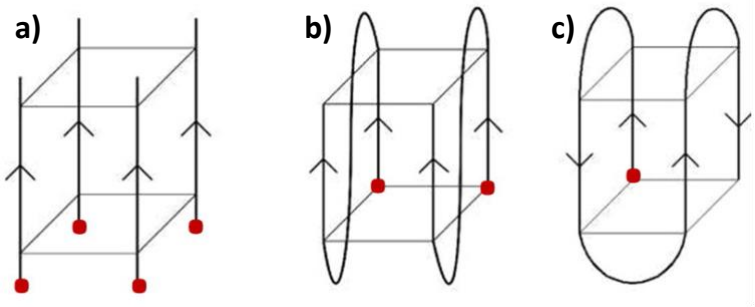

Figure 2. Schematic representation of: a) tetramolecular, b) bimolecular, c) monomolecular G-quadruplex structures (adapted from (10)).

From a topological point of view, G4s can be classified into three main classes: 1) parallel, with all four strands oriented in the same direction; 2) antiparallel, with two strands pointing in the same direction and other two in the opposite one; 3) hybrid, with three oligonucleotide sequences oriented in the same direction (11) (Figure 3).

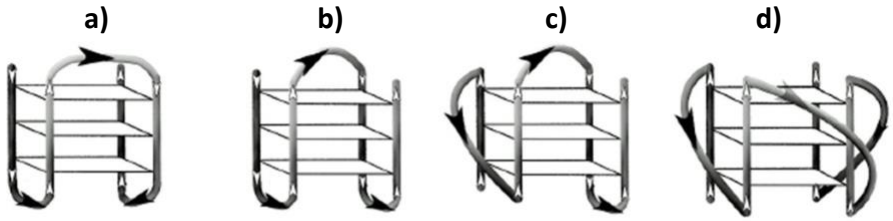

Figure 3. Schematic representation of: a) antiparallel (chair-type), b) antiparallel (basket-type), c) hybrid, d) parallel G-quadruplex topologies (adapted from (10)).

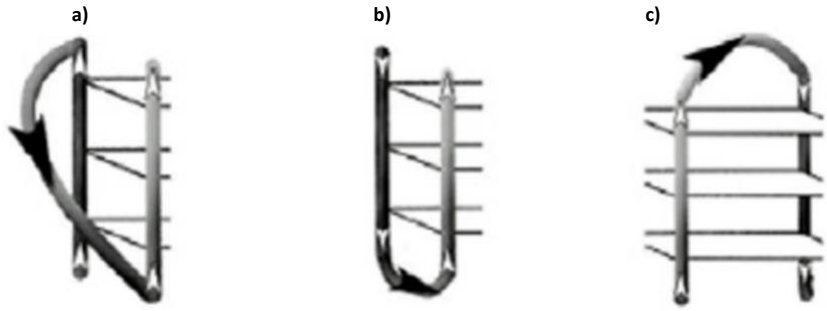

Figure 4. Linking loops in G-quadruplex structures: A) propeller, B) lateral and C) diagonal (adapted from (11)).

Moreover, each topology differs in loop size and sequence. Loops can be defined as the nucleotide sequences connecting the different tetrads and can be distinguished into three main classes: propeller, lateral and diagonal (12). Propeller-type loops are found in parallel intramolecular G4 structures, which require a loop that connects the bottom G-tetrad with the top one (Figure 4a). Antiparallel G4s, in addition to propeller-type loops, include also lateral (or edgewise) loops (Figure 4b), which link adjacent guanine-rich strands. Two loops of this type can be located both at the same and opposite poles of the molecule, corresponding to the "head-to-head" or "head-to-tail" arrangement in bimolecular G4 complexes. Finally, diagonal loops are those connecting opposite guanine-rich strands (Figure 4c) (13). The thermodynamic stability of G4s strongly depends on their topology (14) and number of G-tetrads, but also on the loop size and base composition (15). A further structural element relevant for the G4 folding is the conformation adopted by the guanines, which can be *syn* or *anti* with respect to the *N*-glycosidic bond (16) (Figure 5).

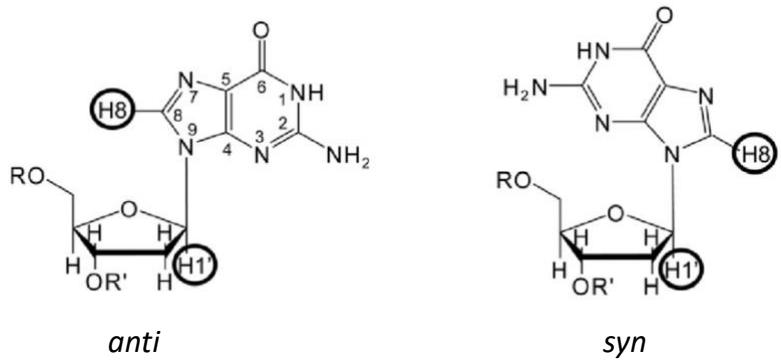

Figure 5. Guanine *anti* and *syn* conformations with respect to the *N*-glycosidic bond.

Interestingly, while in B-DNA nucleobases adopt only the *anti* conformation, in G4 structures guanines can adopt either *syn* or *anti* conformation. This gives rise to a variety of different arrangements within the G-tetrads, which sensibly contribute to increase the topological diversity of G4s (17). G4 topology and stability are strictly associated with metal cations. Several metal cations with different radii can be hosted in the central cavity of a G4 structure. Circular dichroism (CD) studies revealed that cations with ionic radii between 1.3 and 1.5 Å, such as K^+, Rb^+, NH_4^+, Sr^{2+} and Ba^{2+}, stabilize the G4s better than other ions, such as Li^+, Na^+, Cs^+, Mg^{2+} and Ca^{2+}, due to the optimal fit between two adjacent G-tetrads coordinating eight guanine carbonyl oxygens (18) (Figure 6). Smaller cations, such as Li^+, or larger cations, such as Cs^+, do not fit well within two consecutive G-tetrads (18). The general ranking of G4 stabilization by cations is $Sr^{2+} > Ba^{2+} > K^+ > Ca^{2+} > Na^+, NH_4^+, Rb^+ > Mg^{2+} > Li^+ \geq Cs^+$ (19). Notably, if G4s and monovalent cation concentrations are low enough, some divalent cations, such as Ca^{2+}, Co^{2+}, Mn^{2+}, Zn^{2+}, Ni^{2+} and Mg^{2+} can induce G4 instability and dissociation (20). Presumably, the divalent ions interact with the G4 structures in two different ways: they can bind to the

phosphate groups, reducing the charge repulsion and, at higher concentrations, also coordinate in a bidentate manner the 6-keto and 7-imine groups of guanines involved in hydrogen bonding, thus disrupting the G4 structure (21). Therefore, even cations with similar ionic radii, *e.g*. Ca^{2+} (0.99 Å) and Na^{+} (0.97 Å), can have different effects on G4 stability (22). Indeed, not only the ionic radius but also other properties of the cations, including their dehydration energy and coordination number, are essential to determine their overall effect on folding and stability of G4 structures (22, 23). Structural polymorphism of G4s is probably the main reason of their regulatory function in physiological and pathological processes, which makes them interesting targets for diagnostic and therapeutic applications.

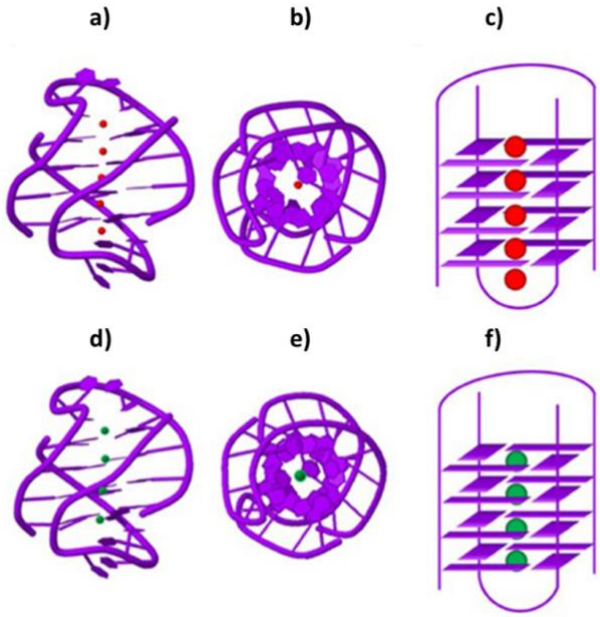

Figure 6. G-quadruplex structures of *Oxytricha nova* telomeric DNA d(GGGGTTTTGGGG) in the presence of K^{+} (a, b, c) or Na^{+} (d, e, f). K^{+} ions are located between two adjacent G-tetrads (PDB entry: 1JPQ), while Na^{+} ions are in the G-tetrads planes (PDB entry: 1JB7). a,d) side view, b,e) top view, c,f) schematic illustrations (adapted from (24)).

1.2 Biological role of G-quadruplexes

It has been widely demonstrated that putative G4 forming sequences (PQS) are present in several important regions of the human genome, including telomeres (25) and gene promoters (26). In particular, bioinformatic analyses suggested that about 376,000 sequences potentially able to fold into G4 structures are present in the human genome (27), mainly distributed in the previously mentioned regions. A successive study highlighted that the above-used algorithm represents a simplification that significantly underestimates the actual number of G4 forming sequences in the genome for several reasons (27). First of all, since G4s composed of two stacked tetrads are generally less stable than single-stranded or duplex DNA, only sequences able to form three or more G-tetrads are considered physiologically relevant; secondly, loops including from 1 to 7 nucleotides are known to form G4s with stability decreasing on length increasing; finally, sequences with discontinuities in the G-tracts are not very stable and thus are not included in PQS (27). Indeed, many experimental studies proved that the previously used algorithm generates both false positives and negatives. To overcome these limitations, Mergny and co-workers recently developed a different algorithm called G4Hunter (28). It considers the G-richness of a sequence, as well as the C-richness of its complementary strand able to form a stable duplex competing with the potential G4 structure, giving a G4 propensity score as the output. After validation of the model by analysis of a large dataset of sequences, it was applied to the human genome proving that the number of sequences able to fold into G4 structures is higher than previously estimated by a factor of 2-10 (28). Moreover, high-resolution sequencing-based methods to detect G4s in the human genome also confirmed the higher number of G4s that can be formed in the genome (> 700,000) than

previously predicted by computational methods (29). The *in vivo* formation of G4s was also investigated. Balasubramanian and co-workers produced BG4, a fluorescent antibody specifically recognizing telomeric G4 structures (30) which demonstrated the presence of G4s in cells and the interaction between the telomerase enzyme and the telomeric G4, further corroborating their involvement in biological processes (31) (Figure 7).

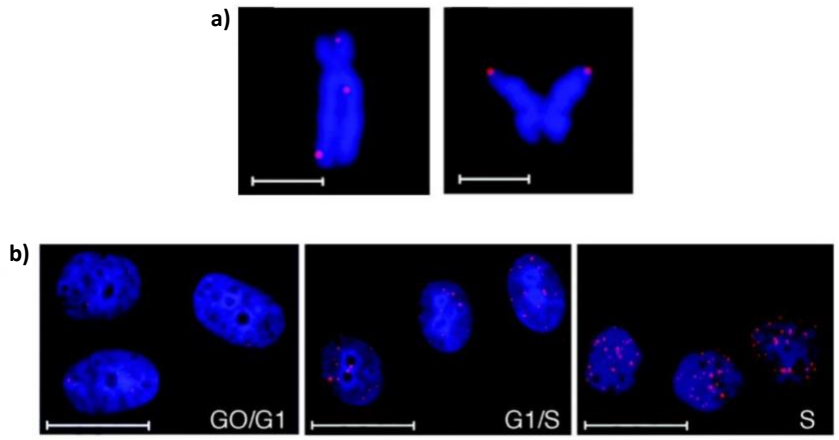

Figure 7. a) G-quadruplex visualization at telomeres in HeLa cells using BG4 antibody (red); b) increase of the BG4 foci during cell cycle, from G0/G1 to S phase in synchronized MCF-7 mammary adenocarcinoma cells. Chromosomes and nuclei are counterstained with DAPI (blue). Scale bars correspond to 2.5 μm in a) and 20 μm in b). (adapted from (30)).

These findings had a crucial impact in this research area, not only definitively proving the *in vivo* G4 existence, but also elucidating their biological functions. Within this thesis, we will focus on DNA G4 structures found in oncogene promoters and telomeres. A proto-oncogene is a normal gene coding for a protein involved in cellular growth-controlling pathways (32). If a mutation occurs in this gene, it can turn into an oncogene, *i.e.* a gene that encodes for a protein capable of transforming normal cells and inducing cancer (32). A large number of G4 forming sequences have been identified in promoter regions of

several oncogenes (33). The formation of G4 structures is indeed one of the regulation systems of their transcription, highlighting their role as promising targets in anticancer therapy (34). In this frame, the development of ligands able to stabilize oncogene promoter G-quadruplexes is of particular interest, being able to inhibit a specific mutated proto-oncogene (34) (Figure 8, left).

Telomeres are DNA sequences present at the ends of eukaryotic chromosomes characterized by repetitive nucleotide sequences with a double strand region and a 3' single-stranded overhang (35, 36), with a "capping function", protecting chromosomal termini from unwanted recombination and degradation, thus guaranteeing proper replication (37, 38). The primary method for maintaining telomere length is provided by telomerase, an RNA-dependent DNA polymerase that synthesizes telomeric DNA sequences (39). Most healthy human somatic cells lack telomerase activity; in contrast, this enzyme is overexpressed in over 90% of malignant cells and *in vitro* immortalized cells (39). This means that telomere shortening is found in mammalian somatic cells with increasing age *in vivo* and progressive cell division *in vitro*, acting as a molecular clock that might track the history of cell replication. Contrarily, cancer cells are "immortal" because the telomeres are kept at a constant length due to the action of telomerases. Based on this, it is evident that telomere maintenance is crucial for the growth of tumors (37). Therefore, disrupting telomere homeostasis is a very promising approach in the search for novel anticancer treatments. The 3' single-stranded overhang structure can be changed by ligands that can stabilize telomeric G4s, making it impossible for telomerase to recognize the end of the telomere and causing cancer cells senescence and finally apoptosis (40) (Figure 8, right).

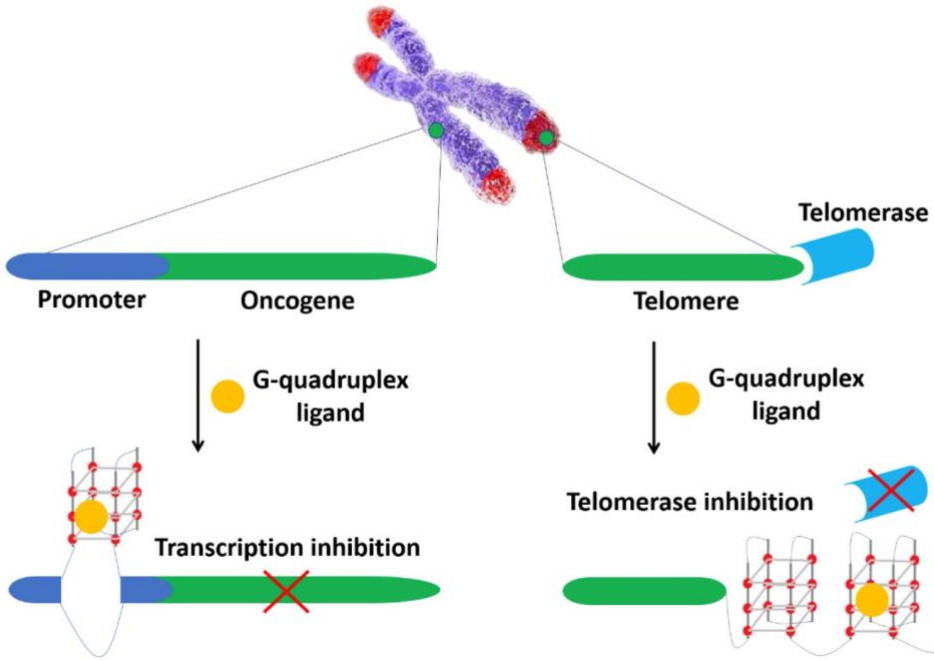

Figure 8. Ligands stabilizing G-quadruplex structures inhibit oncogene transcription and telomerase activity.

1.3 Small molecule-based probes for G-quadruplex detection

A large body of experimental data prove that G4s are crucial elements in physiological and pathological processes. However, despite the plethora of experiments reported in literature through the years, their specific biological functions in different metabolic pathways still need to be fully clarified. Moreover, only a small fraction of the PQS predicted in human genome using bioinformatic analysis has been identified and studied. For these reasons, the development of new tools for the *in vitro* identification of G4 forming sequences is fundamental. The development of fluorescent antibodies gave a significant contribution to this field due to their high specificity for a wide

range of different targets. Nevertheless, antibodies are expensive, have limited stability and are characterized by poor cellular permeability. Moreover, an antibody has to be conjugated with a fluorescent probe to allow the desired target visualization and, even exploiting this strategy, thus far no antibody selectively recognizing specific G4 topologies has been obtained yet.

In the last few years, a number of small molecule-based fluorescent probes for the identification of G4 structures have been developed (41). These probes offer the unique advantage of being based on chemical structures which can be easily modified through chemical synthesis to modulate their fluorescent properties, solubility and affinity for the target. An ideal fluorescent probe should be able to interact with the target in its native environment, without altering its conformation or structure. Several structural elements distinctive of G4s can be exploited for the interaction with targeting ligands, *i.e.* the guanine tetrads, the loops and the grooves, exploiting three potential different binding modes: 1) π-π stacking with planar guanine tetrads; 2) recognition of loops and grooves through electrostatic interactions and/or hydrogen-bonds; 3) intercalation between tetrads (42). Small molecules which are known G4 binders are typically characterized by common structural features. An extended planar aromatic surface guarantees strong π-π stacking interactions with guanine quartets, even stronger in the case of an electron-poor aromatic scaffold. Indeed, strong cation-π interactions with the negatively charged backbone of the G4 ensure high affinity. Moreover, a common feature of G4-selective probes is the presence of decorating groups carrying positively charged moieties able to generate electrostatic attractions with the phosphate backbone or hydrogen bonds with the grooves (42). With the aim of designing effective G4-selective fluorescent probes, all these aspects must be considered, however without altering the spectroscopic properties of the probe, which are

crucial for an efficient target visualization. Indeed, a promising probe should be able to selectively recognize a specific target exhibiting a very strong fluorescence signal in the physiological environment.

In recent literature, a wide number of fluorescent probes selective for G4 structures have been described. They can be classified on the basis of their chemical structure or of the fluorescent response they give upon target interaction.

1.3.1 Fluorescent light-up probes

These interesting compounds are very promising because they are non-emissive as free molecules in solution, but capable to give a strong fluorescent signal upon target recognition. Indeed, when they are free in solution, rotation and vibration around a single bond cause the thermal deactivation of the emitting excited state. On the other hand, upon target interaction, they are forced to adopt a more rigid conformation, leading to a marked fluorescence light-up. The most representative molecules of this class of probes are cyanine-based dyes, characterized by two heteroaryl moieties connected through a methine or polymethine spacer. Among them, the best known compounds are Thiazole Orange (TO) (43) and Thioflavin T (ThT) (44) (Figure 9). In the last years, a series of analogues of known fluorescence probes have been designed and synthesized to achieve higher selectivity and affinity, retaining or magnifying the fluorescent properties of the parent molecules. A typical modification is the extension of the conjugated system. Dir and 9E-PBIC (Figure 9) are two examples of this strategy. The first one, characterized by a modified dimethylindole scaffold attached to a quinolinium group carrying an anionic propylsulfonate tail, shows very low fluorescence quantum yield in

aqueous solution, but very high quantum yield in the presence of parallel c-MYC with good selectivity (45). 9E-PBIC is a carbazole-based probe able to recognize c-MYC with high selectivity, as demonstrated by the 118-fold enhancement in emission intensity at 600 nm as reported by Lin *et al.* (46). Analogues of triphenylamines have been also reported. Among them, one of the most interesting is NBTE (Figure 9), characterized by an emitting excited state with a lifetime remarkably affected by binding with G4s of different topologies which allows the visualization of G4s in living cells by fluorescence lifetime imaging (FLIM), as well as the discrimination of different G4 topologies from other nucleic acid sequences (47). Also quinazolones, quinoxalines and quinolines (48–50) have to be mentioned for their excellent properties as fluorescence light-up probes. Among these, QUMA-1 (Figure 9) is able to give a significant fluorescence light-up in the presence of different RNA G4s, such as TERRA, FMR1, TB1 and MT3, allowing monitoring the dynamics of RNA G4 folding and unfolding in living cells (51).

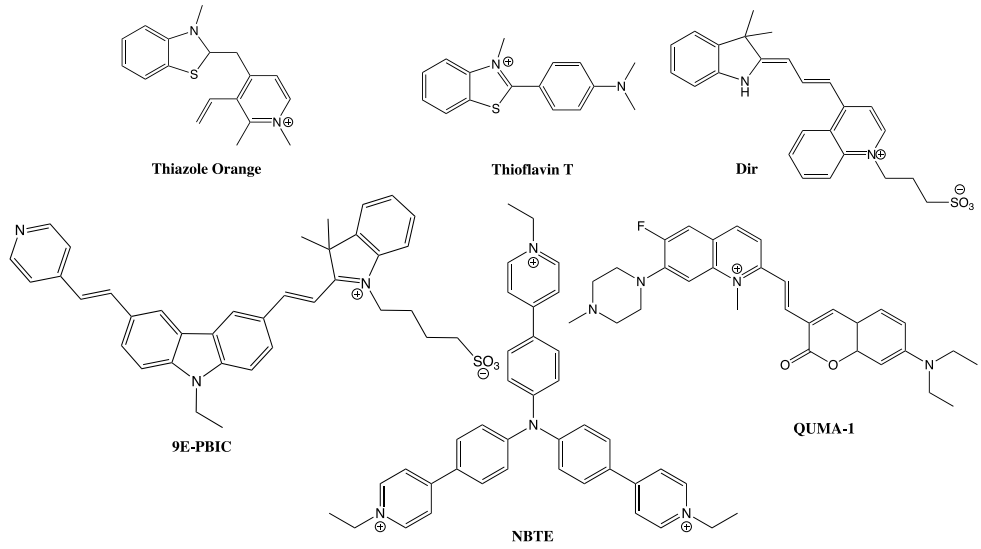

Figure 9. Examples of fluorescent light-up probes.

1.3.2 Aggregation-based probes

Some small molecules, due to their hydrophobic properties, form aggregates in aq. solution, generating quenching or enhancement of the fluorescent signal. In the first case, J-aggregates characterized by stacked monomers in "head-to-tail" conformation are formed; in the second case, the molecules are arranged in a "head-to-head" disposition, resulting in the formation of H-aggregates (52). The latter strategy has been more used for the detection of G4s. Indeed, the interaction of these probes with G4s disrupts the aggregates in solution, thus restoring the emission of the monomer. Examples of this kind of molecules are cyanine-based dyes, as Dir-Trimer (Figure 10). Indeed, this molecule is able to give a strong response upon binding with parallel quadruplexes, especially c-MYC. Thus, it can be used to differentiate parallel G-quadruplexes from other DNA forms, such as single or double-stranded DNAs (53).

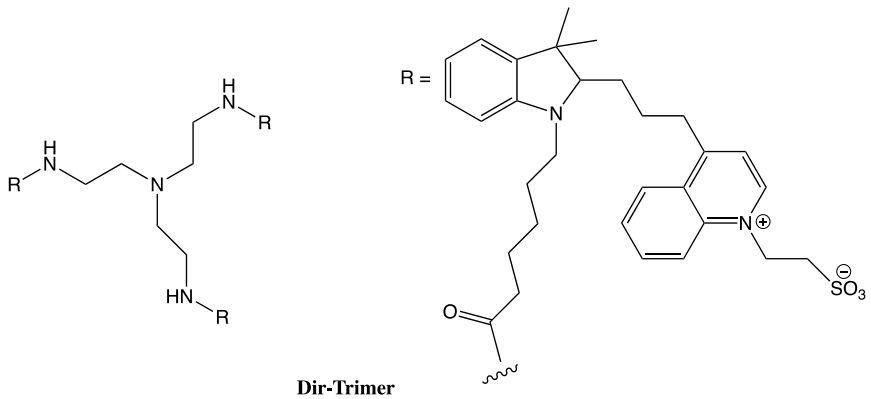

Figure 10. An example of aggregation-based fluorescent probes.

1.4 G-quadruplex Ligands as therapeutics

G4 ligands have been investigated also as therapeutic agents. Main feature required for a good therapeutic agent is its ability to selectively recognize a specific target. Since the structural features required to ensure a strong interaction between ligands and G4s are also those generally associated with their interaction with duplex DNA, through the years several G4-targeting small molecules have been studied to obtain structural information.

RHPS4 is a pentacyclic acridine able to interact with G4s through G-quartet end-stacking binding mode. It is able to interact with the parallel human telomere d[(TTAGGGT)]$_4$ G4 (Figure 11) (54), inhibiting telomerase-induced telomere uncapping and damage. A good *in vivo* anticancer activity was also demonstrated in xenograft mouse models (55). The 3,6,9-trisubstituted acridine BRACO-19 (Figure 11) is able to interact with two bimolecular human telomeric G4s of sequence d(TAGGGTTAGGGT) with good selectivity, showing antitelomerase activity and consistent *in vivo* anticancer activity in xenograft mouse models (56). The tetra-*N*-methyl-4-pyridyl porphyrin TMPyP4 **(**Figure 11) is able to bind the bimolecular human telomere G4 d(TAGGGTTAGGG) with good affinity, not only inhibiting telomerase activity, but also downregulating the expression of several oncogenes including c-MYC, KRAS, RET and c-KIT (57).

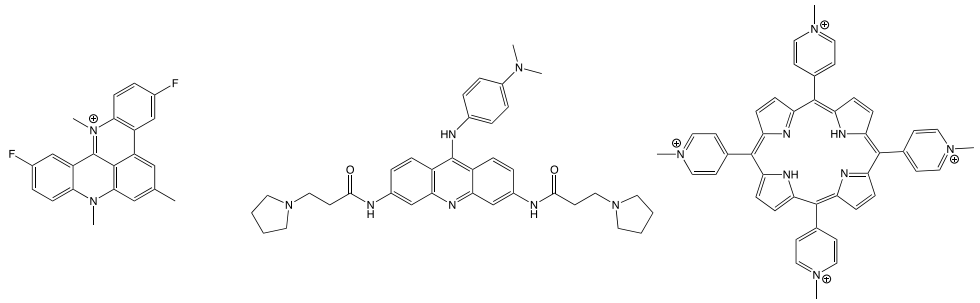

Figure 11. Examples of G-quadruplex-selective ligands endowed with therapeutic activity.

Other promising high-affinity G4 ligands are naphthalene diimides (NDIs) (58), having a proper core which can be easily functionalized with a variety of of substituents, usually two or more aminoalkyl residues, able to favour the selectivity towards G4 over duplex DNA (59). In the case of polyaminoalkyl-decorated NDIs, structural analysis showed π-π stacking of the NDI naphthalene core with the G-tetrad at the 3'-end of telomeric G4 d[AGGG(TTAGGG)$_3$], with the positively charged ammonium substituents protruding into the G4 grooves and interacting with the phosphates of the DNA backbone (60). Some NDIs have also shown a selective cytotoxic activity on various cancer cell lines, also associated with an *in vivo* anticancer activity in human pancreatic ductal adenocarcinoma (PDAC) animal models (61).

1.5 G-quadruplexes as therapeutics

Monoclonal antibodies have been the dominant agents for the identification and inhibition of target molecules in biomedical research since their first introduction in 1975 (62). However, the high immunogenicity, low manufacturing, high cost, and poor stability of monoclonal antibodies are

important issues limiting their widespread use. Oligonucleotide aptamers have recently emerged as the most promising alternative to antibodies. Aptamers made of nucleic acids are small (20–70 bases) single-stranded DNA- or RNA-based molecules that, when folded into their three-dimensional shape, can recognize a chosen target of biological interest with high affinity and specificity. The name "aptamer" comes from the Latin term "aptus," which means "to fit" implying that these molecules have a significant propensity for binding to specific targets by adapting their conformation to the one of the target itself (63). They are additionally known as "chemical antibodies". However, with respect to antibodies, aptamers exhibit remarkable advantages, as it is generally easy to introduce site-specific chemical modifications into oligonucleotide aptamers so to finely tune their binding affinity to the target or increase their stability against nuclease digestion (64–66). These intriguing properties make oligonucleotide aptamers the most advanced tools for detection and inhibition of target molecules beyond monoclonal antibodies for both therapeutic (67–69) and diagnostic applications (70–73).

Aptamers with high affinity and specificity for a given target are usually identified through an *in vitro* selection procedure called Systematic Evolution of Ligands by EXponential enrichment (SELEX), which was first developed in 1990 (63, 74, 75). SELEX is an iterative screening process that selects aptamers starting from a large oligonucleotide library of randomly generated sequences. The sequences are exposed to the target ligand, for example a protein or a small molecule immobilized on a solid support, and the ones that do not bind to the target are removed by simple washings or target capture on paramagnetic beads. This step is followed by multiple rounds of enrichment of the bound oligonucleotides. The iterative enrichment process includes elution of bound oligonucleotides and their subsequent amplification by polymerase

chain reaction (PCR). The oligonucleotides of the initial library are characterized by a variable region of fixed length, flanked by constant regions in the 5′- and 3′-ends which serve as primers for the amplification step (Figure 12).

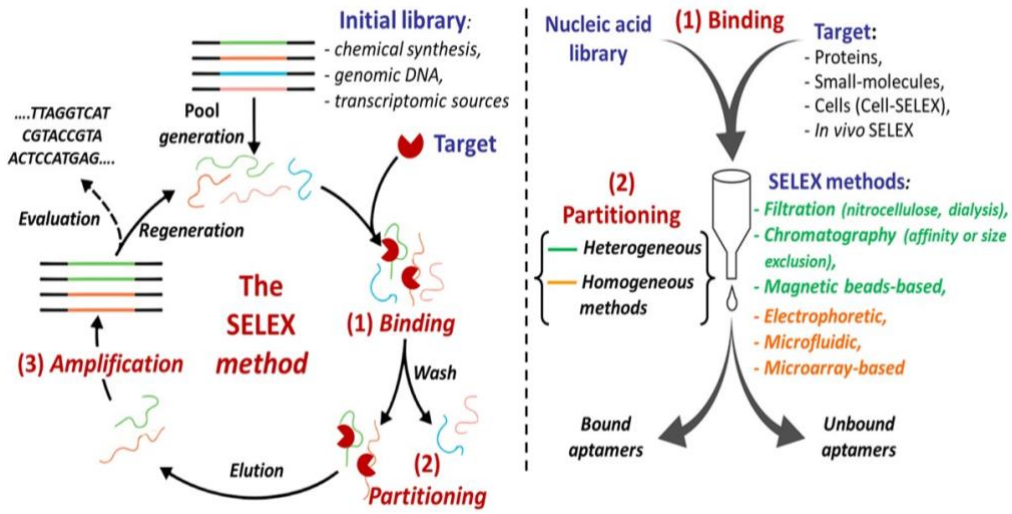

Figure 12. Schematic representation of the SELEX technology (adapted from (10)).

The outstanding progress achieved in this field has led to the identification of a large number of aptamers specific for very different kinds of targets *e.g.* small molecules, ions, proteins, cells, or even whole organisms, such as viruses or bacteria (76–78).

Notably, many of the oligonucleotides with good biological activity among the combinatorially chosen aptamers are G-rich sequences capable of adopting G4 conformations. This is not surprising if we consider the polymorphism of the G4s. High polymorphism means high adaptability, due to the ability of these sequences to fold into peculiar structures which deeply differ from each other and are thus able to fit and recognize a plethora of very different targets. Over

900 aptamers have been developed so far against various targets for medical treatments and diagnostics (79). Aptamers have been generated for medicinal purposes against a wide range of diseases, such as AIDS, cancer, diabetes, and skeletal disorders. For the treatment of macular degeneration, cancer, coagulation, and inflammation, many aptamers are undergoing various phases of clinical trials. Pegaptanib sodium is the first therapeutic aptamer licensed by food and drug administration (FDA) in 2004 for the treatment of wet age-related macular degeneration (wet AMD). It is an aptamer against vascular endothelial growth factor (VEGF) and has been effectively used in market (80–83), opening a wide range of opportunities for the development of further therapeutic oligonucleotide aptamers. However, in 2011 bevacizumab and aflibercept (84, 85) effectively replaced pegaptanib in AMD treatment (86, 87). In this thesis I will focus on anti-VEGF and anti-HMGB1 aptamers for diagnostics and theranostics.

1.6 The Vascular Endothelial Growth Factor (VEGF)

A variety of physiological processes, including embryogenesis, cellular growth and differentiation, wound healing and reproductive systems, depend on neovascular formation, also known as angiogenesis. Several powerful cytokines which are part of the VEGF family play different roles on the vascular endothelium, such as angiogenesis, lymphangiogenesis and vasculogenesis. Angiogenesis and lymphangiogenesis can be defined respectively as the formation of new blood vessels and lymphatic vessels from pre-existing ones; in turn, vasculogenesis is the development of blood vessels from precursor cells during early embryogenesis (88–90). Endothelial cells (ECs) survival and maintenance depend on VEGF. In fact, VEGF is detected

since the first days following embryo implantation and, starting from 16 to 22 weeks of gestation, is expressed in all organs (91–93). However, a VEGF overexpression can stimulate unregulated blood vessel growth causing pathological processes, like cancer and intraocular vascular disorders (94). The overexpression of VEGF in cancer cells is related to their peculiar hypoxia condition. Indeed, only in the presence of high oxygen concentrations the hypoxia-inducible factor (HIF), a transcription factor able to stimulate the release of VEGF, is hydroxylated by HIF prolyl-hydroxylases and in this form recognized by the von-Hippel Lindau tumor suppressor protein, thus becoming a target for polyubiquitylation and proteasomal degradation (95). On the other hand, in hypoxia conditions, HIF is not hydroxylated and degraded, so it acts as a transcription factor stimulating the overproduction of VEGF, which in turn promotes angiogenesis (95, 96).

1.6.1 The VEGF family

The VEGF family is characterized by six structurally related glyco-polypeptides *i.e.* VEGF-A, VEGF-B, VEGF-C, VEGF-D, VEGF-E and placenta growth factor (PlGF) (97, 98). The members of this family can recognize three different tyrosine kinase receptors (VEGFRs) which are VEGFR-1 (Flt-1), VEGFR-2 (KDR/Flk1), and VEGFR-3. VEGF-A can bind VEGFR-1 and VEGFR-2, playing a role in angiogenesis, proliferation, migration, and permeability of ECs (Figure 13) (99); VEGF-B specifically recognizes VEGFR-1 and is involved in extracellular matrix (ECM) degradation and ECs migration (100); VEGF-C and VEGF-D are able to bind both VEGFR-2 and VEGFR-3, being mainly involved in the regulation of lymphangiogenesis (101); VEGF-E interacts with VEGFR-2 exhibiting high

mitogenic activity (102); in turn, also PlGF is able to bind VEGFR-1 (103) (Figure 12). While VEGF regulates the physiological vascular homeostasis in several cell types and tissues, it has been shown to have a role in the molecular pathogenesis of a variety of diseases (104) which is related to its activity on vascular permeability and neo-angiogenesis. In addition to different pathologies like rheumatoid arthritis (105), psoriatic skin (106), ovarian hyperstimulation syndrome (107) and AMD (108), VEGF is also involved in cancer. Tumour cells secrete high levels of VEGF, stimulating the proliferation of ECs, with consequent formation of new abnormal blood vessels (109). VEGF is mainly overexpressed in lung (110), breast (111), gastrointestinal tract (112), liver (113), ovary (114), and glioblastoma multiforme (115). For this reason, VEGF is considered a valid tumour marker (116, 117). Among the cytokines which are part of the VEGF family, VEGF-A is the main one, being involved in regulating angiogenesis during homeostasis and diseases. The two main isoforms of VEGF-A are $VEGF_{121}$ and $VEGF_{165}$, which promote tumor angiogenesis (118). These isoforms are characterized by a common receptor binding domain (RBD). However, $VEGF_{165}$ has also a heparin binding domain (HBD), which enhances the interaction with its receptor, triggering a more relevant angiogenic response in malignant cells (119).

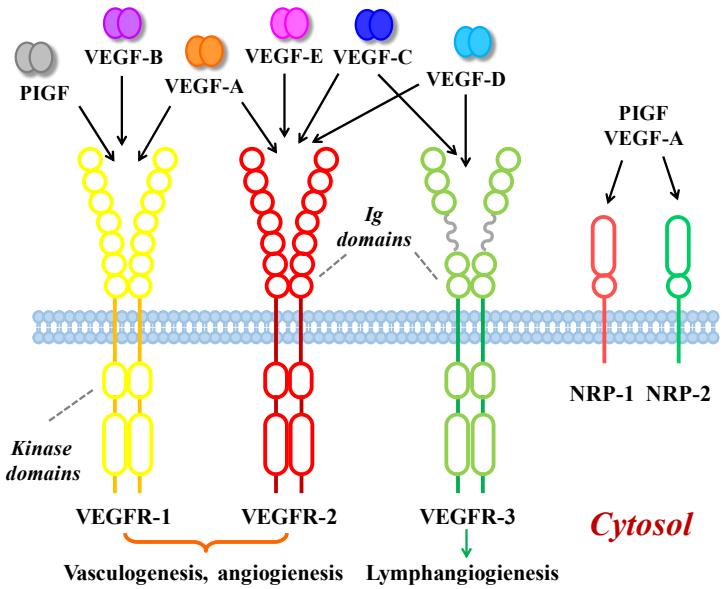

Figure 13. VEGF receptors and their ligands (adapted from (120)).

1.6.2 Anti-VEGF strategies in cancer treatment

In this frame, it is not surprising that the majority of antiangiogenic strategies, particularly in cancer, are based on VEGF suppression. Indeed, its discovery as an important regulator of angiogenesis has led to recognize it as a valuable therapeutic target for anticancer treatments (121). Different anti-VEGF strategies have been developed through the years, *i.e.* based on small molecules, antibodies or peptides/proteins (122) as well as DNA aptamers (120). In this thesis work, I will focus on the latter strategy.

1.6.3 Anti-VEGF G-quadruplex forming DNA aptamers

As mentioned before, many biologically active aptamers able to interact with target proteins obtained through SELEX are G4-forming oligonucleotides. Indeed, G4s have twice the negative charge per structural unit than duplexes, favouring the interaction with the positively charged pockets of many protein-binding domains (123). Moreover, G4s are characterized by high plasticity and adaptability, favouring the interaction with a specific target with tunable binding events.

Several G-rich oligonucleotides were fished out by SELEX using VEGF as target. Nonaka et al. selected the aptamer V7t1, which exhibited high affinity for both $VEGF_{165}$ (K_d = 1.4 nM) and $VEGF_{121}$ (K_d = 1.1 nM) (124). In detail, the authors firstly identified the aptamer Vap7 performing a SELEX toward the isoform $VEGF_{121}$, characterized by the RBD but not the HBD domain. Vap7 was able to bind both the $VEGF_{121}$ and $VEGF_{165}$ isoforms exhibiting K_d values of 1.0 and 20 nM, respectively. Then, the same authors designed and synthesized V7t1, a truncated version of Vap7 containing only the bases presumably involved in the G4 core formation. In contrast to Vap7, which, as shown by circular dichroism (CD) studies, adopted a parallel G4 structure, V7t1 had an unusual CD signature that can be attributed to a mixture of several G4 conformations (124). The same authors optimized this aptamer through in silico maturation obtaining four novel aptamers, the best of which was 3R02, showing an improved affinity for $VEGF_{165}$ with respect to V7t1 (K_d = 0.3 nM) (125). All these oligonucleotides were characterized by a common TGTG motif at their 5′-end, which probably played an important role in promoting the

overall structuring recognized by the protein. In analogy to V7t1, also 3R02 exhibited CD spectra profiles indicative of a mixture of conformations (125).
In previous studies of the research group where this thesis has been carried out, the main features of V7t1 aptamer were investigated, aiming at elucidating its bioactive conformation. This research demonstrated that, in the presence of physiological extracellular Na^+ concentrations, this aptamer has a very different conformational behaviour if subjected to annealing procedures or not. The annealed samples of V7t1 were prepared by heating the oligonucleotide at high temperature and then slowly cooling it to r.t. to favour the thermodynamically stable conformations. In fact, annealed V7t1 (here named A. V7t1) adopts a monomeric, largely antiparallel G4 folding, while not-annealed V7t1 (here named N.A. V7t1) mostly forms dimeric parallel G4 structures. Surprisingly, electrophoresis mobility shift assay (EMSA) experiments revealed that only the dimeric aptamer effectively binds $VEGF_{165}$, displaying a higher affinity for the protein compared to the monomeric form (Figure 14) (126). These findings were explained in terms of multivalency effects which may be operative in dimeric or multimeric aptamers, providing a more efficient binding for target recognition (127).

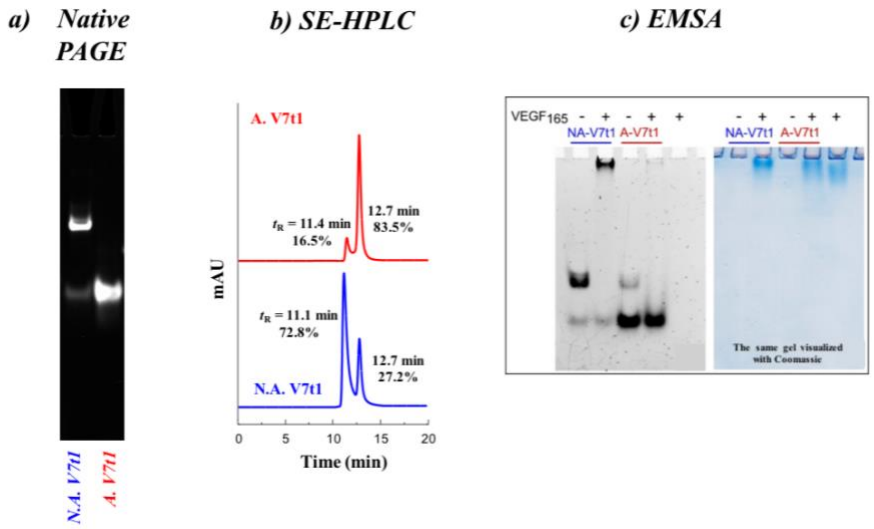

Figure 14. a) 10 % native PAGE and b) SE-HPLC analysis of N.A. and A. V7t1 in HEPES/Na^+ buffer. C) EMSA of N.A. and A. V7t1 incubated with $VEGF_{165}$. The same gel was first stained with GelGreen (left) and then with Coomassie (right) (adapted from (126)).

These results provided the basis for my successive research, reported in this thesis and thoroughly discussed in Chapter 3.

1.7 HMGB1 protein: physiological and pathological roles

High-Mobility Group Box (HMGB) is a family of three mammalian nuclear proteins which includes HMGB1, HMGB2 and HMGB3 (128). HMGB1 protein was first isolated almost 50 years ago as an abundant non-histonic and chromatin-associated protein with high electrophoretic mobility (129). HMGB1 is present within the nuclei of almost all eukaryotic cells and is involved in the maintenance of nucleosome structure and regulation of gene transcription, promoting access of transcriptional factors to specific genes

(130, 131), although HMGB1 itself is not sequence-specific. Human HMGB1 is a small protein consisting of 215 amino acids and has three distinct domains: two tandem domains, composed of approximately 80 amino acids, known as HMG boxes A and B, which share more than 80% identity and are connected through a short flexible linker of 24 amino acids to the 30 amino acid-long acidic C-terminal tail (Figure 15a). HMG boxes are well conserved DNA-binding domains and are characterized by three α-helices arranged in L-shaped conformation (132, 133) (Figure 15b,c).

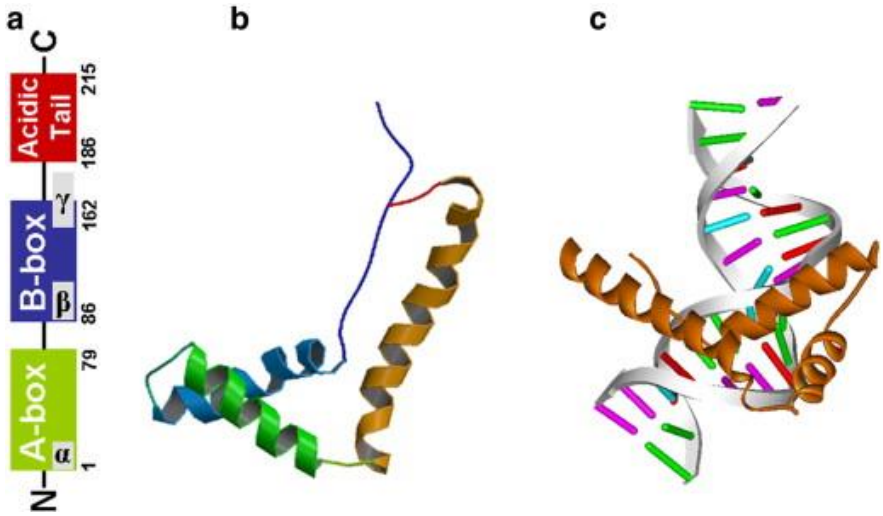

Figure 15. a) The domain structure of HMGB1: α is the heparin-binding site (6-12), β the cytokine inducing peptide (89-108), γ is the RAGE binding motif (150-183); b) Structure of the "HMG box" (Protein Data Bank, PDB: 1HME); c) HMG domain bound to a DNA duplex. (adapted from (134))

The A and B boxes of the protein can interact with DNA, thus producing either bending or distortion of the double helix (132, 133, 135). The acidic C-terminus contributes to the spatial arrangement of both A and B boxes and regulates HMGB1-DNA binding specificity (136). The N- and C-terminal

regions of the protein are rich of basic and acidic amino acid residues, respectively (137–139). Despite its ability to induce kinks in linear double-stranded DNA (140), HMGB1 can recognize and bind with high affinity various types of non-canonical (*i.e.* non-B) DNA structures, such as cruciform, hemicatenated and UV- or cisplatin-damaged DNA (141–143). Thanks to its "architectural" features, this protein is able to facilitate the assembly of certain nucleoprotein complexes and is considered a key factor in fundamental nuclear events, including DNA recombination, replication (144), remodeling (145, 146) and repair (147). HMGB1 was also identified as an important extracellular mediator in inflammation processes. This protein is passively released from necrotic cells by simple diffusion into the extracellular environment (148), thus triggering innate immune response via its interaction with cell surface receptors. In terms of effects or functions within lymphoid cells, HMGB1 is mainly secreted from mature dendritic cells (DCs) to promote T-cell and B-cell reactivity and expansion, and from activated natural killer cells to promote DCs maturation during the afferent immune response (149). Increasing advances in understanding the role of HMGB1 in immunity have led to widely accept the notion that HMGB1 acts as an important, potent and ubiquitous cytokine that exerts significant effects on both myeloid and lymphoid cells. Indeed, it plays a complex modulatory role in both innate and adaptive immune responses (149, 150). Extracellular HMGB1 stimulates the motility of many cell types, including endothelial cells, fibroblasts, dendritic cells, macrophages, smooth muscle cells and tumour cells. The cell surface receptor RAGE plays a key role in most HMGB1-dependent migration mechanisms. The binding of HMGB1 to RAGE activates a signaling pathway through extracellular signal-regulated kinase (ERK), nuclear factor kappa B (NF-κB) as well as proto-oncogene tyrosine-protein kinase (Src) activations

(151) that ends up in cytoskeletal remodeling for regulation of cell migration (Figure 16). HMGB1 is also strictly linked to disease severity, development of cytokine storm (CS), acute lung injury (ALI) and acute respiratory distress syndrome (ARDS) in SARS-CoV-2 infection. Indeed, this infection produces the release of extracellular HMGB1 through down-regulation of angiotensin-converting enzyme 2 (ACE2) (152) and activation of node-like receptor pyrin 3 (NLRP3) inflammasome (153), autophagy and toll-like receptors 2 and 4 (TLR2/TLR4). HMGB1 activates TLR2, TLR4, RAGE receptors and mitogen-activated protein kinase (MAPK), causing activation of NF-κB signaling pathway (154), which induces neutrophil extracellular traps (NETs) formation, thrombosis and CS, together with ALI and ARDS (155–157). Considering the multiple roles of HMGB1 in a wide variety of pathologies, the identification of HMGB1 inhibitors is of significant experimental and clinical interest. It has been demonstrated that the inhibition of HMGB1-RAGE interaction represents a promising approach to modulate the inflammatory activity of the protein, as well as to block tumour growth and metastasis (134).

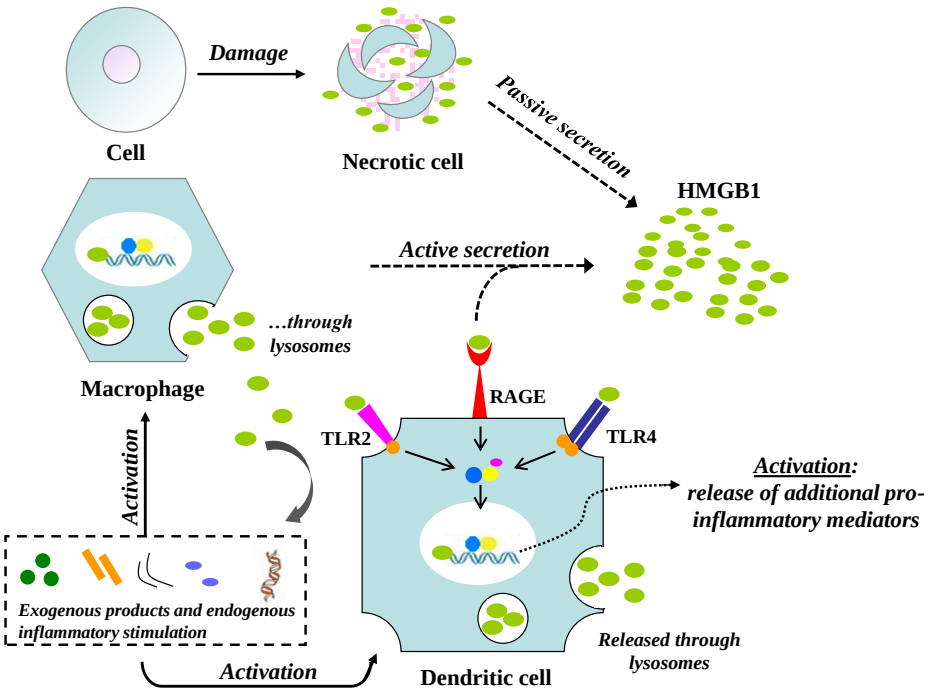

Figure 16. HMGB1 is a multi-functional regulator: in cell nucleus, it acts as an architectural chromatin-binding factor. It can be passively released by damaged or virus-infected cells, or actively secreted by innate immune cells in response to exogenous bacterial products [*e.g.* endotoxin or CpG-DNA] or endogenous inflammatory stimuli [*e.g.* TNF (Tumour Necrosis Factor) or IFN-γ (Interferon gamma)]. Extracellular HMGB1 acts on its target receptors leading to nuclear translocation of transcription factors [*e.g.* NF-kB (Nuclear Factor kappa-light-chain-enhancer of activated B cells)] and subsequent activation of the release of additional proinflammatory mediators. (adapted from (134)).

1.7.1 The HMGB1-receptor RAGE

RAGE is a multiligand transmembrane receptor composed of a short intracellular tail (43 residues) critical for signal transduction, a single transmembrane helix and three extracellular immunoglobulin-like domains, one variable-like (V) and two constant-like (C1 and C2) parts (158–160) (Figure 17), which is constitutively expressed in lung and skin.

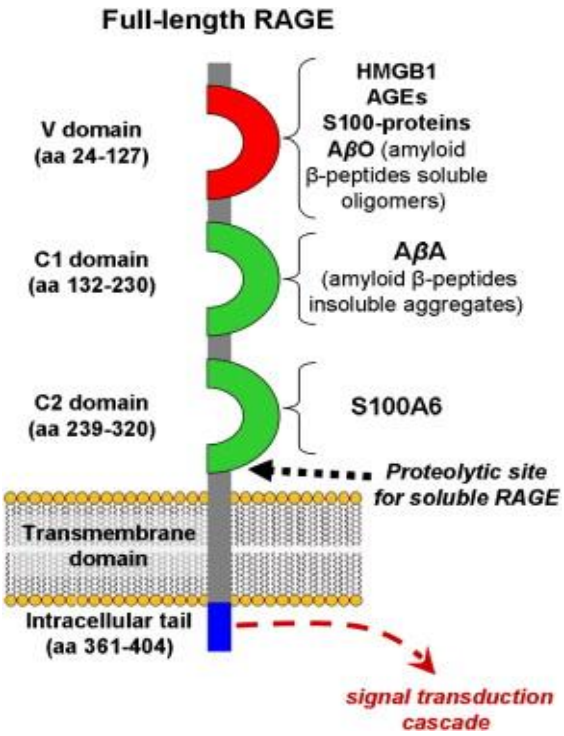

Figure 17. Schematic representation of RAGE protein and its domains. The association of ligands [*e.g.* AGEs (Advanced Glycation End Products), S100 proteins family, amyloid β-peptides] with RAGE results in a complex signal transduction cascade leading to cell activation (adapted from (134)).

In the majority of other cells, including vascular endothelial cells, neutrophils, DCs and neurons, RAGE expression is relatively low under physiological conditions (161), but increases when ligands, such as AGEs, or inflammatory mediators accumulate (162, 163). Since the RAGE promoter contains multifunctional NF-κB and SP-1 (Specificity Protein 1) transcription factor-binding sites (164), ligands and proinflammatory cytokines promote the expression of RAGE, potentially triggering a receptor-dependent autoinflammatory loop. RAGE exists in two main isoforms, the full-length RAGE, as transmembrane protein, and the soluble RAGE, that can be generated by proteolysis, lacking the transmembrane domain and the intracellular tail (165). RAGE was originally identified as a receptor for AGEs, but can also bind other structurally diverse ligands (166), including not only HMGB1, but also S100 calcium binding proteins and amyloid-β peptides (134, 167). Due to its multi-domain structure and ability to recognize different classes of ligands, RAGE behaves as a pattern recognition receptor (PRR) in orchestrating immune responses, analogously to innate immune receptors such as TLRs. However, unlike other PRRs, that predominantly bind to exogenous ligands, RAGE binds to endogenous ligands, especially those considered to be damage-associated molecular pattern molecules (DAMPs), such as HMGB1. RAGE activation through HMGB1 is involved in mediating several pathological conditions, including sepsis (168–171), cancer (172, 173), diabetes and Alzheimer's disease (174). Therefore, inhibition of HMGB1-RAGE interaction represents a promising approach in anti-inflammatory and anticancer strategies. It was indeed demonstrated that inhibition of the HMGB1-RAGE recognition suppressed tumour growth and metastasis in lung cancer (175).

1.8 Inhibitors of HMGB1-cytokine activity

1.8.1 Endogenous antagonists and exogenous small molecules as HMGB1 inhibitors

Several endogenous molecules neutralize extracellular HMGB1 or convert extracellular HMGB1-mediated functions from proinflammatory to anti-inflammatory. The hemoglobin-capturing protein haptoglobin (Hp) may also bind and sequester HMGB1 (176). The uptake of the Hp-HMGB1 complexes via cluster of differentiation 163 (CD163) elicits the release of anti-inflammatory cytokines and enzymes. Hp binds hemoglobin with a K_d value in the femtomolar range and HMGB1 in the nanomolar range, meaning that in free extracellular hemoglobin Hp displaces HMGB1, systemically increasing its levels. Thrombomodulin (TM) is an endothelial anticoagulant cofactor that promotes thrombin-mediated formation of activated protein C (autoprothrombin II-A) and exerts anti-inflammatory effects by binding and neutralizing extracellular HMGB1 (177). Moreover, TM aids the proteolytic cleavage of HMGB1 by thrombin (178). RAGE has several isoforms arising from alternative splicing: the full length, N-terminally truncated, and C-terminally truncated form. The C-terminally truncated form of RAGE is secreted from the cell, as well as an alternatively spliced form that lacks the transmembrane domain (sRAGE). sRAGE acts as a decoy receptor and has been successfully used to block HMGB1-RAGE signaling in several disease models (179). The complement component 1q protein (C1q) is known to possess immunosuppressive properties distinct from its role in initiating the complement cascade (180). It was recently reported that C1q can form a

multimolecular signaling complex with HMGB1, RAGE, and leukocyte-associated immunoglobulin-like receptor 1 (LAIR-1) in lipid rafts (181). The functional outcome of this interaction is that C1q and HMGB1 together promote monocytes to differentiate from an anti-inflammatory phenotype (M2 macrophages). In the absence of C1q binding, HMGB1 can promote the differentiation of proinflammatory macrophages (M1). Autoantibodies may also counteract proinflammatory HMGB1 activities. These autoantibodies can be generated during sepsis and be associated with a favorable outcome in patients undergoing septic shock (182).

In the last decades, several relatively small molecules were explored for their ability to inhibit HMGB1 pathological activity. These molecules derived: 1) from natural sources (*e.g.* glycyrrhizin, tanshinone IIA, (−)-epigallocatechin-3-gallate, quercetin, lycopene), mainly isolated from Chinese medical herbs, *e.g.* Danshen (*Salvia miltiorrhiza*) and Gancao (licorice); or 2) from chemical synthesis (nafamostat, sivelestat, atorvastatin, simvastatin, gabexate mesilate, methotrexate). Mollica et al. showed that glycyrrhizin, a natural triterpene found in roots and rhizomes of licorice (*Glycyrrhiza glabra*) with anti-inflammatory and antiviral properties, bound directly to both HMG boxes of HMGB1 ($K_d \approx 150$ μM) and inhibited its chemoattractant and mitogenic activities ($IC_{50} = 50$ μM for the inhibition of HMGB1-induced chemotaxis in fibroblasts and 15 μM for endothelial cells) (183). Salicylic acid (SA), the endogenously deacetylated product of aspirin (acetylsalicylic acid) and both synthetic (3-aminoethyl (AE)-SA) and natural (amorfrutin-B1) analogues of SA, were also discovered as good binders of HMGB1. Although K_d values for SA were estimated in the low μM range, the SA analogues 3-AESA and amorfrutin B1 had K_d values in the nM range. SA and analogues could inhibit the chemoattractant activity of HMGB1 as well as its cytokine-inducing effect.

This biological inhibition was deemed relevant based on estimated plasma SA concentrations after standard dose aspirin administration, while its analogues (3-AESA, amorfrutin B1) were observed to be orders of magnitude more potent (184).

1.8.2 Oligonucleotide (ON)-based inhibitors of HMGB1

Taking into account the role of HMGB1 in cell nuclei, where it interacts with DNA leading to distortion and bending of the double helix, and considering that HMGB1 is able to recognize with high affinity a wide range of distorted DNA structures (142), suitable DNA-based ligands were proposed as efficient modulators of HMGB1 activity. As a first approach, several HMGB1 ligands based on kinked DNA duplexes were designed and synthesized to increase the affinity toward the target protein (185, 186). Bending in the oligonucleotide structure was induced by asymmetric internal bulges obtained by insertion of unpaired adenines in the middle of one of the two strands. Interestingly, the examined bimolecular duplexes were recognized by HMGB1 with high affinity and were able to inhibit HMGB1-induced cell proliferation and migration in a concentration-dependent manner (186). Nevertheless, the thermal stability of these DNA-based HMGB1 inhibitors was in all cases quite low (T_m ca. 37 °C), not encouraging their further investigation on *in vivo* models (186). Aiming at improving the thermal and enzymatic stability of the kinked duplexes for potential *in vivo* applications as inhibitors of HMGB1 cytokine activity, a bent hairpin-loop DNA, designed as a unimolecular version of the bimolecular duplex, was also studied (187). Generally, in the search for DNA-based drugs with improved thermal and enzymatic stability, the

unimolecular forms are considered an attractive alternative to backbone-modified analogues (188–191). In addition to the unpaired adenines that generate the kink, this molecule contained an additional three-adenines loop connecting the two complementary strands (Figure 18a). This hairpin-loop duplex showed largely increased thermal and enzymatic stability compared to the previously studied bimolecular duplex, still efficiently interacting with HMGB1 protein. Furthermore, the kinked hairpin-loop DNA was able to inhibit the protein-induced cellular migration in a concentration-dependent manner, three orders of magnitude lower than the known HMGB1 inhibitor glycyrrhizin (134). More recently, Pagano et al. discovered that HMGB1 interacts with the 26-mer tract of the human telomeric DNA sequence d(TTAGGGTTAGGGTTAGGGTTAGGGTT) (tel_{26}) that is typically folded in a G4 structure (192) (Figure 18b). The same authors demonstrated that the protein can also bind to a G4-forming sequence in the promoter region of KRAS oncogene, with a stabilizing effect (193).

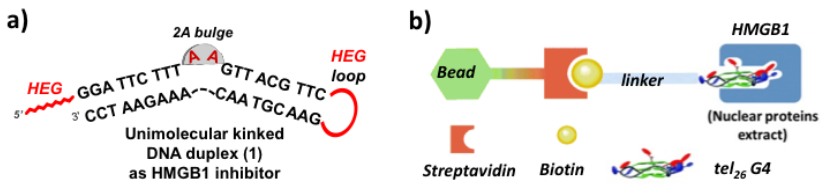

Figure 18. a) Schematic structure of the best HMGB1-inhibitor of a series of hairpin-loop bent duplexes. b) General scheme for HMGB1 "fishing" from nuclear protein extract, by telomeric tel_{26} sequence structured in G-quadruplex. (adapted from (187)).

Altogether, these results provided the basis for my successive research, reported in this thesis and thoroughly discussed in Chapter 4.

Chapter 2 - Aim of the PhD thesis

An estimated 10 million deaths, *i.e.* ca. one in every six deaths, were attributed to cancer in 2020, making it the second highest cause of death worldwide. Lung, prostate, colorectal, stomach and liver cancer are the most common types of cancer in men, while breast, colorectal, lung, cervical and thyroid cancer are the most common ones among women (194). Cancer continues to grow globally, exerting physical, emotional and financial strain on individuals, communities and health systems. Nowadays, 50% of tumours are only discovered when they are already in an advanced stage. Early cancer detection leads to more successful therapies and significantly higher survival rates. Recent improvements in early detection have undoubtedly saved lives, but more effective, non-toxic treatments and development of early cancer detection techniques are required (195).

In this context, the aim of the thesis is to develop useful biosensors and/or therapeutic agents based on G4 forming oligonucleotide aptamers, able to recognize proteic targets that are considered known biomarkers for early detection of tumours and/or inflammations, and novel *ad hoc* designed probes which give a marked fluorescence enhancement upon G4 binding.

In the first part of the thesis, we focused on aptameric systems for VEGF early detection. In detail, we evaluated the interaction between V7t1 and 3R02 aptamers and an *ad hoc* synthesized cyanine dye (here named CyOH) and the ability of these aptamer-dye complexes to recognize the target protein, with the aim of developing efficient anticancer theranostic systems, using different biophysical techniques, *i.e.* gel electrophoresis, circular dichroism (CD), UV-vis and fluorescence spectroscopy. The studied aptamer-dye complexes were tested on MCF-7 breast cancer cells to evaluate their diagnostic and therapeutic potential. Moreover, modified V7t1 analogues containing metal-binding

ligandosides were also synthesized and characterized with the aim to favour aptamer dimerization and VEGF recognition.

In the second part of the thesis, we focused on aptameric systems for HMGB1 early detection and inhibition. This protein is actively secreted from stressed and immune cells and passively released from necrotic cells in the extracellular environment, where it is involved in the pathogenesis of various inflammatory and immune diseases, as well as cancer (134). Moreover, it has been recently proposed as a biomarker and therapeutic target in SARS-CoV-2 infections (152). The project focused on G4 forming aptamers selective for HMGB1 identified through SELEX technology from a properly designed library of oligonucleotides. We explored the conformational behaviour and molecularity of the selected aptamers in a physiological buffer mimicking the extracellular environment (PBS, Phosphate-Buffer Saline) using UV-vis, CD, gel electrophoresis and size exclusion chromatography analysis in a combined approach and determined their thermal and enzymatic stability. Moreover, the affinity of these aptamers for HMGB1 was comparatively estimated by a properly designed and optimized ELISA (Enzyme-linked immunosorbent assay)-like assay. All the aptamers and the proper controls were also tested in cellular assays to evaluate their ability to inhibit cellular migration induced by the protein in order to select the most effective HMGB1 inhibitors.

Chapter 3 - Anti-VEGF systems for diagnostics and theranostics

3.1 State of art and synopsis

Nucleic acid aptamers are short single-stranded DNA or RNA, generally identified from combinatorial libraries of oligonucleotides by SELEX, which are able to recognize with high affinity and specificity a plethora of different targets, including proteins, small molecules and even whole cells.

Many biologically relevant aptamers are G-rich sequences that fold into stable G4 structures, as already discussed in Chapter 1.5. Due to their many advantages, including their wide target recognition, high affinity, stability, selectivity, and capacity to form peculiar H-bonds, aptamers are considered essential tools in the development of biosensors (also known as "aptasensors") in combination with different sensing techniques. We here focused on two G4 forming anti-VEGF aptamers, already known in literature, to develop new effective systems for cancer diagnostics and theranostics.

VEGF-A is a glycoprotein that includes many isoforms playing essential roles in angiogenesis, lymphangiogenesis and vasculogenesis, thus favouring the growth of solid tumours and being involved in the onset and progression of most tumours and/or inflammations (196). This growth factor is recognized as a valid tumour biomarker and therapeutic target. Therefore, selectively targeting VEGF-A, and particularly its main isoforms $VEGF_{165}$ and $VEGF_{121}$ (197), can be an extremely important strategy for early detection and therapy of cancer in the context of precision medicine. Several G4 forming aptamers have been identified for the selective inhibition of VEGF-A (120). In detail, Nonaka et al. selected the aptamer V7t1, which exhibited high affinity for both $VEGF_{165}$ (K_d = 1.4 nM) and $VEGF_{121}$ (K_d = 1.1 nM) (124). An in silico maturation, as post-SELEX optimization of this aptamer, allowed obtaining four novel aptamers, the best of which was 3R02, showing improved affinity

for $VEGF_{165}$ compared to V7t1 (K_d = 0.3 nM) (125). Previously, my research group demonstrated that V7t1 in a Na^+-rich buffer mimicking the extracellular environment is very different from a conformational point of view if subjected or not to annealing procedures, *i.e.* to heating to high temperature followed by very slow cooling to r.t., so to favour the thermodynamically stable conformations. Indeed, not-annealed V7t1 (N.A. V7t1) mainly forms dimeric parallel G4 structures, while the annealed oligonucleotide (A. V7t1) adopts a monomeric antiparallel G4 folding. Interestingly, only the dimeric aptamer efficiently binds $VEGF_{165}$, showing a higher affinity for the protein compared to the monomeric species (126), which was explained as the consequence of a multivalency effect (127, 198). Based on these preliminary studies, we here focused on the high-affinity VEGF binders V7t1 and 3R02. Our aim was to exploit these aptamers as promising candidates for the development of efficient tools for VEGF targeting if associated with *ad hoc* designed conformation-sensitive probes. In particular, we were interested in probes able to selectively bind and stabilize these aptamers in their bioactive conformations, generating complexes strongly recognized by the target protein and easily visualizable. In this frame, literature studies offer several fluorescent ligands which have been designed and investigated for the detection of G4 structures (199–201). Among these, cyanine dyes play a prominent role (202–204), being versatile molecules, easy to synthesize and *ad hoc* functionalize, allowing a fine-tuning of their G4 binding affinity and optical properties (203, 204). Thiazole orange (TO, 4-[3-methyl-2,3-dihydro(benzo-1,3-thiazole)-2-methylidene] quinolinium iodide), one of the most representative dyes of this class, is characterized by a very low intrinsic fluorescence in aq. solutions, marked chemical stability, and high molar absorption coefficient. It can interact with

different DNA and RNA structures, showing a remarkable fluorescence turn-on response (205). When TO interacts with G4 structures, a fluorescence enhancement >2-fold higher than that obtained with duplexes is observed (206). This behaviour is strictly connected with the intramolecular rotation around the C-C bond connecting the benzothiazole and quinoline heterocycles which compose the TO structure: when these moieties are free to rotate around this simple bond, for example when the ligand is dissolved alone in aq. solutions, its fluorescence is almost null. Upon interaction with duplex DNA, the molecular target acts as a rigid cage forcing TO into a fully planar conformation, which can thus form stable intercalation complexes between adjacent Watson-Crick base pairs. With G4 structures, TO can strongly bind the terminal G-quartets which offer a larger aromatic surface compared to the base pairs of duplex structures, thus allowing more intense π-π stacking interactions and higher fluorescence response of the ligand (207). Considering the intriguing properties of TO, we focused our attention on TO analogues as potential binders of the anti-VEGF G4 forming aptamers V7t1 and 3R02. In particular, we here selected a TO derivative, named CyOH (Scheme 1) (208, 209), designed to provide better solubility in aq. solutions and lower tendency to self-aggregate compared to the parent ligand, still maintaining the G4 recognition ability typical of TO. We thus analyzed the interaction of CyOH with the G4 forming aptamers V7t1 and 3R02 by different biophysical techniques, determining the stability and properties of the resulting complexes. We particularly investigated the fluorescence response of CyOH when bound to either V7t1 or 3R02 in relation to the aptamer conformation, molecularity and specific recognition by the protein. Finally, we evaluated the antiproliferative activity of the aptamer-CyOH complexes on MCF-7 breast cancer cells, using MCF-10A normal cells as a control, by MTT assays, as well

as their cell uptake and colocalization with a fluorescently-labelled VEGF-specific antibody by confocal laser scanning microscopy (CLSM) analysis. The data described below are extracted from a published article (Napolitano,E. et al. (2023) Selective light-up of dimeric G-quadruplex forming aptamers for efficient $VEGF_{165}$ detection. *Int. J. Biol. Macromol*.).

3.2 Results and discussion

3.2.1 Analysis of the interaction between V7t1 and VEGF protein

In a paper previously published by the research group where this thesis has been carried out, it was demonstrated that the dimeric, parallel G4 conformation present when the aptamer V7t1 is N.A. in HEPES/Na^+ buffer, can interact with the target $VEGF_{165}$ protein with higher affinity than the monomeric, antiparallel G4 adopted by the A. aptamer (126). With the aim of confirming this finding and supporting it with a quantitative determination of the affinity of $VEGF_{165}$ for N.A. vs. A. V7t1 in HEPES/ Na^+ buffer, chemiluminescence-based protein binding assays were here performed. In detail, $VEGF_{165}$ labeled with a Histidine-tag was immobilized into the wells of a copper-coated 96-well plate. Then, N.A. and A. 3′- biotinylated V7t1 samples in HEPES/Na^+ were incubated, in parallel experiments, with the anchored protein at different concentrations (steps 1 and 2, Figure 19a). After that, to each well streptavidin-HRP was added, which bound to the aptamer exploiting the biotin-streptavidin high-affinity interactions (step 3, Fig. 19a). In the last step, a specific ECL reagent, substrate of HRP, was added to each well producing a chemiluminescence signal proportional to the amount of V7t1 bound to $VEGF_{165}$ (steps 4 and 5, Figure 19a). In line with our expectations,

when V7t1 was N.A., a strong binding between the aptamer and the target protein was observed, with a K_d of ca. 33 nM calculated from fitting the fraction of bound $VEGF_{165}$ as a function of the aptamer concentration (Figure 20). By comparing the chemiluminescence signals of N.A. and A. V7t1, it clearly emerged that for the A. aptamer only a very weak chemiluminescence response was observed, with data that did not allow extrapolating a K_d value (Figure 19b). These results quantitatively demonstrated that the interaction between $VEGF_{165}$ and the dimeric V7t1 is far stronger than the interaction of the same protein with the monomeric aptamer, fully corroborating our previous qualitative findings based on EMSA experiments (126). In addition, to demonstrate that the biotin linker of the V7t1 aptamer did not alter the aptamer bioactive folding, an EMSA experiment under the same conditions previously reported (126) was performed using 3′-biotinylated V7t1, CyOH and $VEGF_{165}$. The obtained results were comparable to those reported for unmodified V7t1, demonstrating that the introduced biotin-linker modification did not affect the ability of the aptamer to recognize the protein (Figure 21).

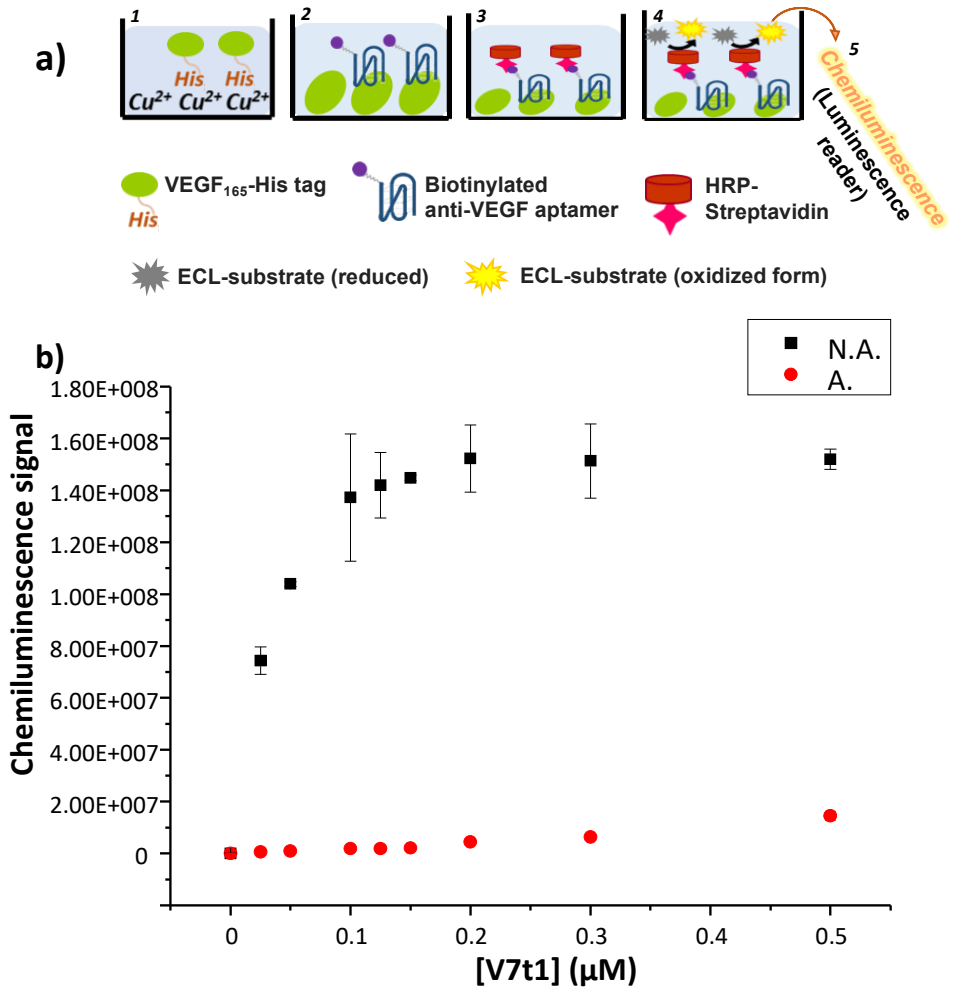

Figure 19. a) Schematic representation of the $VEGF_{165}$ binding assay on a copper-coated 96-well plate. b) Chemiluminescence signal reported as a function of the V7t1 aptamer concentration. Plotting is obtained by registering the chemiluminescence signals from fixed amounts of ECL/streptavidin-HRP added to increasing amounts of either N.A. or A. biotinylated V7t1 in HEPES/Na^+ pre-bound to 20 pmol of $VEGF_{165}$, previously immobilized on a 96-well plate. The black squares refer to N.A. V7t1 (predominantly dimeric G-quadruplex structure), the red dots refer to A. V7t1 (only monomeric G-quadruplex structure) (210).

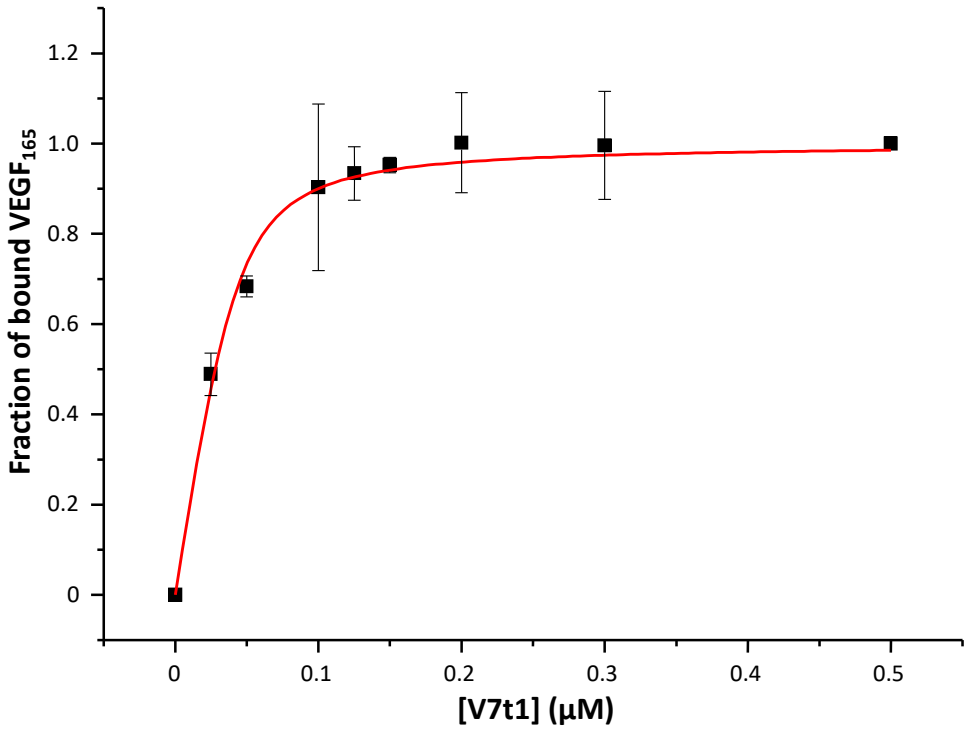

Figure 20. Binding curve obtained by plotting the fraction of bound $VEGF_{165}$ as a function of N.A. V7t1 aptamer concentration. The black squares represent the experimental data, the red line is the best fit obtained with an independent and equivalent-sites model (see experimental section for details) (210).

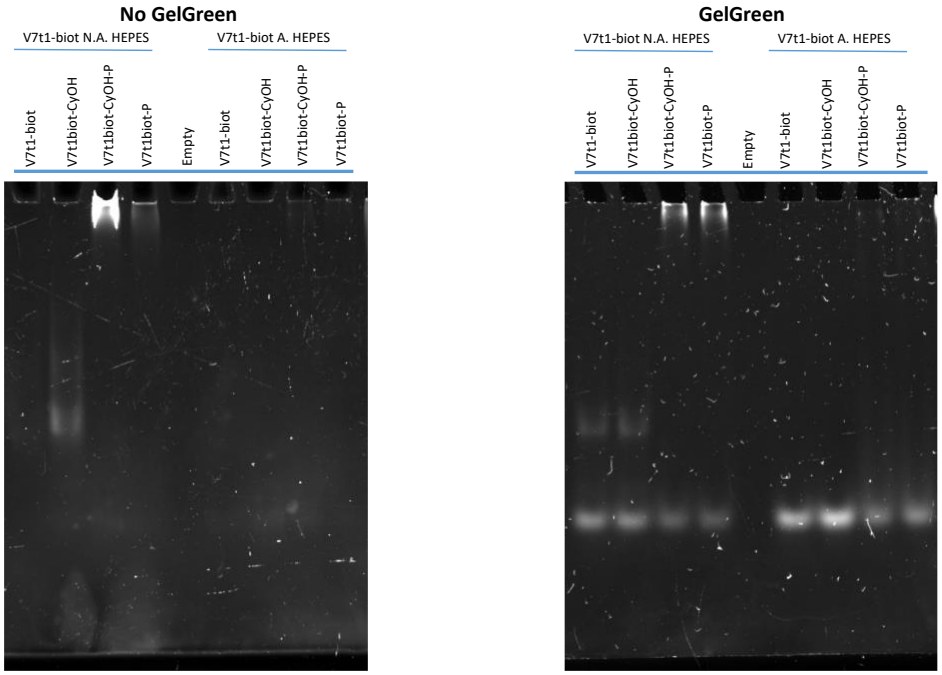

Figure 21. Representative EMSA experiment, with the gel visualized first without staining (No GelGreen, on the left) and then after addition of GelGreen staining, on A. and N.A. V7t1-biotin samples (30 pmol) incubated with CyOH (30 pmol) and $VEGF_{165}$ (40 pmol) in HEPES/Na^+ buffer. The letter P in the figure indicates the protein $VEGF_{165}$. The gel was run at constant 45 V for 2.5 h with TAE 1x as running buffer (210).

3.2.2 Synthesis of the cyanine derivative CyOH

The cyanine CyOH is a fluorescent probe already described in literature as a valuable tool in the biological context (209). It is a derivative of TO which maintains the central chromophore of this molecule, necessary for G-quartet recognition, but is decorated with a *n*-propyl linker functionalized with a terminal hydroxyl group on the quinolinium ring of TO in lieu of the methyl group. This longer polar appendage provides better solubility in aq. solutions, lower aggregation propensity and ability to form additional hydrogen bonds with the target compared to the parent TO. CyOH was synthesized by

modifying a literature protocol with the aim of improving the reaction yields and simplifying the working conditions. As first step, 4-methylquinoline **1** was alkylated with 3-iodopropan-1-ol in ethanol (Scheme 1, step a), rather than with the corresponding bromo derivative, thus leading to compound **2** in better yields (90 %) compared to the previously reported ones. In parallel, benzothiazolium iodide **3** was reacted with methyl iodide to give 1-methylbenzothiazolium iodide **4** (Scheme 1, step b). The final condensation between **2** and **4** was carried out in ethanol in the presence of triethylamine (TEA) at r.t. for 90 min (Scheme 1, step c), adapting the procedure used for a similar substrate (211). The crude product CyOH was obtained as a precipitate by addition of diethyl ether and was subsequently purified by HPLC. The final target compound was thus isolated in pure form with an overall yield of 77 %, *i.e.* with a relevantly increased yield compared to the 20 % previously reported in the literature (209). All the synthesized compounds were analyzed by analytical HPLC, always showing >95 % purity, and characterized by UPLC-ESI-MS and ^{1}H NMR analysis, which fully confirmed their identity, also in comparison with literature data (212, 213).

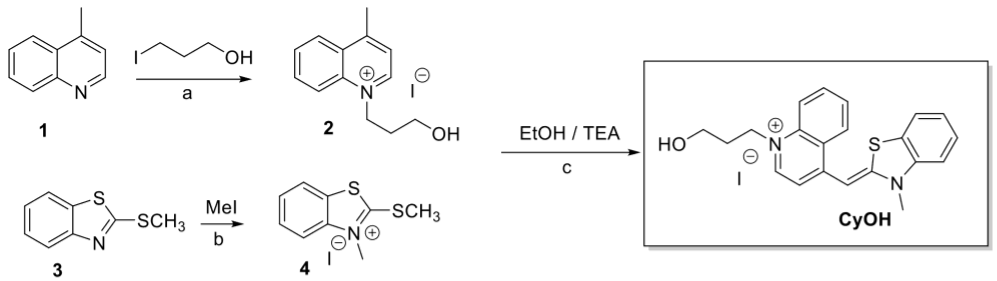

Scheme 1. Synthetic scheme for the preparation of the CyOH probe: a) 3-iodo-1-propanol in ethanol (2.5 eq.), reflux, 72 h; b) MeI (3 eq.), 100 °C, 15 h; c) EtOH/TEA, r.t., 90 min (210).

3.2.3 UV-vis spectroscopic analysis of CyOH and CyOH-V7t1 and 3R02 complexes

UV-vis spectra of CyOH in water and in HEPES/Na^+ buffer from 4 to 36 μM were recorded to determine its absorbance properties (Figure 22). CyOH showed a main band at 504 nm and a weaker vibronic shoulder at 476 nm, similarly to TO (214, 215). Plotting the absorbance values of CyOH at 504 nm *vs*. concentration for both the conditions explored, a linear trend was obtained in accordance with the Beer-Lambert law, thus allowing to exclude the formation of aggregates even at high concentrations (Figure 22). Titrations were then carried out by adding to a fixed concentration of CyOH (8 μM), increasing amounts of V7t1 or 3R02, previously annealed or not in HEPES/Na^+ buffer, up to 8 μM. Here, hypochromic effects were observed at very high CyOH/aptamer ratios, with intensity reduction of the band at 504 nm, then followed by progressive bathochromic shifts of the maxima to 516 nm for the N.A. and to 512 nm for the A. aptamers, and final hyperchromism, allowing the recovery of most of the original CyOH signal intensity at CyOH/aptamer 1:1 ratio (Figure 23). G4-induced hypochromicity in the UV spectrum of the dye is diagnostic of ligand binding to DNA through π-π stacking interactions (216, 217). These results suggested a model in which CyOH is not self-aggregated and binds the terminal G-quartets of the G4s at 1:1 CyOH/aptamer ratio.

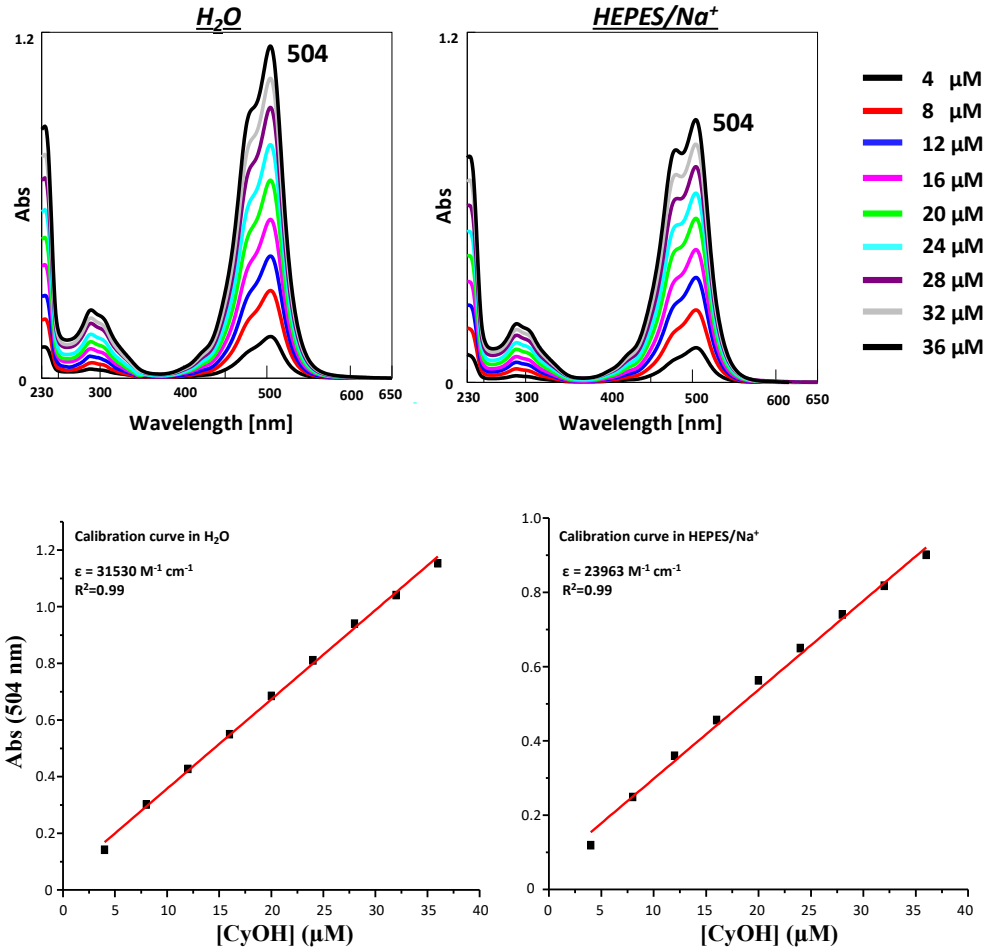

ε (504 nm) H_2O	31530 M^{-1} cm^{-1}
ε (504 nm) HEPES/Na^+	23963 M^{-1} cm^{-1}

Figure 22. Overlapped representative UV-vis spectra of CyOH at various concentrations recorded at r.t. in H_2O and in HEPES/Na^+ buffer and related calibration curves, obtained reporting the maximum absorbance values of the band at 504 nm as a function of CyOH concentration (210).

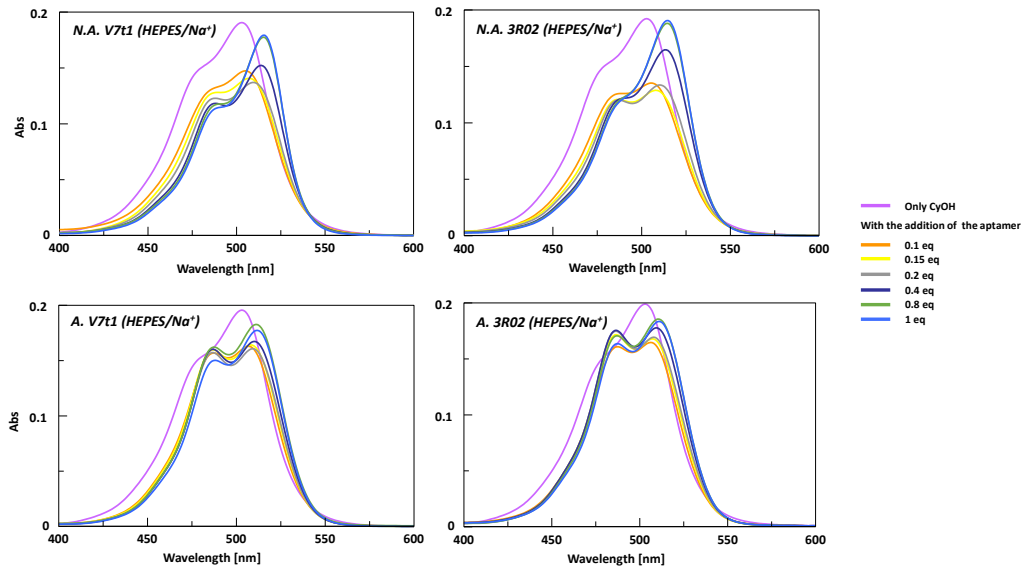

Figure 23. Overlapped representative UV-vis absorption spectra of a 8 μM solution of CyOH in HEPES/Na^+ buffer titrated with increasing amounts of N.A. or A. V7t1 and 3R02 (up to 1 equivalent) (210).

3.2.4 Evaluation of the interaction of CyOH with V7t1 and 3R02 by polyacrylamide gel electrophoresis (PAGE) analysis

To characterize the interaction of CyOH with N.A. and A. V7t1 in terms of molecularity of the species in solution, native gel electrophoresis experiments were performed, analyzing the samples at 1:1 DNA/probe ratio in the selected HEPES/Na^+ buffer. Specific staining for nucleic acids (GelGreen) showed two main bands for N.A. V7t1, attributable to the presence of monomeric and dimeric G4 structures (Figure 24, GelGreen, lane 1), whereas after annealing the retarded band disappeared, indicating the exclusive formation of a monomeric G4 form (Figure 24, GelGreen, lane 3), in accordance with our

previous findings (126). Noteworthy, the addition of 1 eq. of CyOH to both N.A. and A. V7t1 samples did not alter the molecularity of the systems or the monomer/dimer ratio (Figure 24, GelGreen, lanes 2 and 4). Interestingly, a strong selective fluorescent signal in correspondence of the retarded aptamer bands of the samples containing the probe was observed without staining under a UV transilluminator (Figure 24, No GelGreen, lane 2). This means that CyOH is able to give a marked fluorescence light-up but only upon binding to dimeric V7t1, which is the most relevant species for $VEGF_{165}$ target recognition, as demonstrated in our previous studies (126) and in the above reported chemiluminescence-based analysis. A titration experiment was also carried out by adding increasing amounts of CyOH up to 2 eq. to N.A. V7t1 in HEPES/Na^+, showing increasing fluorescence intensity of the complex up to 1:1 aptamer- CyOH ratio, and then an essentially constant fluorescence intensity when in excess of the probe (Figure 25). The same experiments were also carried out to characterize N.A. and A. 3R02 upon CyOH interaction at 1:1 DNA:probe ratio in HEPES/Na^+. GelGreen staining showed a band attributable to monomeric species and multiple retarded bands indicative of the presence of both dimeric and multimeric G4 structures (Figure 26, GelGreen, lane 1). As observed for V7t1, upon annealing the retarded bands disappeared, indicating that, after an heating procedure, the formation of dimeric and multimeric species upon a successive cooling cycle was prevented (Figure 26, GelGreen, lane 2). Also in the case of 3R02, in both N.A. and A. form, the addition of 1 eq. of CyOH did not alter the molecularity and monomer/dimer ratio of the systems (Figure 26, GelGreen, lanes 3 and 4). Moreover, it allowed the visualization of a strong fluorescent signal only in correspondence of the retarded bands without staining solution under UV transilluminator,

demonstrating a selective light-up of the probe when bound to the dimeric and higher-order species of 3R02 (Figure 26, No GelGreen, lane 3).

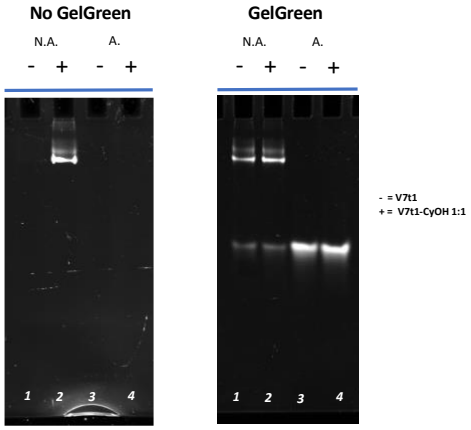

Figure 24. Representative 20% polyacrylamide gel electrophoresis analysis under native conditions of 3.6 μM V7t1 in HEPES/Na^+ buffer. The gel was run at constant 80 V for 3 h at r.t. with TBE 1x as running buffer. N.A. and A. V7t1 samples were loaded in lanes 1 and 3, respectively, whereas the 1:1 complexes of N.A. and A. V7t1 with CyOH were loaded in lanes 2 and 4, respectively (210).

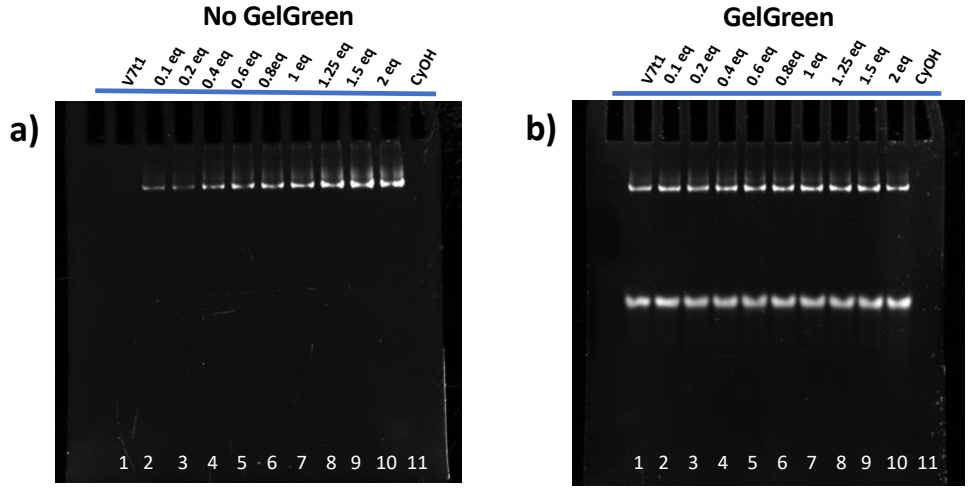

Figure 25. Representative 20% polyacrylamide gel electrophoresis analysis under native conditions of N.A. V7t1 at 3.6 μM concentration alone (lane 1) and in the presence of increasing amounts of CyOH (lanes 2 to 10) in HEPES/Na^+. No band was observed for CyOH alone (3.6 μM, lane 11) under the explored conditions. The gel was visualized first **(a)** without staining and then **(b)** with GelGreen staining. The gel was run at constant 80 V for 3 h at r.t. with TBE 1x as running buffer (210).

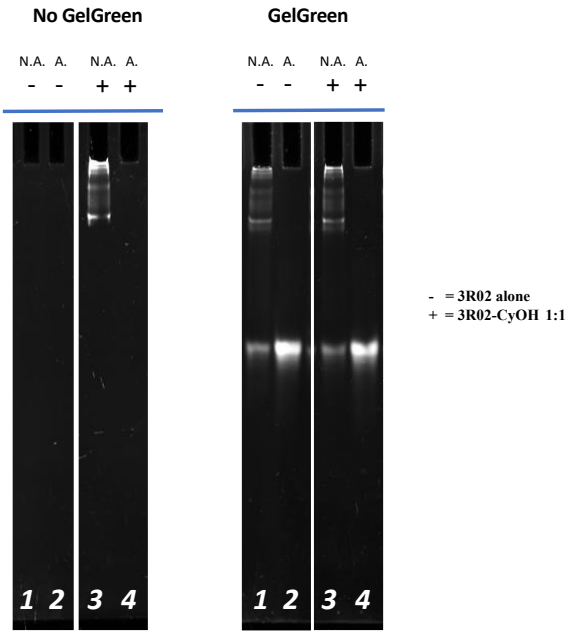

Figure 26. Representative 20% polyacrylamide gel electrophoresis analysis under native conditions of 3.6 μM 3R02 in HEPES/Na^+ buffer. The gel was run at constant 80 V for 3 h at r.t. with TBE 1x as running buffer. N.A. and A. 3R02 samples were loaded in lanes 1 and 2, respectively, whereas the 1:1 complexes with CyOH of the N.A. and A. 3R02 were loaded in lanes 3 and 4, respectively (210).

Finally, we also performed a native gel of N.A. V7t1 and 3R02, both with and without CyOH, dissolved in DMEM, a buffer typically used for cell assays, supplemented or not with 10% fetal bovine serum. The results were fully comparable to the ones found in HEPES/Na^+, showing that the dimeric (and also multimeric for 3R02) aptamers and their selective fluorescence light-up in the presence of CyOH were observed also varying the solution conditions (Figure 27).

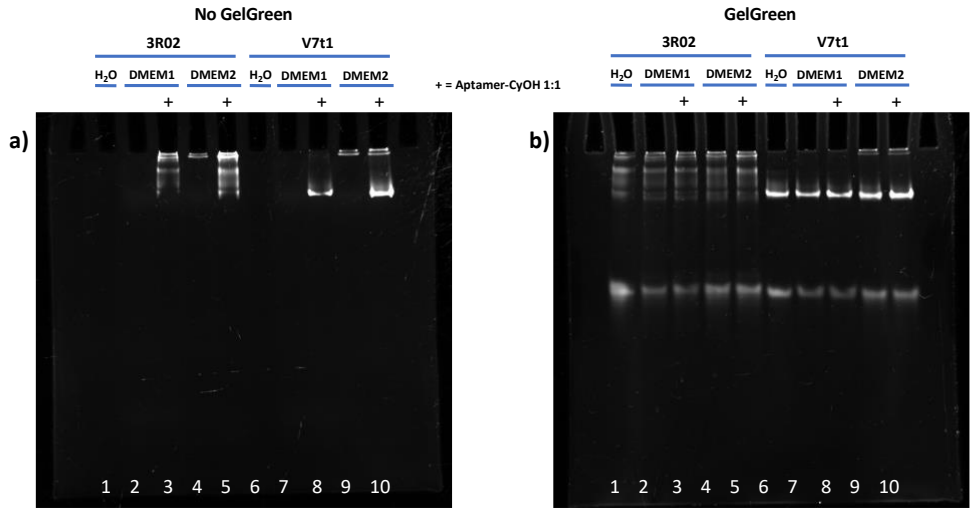

Figure 27. Representative 20% polyacrylamide gel electrophoresis analysis under native conditions of N.A. 3R02 or V7t1 (3 μM) in H_2O (lanes 1 and 6, respectively), DMEM1 (lanes 2-3 and 7-8, respectively) and DMEM2 (lanes 4-5 and 9-10, respectively). N.A. 3R02-CyOH samples were loaded in lanes 3 and 5; N.A. V7t1-CyOH samples were loaded in lanes 8 and 10. DMEM1: DMEM (Dulbecco′s Modified Eagle′s Medium) without supplementation; DMEM2: DMEM with supplementation (10% fetal bovine serum). The gel was visualized first **(a)** without staining and then **(b)** with GelGreen staining. The gel was run at constant 80 V for 3 h at r.t. with TBE 1x as running buffer (210).

3.2.5 Evaluation of the interaction of CyOH with V7t1 and 3R02 by fluorescence spectroscopy analysis

The interaction of CyOH with both N.A. and A. V7t1 and 3R02 samples in HEPES/Na^+ was then evaluated by fluorescence spectroscopy analysis. The fluorescence titrations were performed by adding increasing amounts of each aptamer, up to 4 μM, to a fixed concentration of CyOH (2 μM). The CyOH alone showed a weak-to-null fluorescence signal when excited at 504 nm (Figure 28, black line). Interestingly, in all the conditions explored, a comparable emission band with a maximum at 534 nm progressively increased in intensity by adding increasing amounts of the aptamers (Figure 28, colored

lines) suggesting a ligand-aptamer binding via π-π stacking interactions, in agreement with the UV–vis titration data (Figure 22). The obtained results demonstrated that CyOH interacted with both dimeric (also multimeric for 3R02) and monomeric V7t1 and 3R02 with a similar binding mode, even if with a different fluorescent response. As a matter of fact, the interaction of the probe with dimeric/multimeric G4s gave a fluorescence light-up almost doubled compared to the monomeric ones, in accordance with the PAGE analysis (Figures 24 and 26).

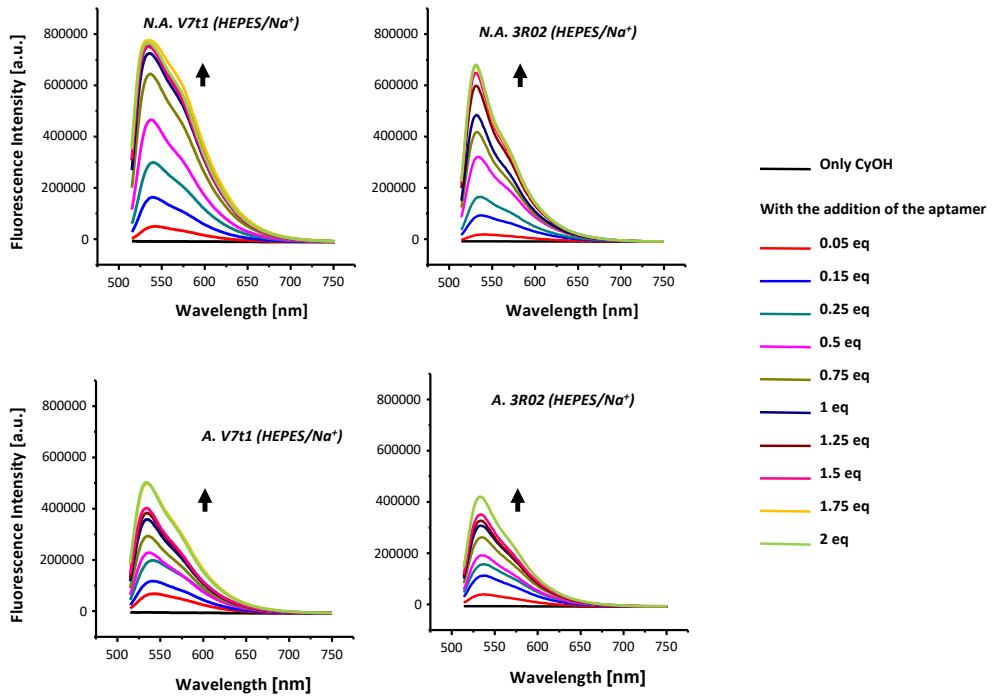

Figure 28. Representative fluorescence emission spectra obtained by adding increasing amounts of N.A. or A. V7t1 and 3R02 (from 0 to 2 eq.) to a 2 μM solution of CyOH (excitation wavelength: 504 nm, entrance and exit slit: 3 nm) in HEPES/Na^+ buffer (210).

We also determined the fluorescence quantum yield of the CyOH alone and when bound to N.A. or A. V7t1 in HEPES/Na^+ in a 1:1 ratio, *i.e.* when the aptamer is mainly dimeric or only monomeric, respectively. The aim was to quantitatively describe the fluorescence enhancement related to the binding of CyOH to the aptamers in the studied conditions. As expected, the fluorescence quantum yield of the probe alone in solution is negligible (Φ_i = 0.02 %), whereas this value remarkably increased when the probe was bound to A. V7t1 (Φ_x = 14 %) and particularly to N.A. V7t1 (Φx = 27 %) (Figure 29). Indeed, it is interesting to highlight that the fluorescence quantum yield value relative to the N.A. V7t1-CyOH 1:1 complex is ca. twice the one of the A. V7t1-CyOH complex, demonstrating on a quantitative basis the selective fluorescence light-up of the probe upon interaction with dimeric V7t1, in accordance to the fluorescence titration data. Remarkably, the fluorescence quantum yield registered for N.A. V7t1 is comparable with the values reported in the literature for the most efficient fluorescent G4 ligands (218, 219).

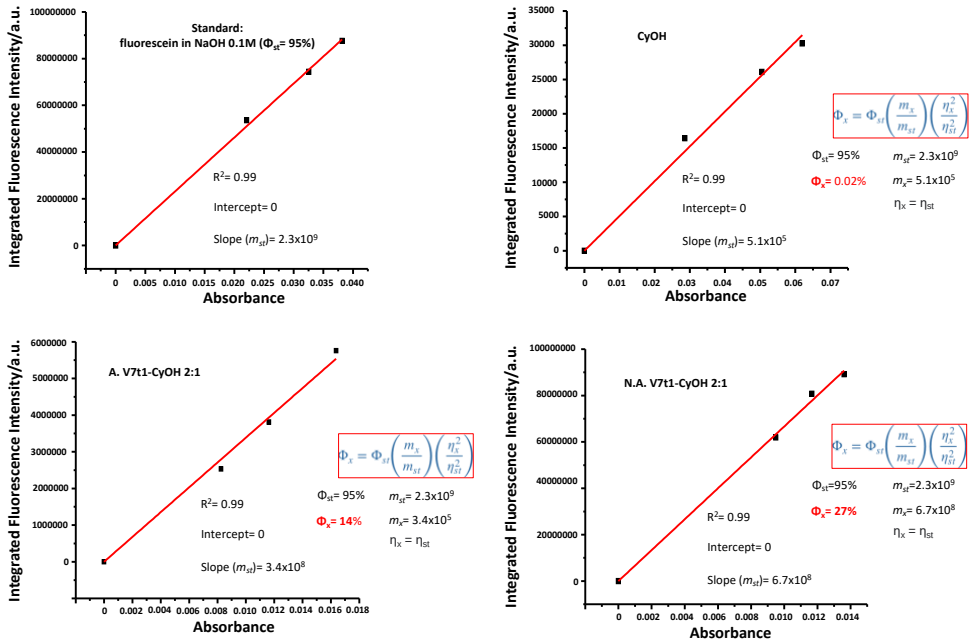

Figure 29. Linear fits for the integrated fluorescence intensity of fluorescein, CyOH, N.A. V7t1-CyOH and A. V7t1-CyOH *vs*. absorbance, for the determination of the related fluorescence quantum yields values. Φ_{st} is the quantum yield of fluorescein in a 0.1 M NaOH solution (Φ_{st} = 95 %), m_x is the slope of a linear fit for the integrated fluorescence intensity of CyOH alone or V7t1-CyOH complexes *vs*. absorbance, m_{st} is the slope of a linear fit for the integrated fluorescence intensity of fluorescein *vs*. absorbance, n_x is the refractive index of HEPES (n_i = 1.33), n_{st} is the refractive index of a 0.1 M NaOH solution (n_{st} = 1.33) (210).

With the aim to have further information about the interaction mode of CyOH with the investigated aptamers, we also performed a fluorescence spectroscopy-based displacement assay using ThT as a model ligand. ThT is a known dye with almost null fluorescence when free in solution, able to produce a fluorescence light-up signal upon π-π stacking interactions with the terminal G-quartets of G4 structures (220–222). In these experiments we added to preformed N.A. or A. V7t1-ThT and 3R02-ThT 1:1 complexes (at 4 uM concentration) increasing amounts of CyOH up to 8 μM concentration, observing a progressive decrease of the fluorescence signal of ThT and the

concomitant appearance of new fluorescence bands in the 525–550 nm region, attributable to the aptamer-CyOH complexes (Figure 30). This finding clearly suggested that CyOH binds to the investigated aptamers essentially via the same binding mode used by ThT, *i.e.* π-π stacking interactions on terminal G-quartets of G4 structures, displacing it from its preferred binding sites (223, 224).

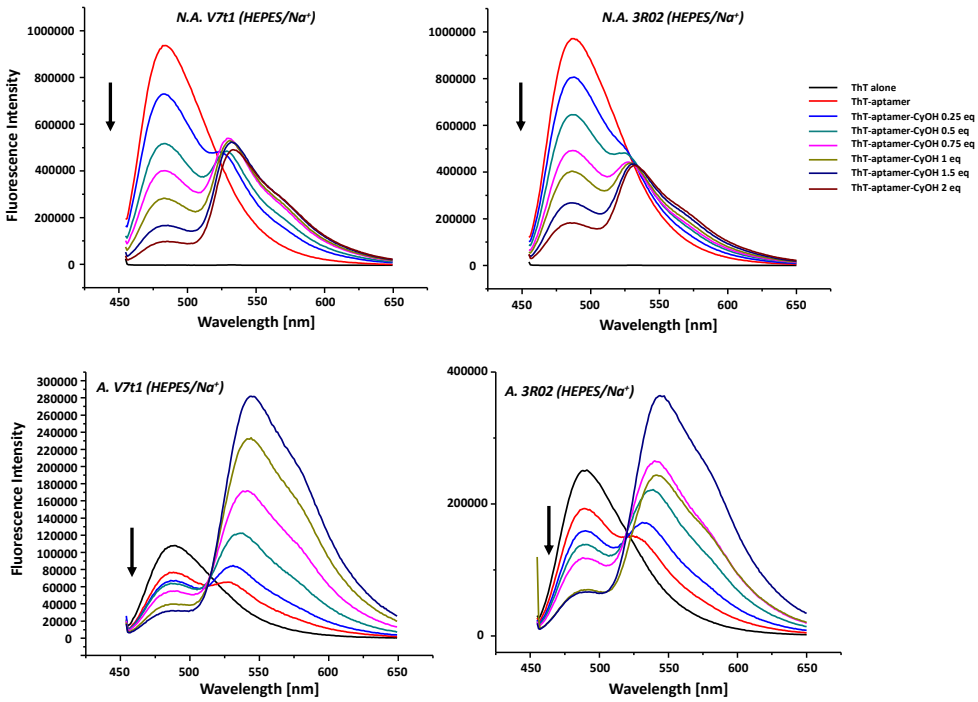

Figure 30. Representative fluorescence emission spectra obtained by adding increasing amounts of CyOH up to 2 eq (8 μM concentration) to preformed N.A. and A. V7t1-ThT or 3R02-ThT 1:1 complexes (excitation wavelength: 450 nm, entrance and exit slit at 3 nm) in HEPES/Na^+ buffer (210).

3.2.6 Evaluation of the interaction of CyOH with V7t1 and 3R02 by CD spectroscopy analysis

To analyze the effect of CyOH binding on N.A. and A. V7t1 and 3R02 conformations, a CD analysis was performed. The aptamers alone in solution showed CD profiles indicative of mostly parallel G4 structures when in N.A. form, and mainly antiparallel G4 conformation after annealing, as confirmed by the deconvolution analysis reported in Figure 31. By adding to a fixed concentration of V7t1 or 3R02 (2 μM) increasing amounts of CyOH up to 10 eq., the N.A. oligonucleotides showed limited-to-null variation of the CD band centered at 263 nm, indicating no detectable change of the parallel G4 folding of the aptamers (225). On the other hand, the A. aptamers showed a progressive decrease of the CD band centered at 299 nm, typical of antiparallel G4 structures, together with an increase of the maximum at 263 nm, thus indicating a net conformational switch – induced by the ligand in a concentration-dependent mode – of the target aptamers from mainly antiparallel to parallel G4 structures (Figures 32 and 33) (225). This conformational switch from antiparallel to parallel G4 structures can be explained, according to the literature, as the result of the more efficient ligand binding to the terminal G-quartets of parallel G4 structures, better exposed and thus more prone to give intense π-π stacking interactions with a ligand than antiparallel G4 structures (226–229). Moreover, the presence of induced circular dichroism (ICD) signals gave us additional information on G4/ligand interactions. The CD profiles for all the investigated systems with aptamer-CyOH ratios higher than 2:1 showed a positive ICD band with a maximum centered at 516 nm and a negative ICD band with a minimum at 475 nm, more pronounced for the A. than for the N.A. aptamers (Figure 32). The bisignate

ICD signals indicate aggregation of the dye when bound to the aptamers, with probably one type of aggregate, most likely dimeric, as suggested by the presence of a well-defined isodichroic point in the ICD bands (230, 231). The higher intensity of the ICD signals in the A. vs. N.A. aptamer forms is a consequence of the fact that, at high ligand ratios, when the aptamers are monomeric, binding at G4 loops and/or grooves, in addition to end-stacking mode, could be relevant. On the other hand, the interaction with the dimeric aptamers occurs essentially via end-stacking onto the outer G-quartets of the dimer (230).

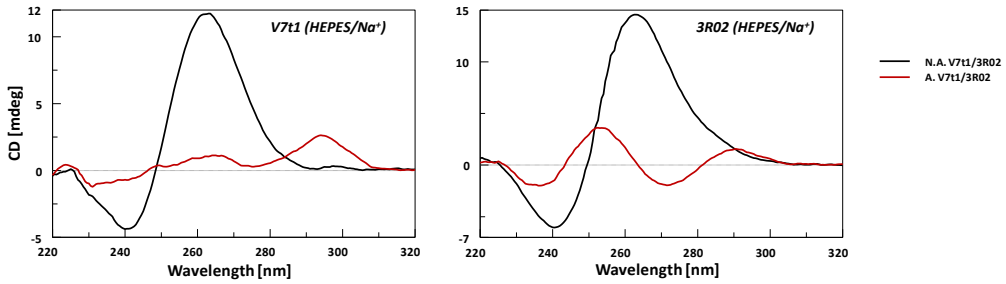

	Parallel	Hybrid	Antiparallel
V7t1 N.A.	90	0	8
V7t1 A.	35	0	63
3R02 N.A.	76	17	5
3R02 A.	32	0	66

Figure 31. Overlapped CD spectra of N.A. and A. V7t1 (on the left) and 3R02 (on the right) in HEPES/Na^+ buffer and prediction of the relative abundance of the different G-quadruplex topologies adopted by V7t1 and 3R02 obtained by singular value decomposition (SVD) analysis of the CD spectra recorded in HEPES/Na^+, performed by exploiting the software developed by del Villar-Guerra *et al.* (232). Deviations from 100% (± 1%) are due to significant digits approximation of the values originally obtained by the simulations (210).

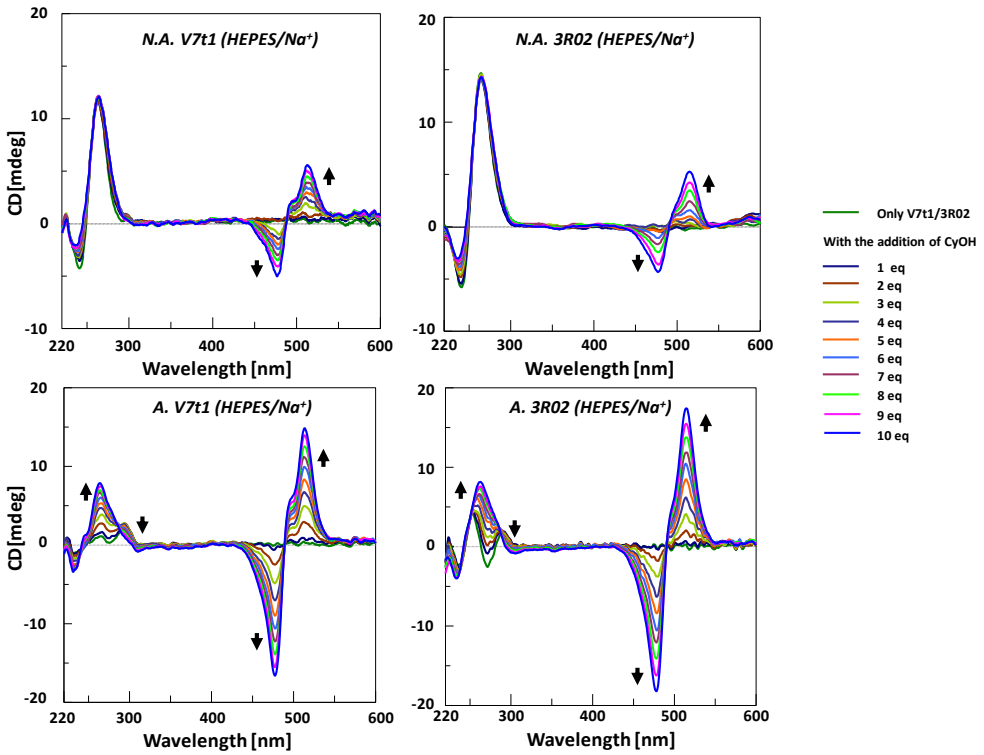

Figure 32. Overlapped representative CD spectra obtained by adding increasing amounts of CyOH (up to 10 eq.) to a 2 μM solution of N.A./A. V7t1 and 3R02 aptamers in HEPES/Na^+ buffer (210).

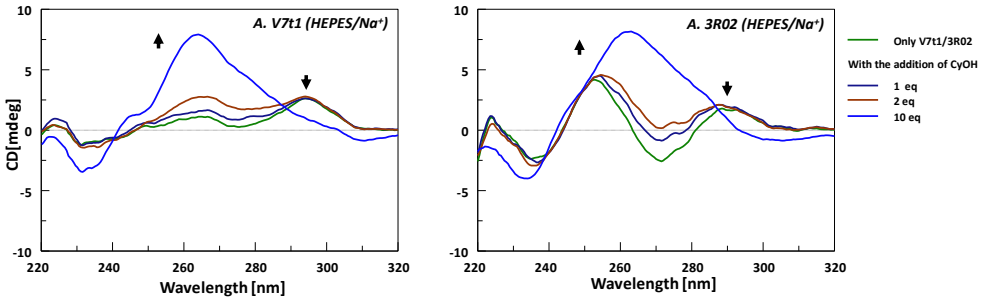

Figure 33. Overlapped representative CD spectra obtained in titration experiments by adding increasing amounts of CyOH (1, 2, 10 equiv.) to a 2 μM solution of A. V7t1 or 3R02 in HEPES/Na^+ buffer (210).

CD-melting experiments were then performed to evaluate the thermal stability of the V7t1 or 3R02-CyOH complexes at 1:1 DNA:probe ratio by monitoring the CD signal at 263 nm in the 15-90 °C range (Figure 34). The CD-melting profile showed a clear stabilizing effect of CyOH on N.A. V7t1 in HEPES/Na^+, even though, similarly to the aptamer alone, a complete denaturation of its G4 structure was not obtained even at 90 °C and apparent $T_{1/2}$ values could not be determined (126). The probe CyOH was also able to stabilize N.A. 3R02, with apparent $T_{1/2}$ > 80 °C. For both A. V7t1 and 3R02 aptamers in HEPES/Na^+, a CD-melting profile could not be obtained since at 1:1 DNA:probe ratio both the maxima, at 299 and 263 nm, were very low.

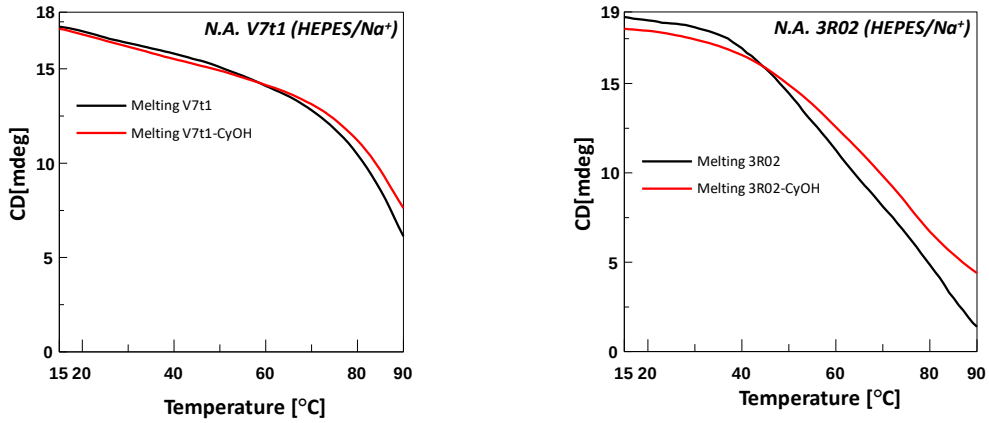

Figure 34. Representative CD-monitored melting curves, registered at 263 nm, of V7t1 and 3R02 alone and of the 1:1 V7t1-CyOH or 3R02-CyOH complexes in HEPES/Na^+ buffer (210).

3.2.7 Binding studies on the interaction of V7t1-CyOH and 3R02-CyOH with $VEGF_{165}$ by electrophoretic analysis

To verify if V7t1 bound to CyOH was still able to recognize $VEGF_{165}$, EMSA experiments under non-denaturing conditions were performed (233). N.A and A. V7t1 samples in the presence of 1 eq. of CyOH were incubated with 1.3 eq. $VEGF_{165}$, analysing the resulting mixtures by PAGE using the free oligonucleotide as control. GelGreen staining, able to reveal nucleic acids, showed the disappearance of the dimeric bands relative to dimeric V7t1, with the concomitant appearance of a new retarded band in the samples containing $VEGF_{165}$ (Figure 35, GelGreen, lanes 3 and 4). However, no change in the intensity of the faster migrating bands relative to monomeric V7t1 was observed (Figure 35, GelGreen, *cfr.* lanes 3 and 4 with lanes 1 and 2). Interestingly, without staining, it was possible to appreciate the strong fluorescence signal of CyOH in correspondence of the retarded band attributable to the aptamer-CyOH-protein complex in the lane where N.A. V7t1, CyOH and $VEGF_{165}$ had been loaded (Figure 35, No GelGreen, lane 3), demonstrating a strong preference of $VEGF_{165}$ for dimeric over monomeric V7t1 (126) also when the aptamer was bound to the selected cyanine probe. An EMSA experiment was performed under the same conditions on the biotinylated V7t1 aptamer, here used to determine the affinity for $VEGF_{165}$, as reported in Figure 19.

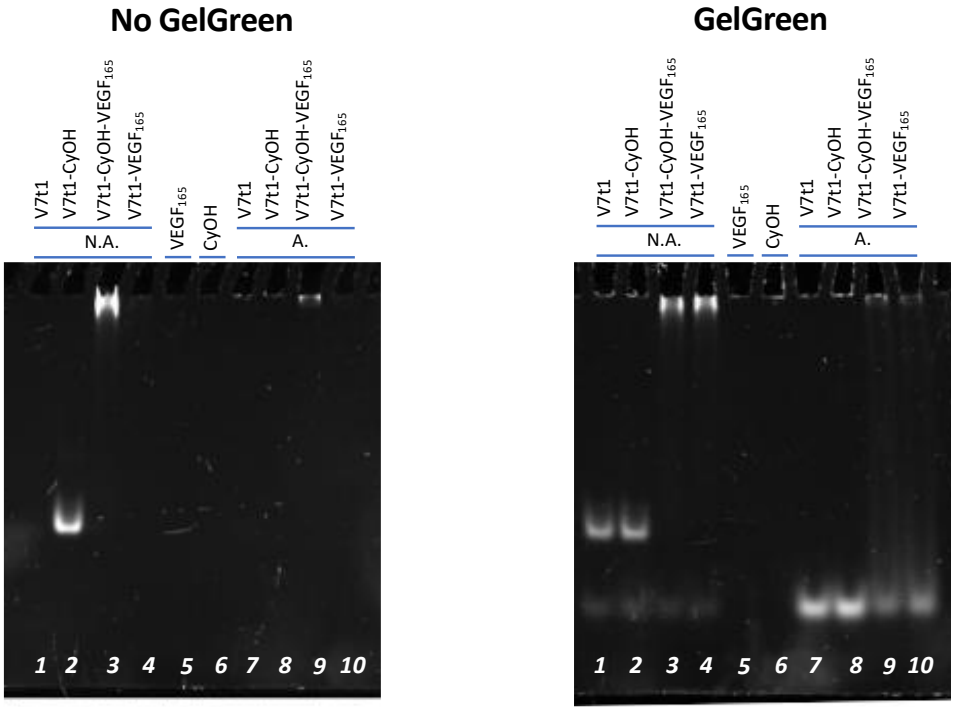

Figure 35. Representative unstained (No GelGreen) and GelGreen-stained EMSA of A. and N.A. V7t1 (30 pmol) incubated with CyOH (30 pmol) and $VEGF_{165}$ (40 pmol) in HEPES/Na^+ buffer. N.A. V7t1 was loaded in lanes 1-4 and A. V7t1 in lanes 7-10**.** The gel was run at constant 45 V for 2.5 h with TAE 1x as running buffer (210).

No differences were observed in the protein recognition capacities of V7t1 if free or functionalized with a biotin tag at its 3′-end (Figure 36). An EMSA experiment was also performed to examine the ability of 3R02 to recognize $VEGF_{165}$ when bound to CyOH. N.A. and A. 3R02 samples in HEPES/Na^+ in the presence of 1 eq. of CyOH were incubated with 1.3 eq. $VEGF_{165}$ and the resulting mixtures were analyzed by PAGE using free 3R02 and V7t1 oligonucleotides as controls. By using the GelGreen staining, we were able to appreciate the selective disappearance of the slower-migrating bands relative to dimeric/multimeric aptamer G4 forms (Figure 37, GelGreen, *cfr*. lane 3 with 7, and lane 5 with 1) and the concomitant appearance of retarded bands relative

to the protein complexes (Figure 37, GelGreen, lanes 3, 4, 5 and 6). On the other hand, only a slight change of the faster-migrating bands of monomeric 3R02 was observed (Figure 37, GelGreen, *cfr*. lane 4 with 8, and lane 6 with 2). Interestingly, without staining, it was possible to appreciate the strong fluorescence signal of CyOH in correspondence of the new retarded bands, which were attributed to the cyanine-aptamer-protein complex in the system containing N.A. 3R02, CyOH and $VEGF_{165}$ (Figure 37, No GelGreen, lane 3). The overall results, revealing that only the dimeric or higher-order G4 structures of the selected aptamers showed a very good recognition ability of the target protein, let us conclude that the multiple retarded bands observed in N.A. 3R02 sample are probably dimers and multimers that, similarly to the dimeric V7t1, are largely preferred by $VEGF_{165}$ with respect to monomeric 3R02.

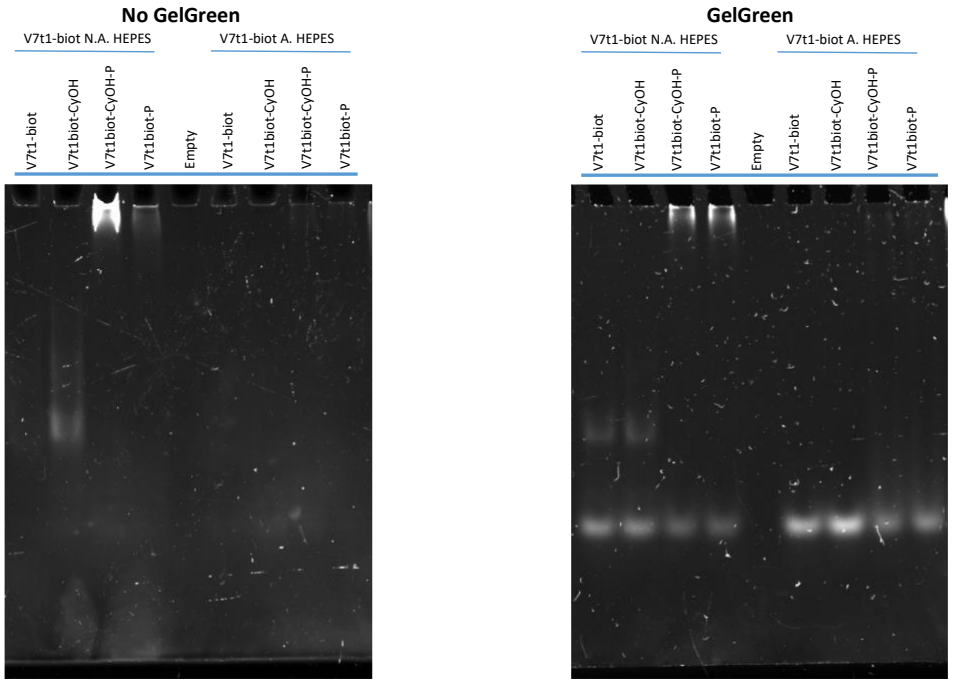

Figure 36. Representative EMSA experiment, with the same gel visualized first without staining (No GelGreen, on the left) and then after addition of GelGreen staining, on A. and N.A. V7t1-biotin samples (30 pmol) incubated with CyOH (30 pmol) and $VEGF_{165}$ (40 pmol) in HEPES/Na^+ buffer. The letter P in the figure indicates the protein $VEGF_{165}$. The gel was run at constant 45 V for 2.5 h with TAE 1x as running buffer (210).

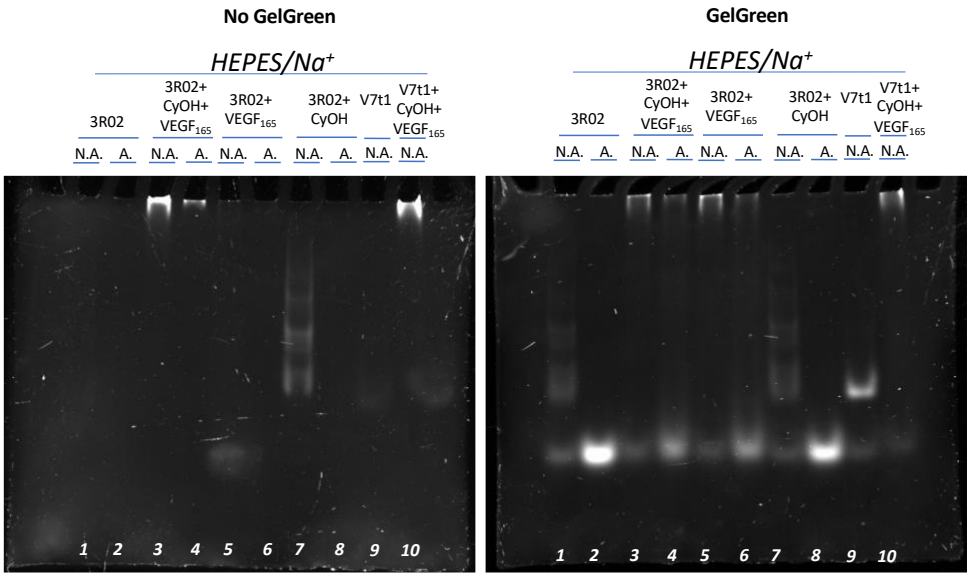

Figure 37. Representative EMSA experiment, with the same gel visualized first without staining (No GelGreen, on the left) and then after addition of GelGreen staining (GelGreen, on the right), on A. and N.A. 3R02 samples (30 pmol) incubated with CyOH (30 pmol) and $VEGF_{165}$ (40 pmol) in HEPES/Na^+ buffer. The gel was run at constant 45 V for 2.5 h with TAE 1x as running buffer (210).

3.2.8 Biological studies

MTT *in vitro* assays (see experimental part) were performed on MCF-7 breast cancer cells, using non-tumorigenic MCF- 10A cells as control, to evaluate the antiproliferative activity of the complexes V7t1-CyOH and 3R02-CyOH on cancer and healthy cells. The obtained results indicated that CyOH alone exerted significant dose-dependent toxic effects on both cancer and normal cells, with similar IC_{50} values (28 and 30 μM, respectively) after 48 h incubation. On the other hand, much lower toxicity was observed for the aptamer-CyOH complexes tested on the same cell lines, particularly on the healthy cells, with cell viability of ca. 60 and 75 %, respectively for MCF-7 cells treated with V7t1-CyOH or 3R02-CyOH at 30 μM, and ca. 90 % for MCF-10A cells under the same conditions (Figure 38). The selectivity of the

aptamer-CyOH systems for cancer over non-cancer cells indicated a good *in vitro* stability of these complexes, with no relevant release of free CyOH within the cells.

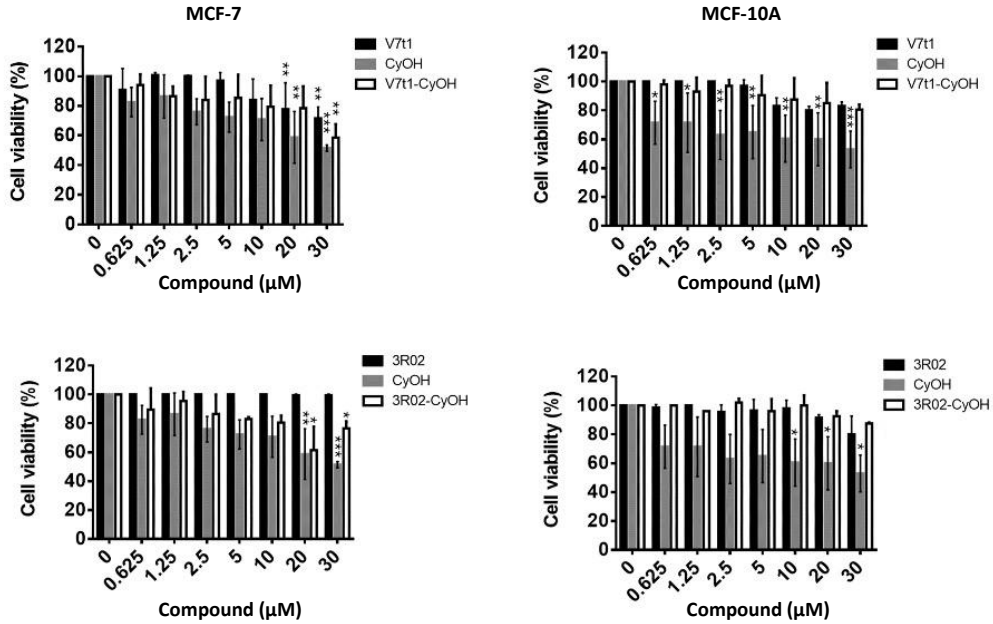

Figure 38. Effects of increasing concentrations of CyOH, nude aptamers and aptamer-CyOH complexes (0 - 30 μM) on the viability of MCF-7 human breast cancer and non-tumorigenic MCF-10A cells upon 48 h of incubation. Cell viability values are expressed as the percentage of cell viability obtained for treated vs. control cells grown in the absence of the tested molecules. Three independent experiments were performed and, for all the experimental points, *P < 0.05, **P < 0.01 or ***P < 0.001 were obtained for treated *vs.* control samples (210).

With the aim of evaluating how CyOH and the V7t1-CyOH and 3R02-CyOH complexes were internalized in the tested cell lines, CLSM experiments were performed. Using the studied systems at 5 μM concentration, which ensured cell viability above 70 %, MCF-7 breast cancer cells were incubated at different times (3, 6, 9, 24 and 48 h) and then analyzed by CLSM. The results showed that both CyOH, on one side, and V7t1-CyOH and 3R02-CyOH complexes, on the other, were taken up by MCF-7 cancer cells, but with

substantial differences. CyOH alone was internalized rapidly and in an unspecific manner, causing evident toxic effects like nuclei damage, in accordance with the MTT experiments (Figure 39b). On the other hand, N.A. V7t1-CyOH and 3R02-CyOH complexes were more selectively and slower internalized into cells, with a poor toxic activity, in agreement with the MTT assays, which demonstrated that the complexes did not dissociate within cells.

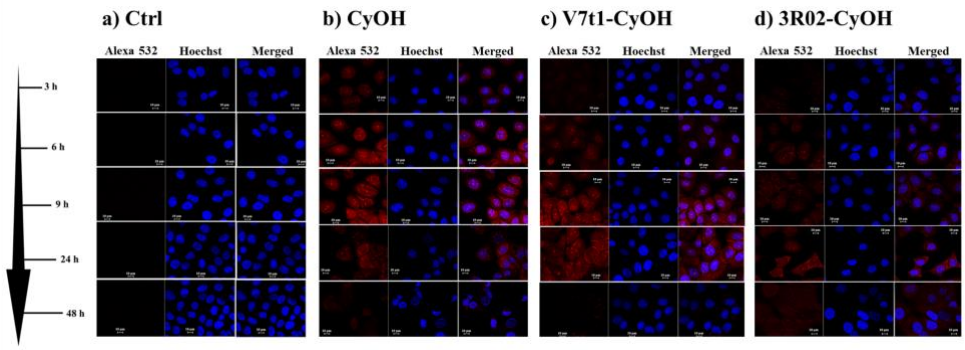

Figure 39. Confocal microscopy images relative to the internalization of CyOH and V7t1-CyOH and 3R02-CyOH complexes into MCF7 cells. a) Control cells; b) cells incubated with CyOH; cells incubated, respectively, with c) V7t1-CyOH and d) 3R02-CyOH complexes. In each panel, column 1 shows the visualization with the Alexa 532 filter suitable to reveal the CyOH dye; column 2 the visualization with the Hoechst filter; column 3 the merge between columns 1 and 2. Cells were cultured on glass coverslips in 24-well plates, grown to semiconfluency and incubated for 3, 6, 9, 24 and 48 h. Cell nuclei were stained by incubating the cells with 0.001 mg/mL Hoechst in PBS 1x for 20 min in the dark. After fixing the cells in 4% paraformaldehyde, these were analyzed by CLSM by using a 63x oil immersion objective (210).

Cellular colocalization experiments were also performed by CLSM on human breast cancer MCF-7 and non-toumorigenic MCF-10A cells to evaluate the ability of the aptameric complexes to specifically recognize the target VEGF-A in cells. In detail, the two cell lines were incubated with the V7t1-CyOH or 3R02-CyOH complexes both at 5 μM concentration for 24 h to have optimal internalization, as shown in the time course experiments reported in Figure 39,

and in parallel with a fluorescently labelled VEGF-A specific antibody. The fluorescent antibody evidenced that VEGF-A was mainly present in the nuclei of MCF-7 cancer cells, whereas it was mainly localized in the cytoplasm of non-toumorigenic MCF-10A cells (Figure 40, CTRL). Interestingly, the same localization was detected by using both V7t1-CyOH and 3R02-CyOH complexes (Figure 40, Alexa 532 columns), demonstrating a good colocalization with the fluorescent anti-VEGF-A antibody (Figure 39, MCF-7 and MCF-10A panels, merged columns, 2nd and 3rd lines) and thus with the target VEGF-A. In detail, in MCF-7 cancer cells incubated with the aptamer-CyOH complexes, the fluorescence signal of the probe was mainly observed in the nuclei and a good colocalization with VEGF-A was detected (Fig. 10, yellow spots in MCF-7 panel, merged columns, 2nd and 3rd horizontal lines). In the healthy MCF-10A cells, the complexes mainly localized in the cytoplasm (Figure 40, yellow spots in MCF-10A panel, merged columns, 2nd and 3rd horizontal lines), whereas CyOH alone did not follow a precise localization pattern (Figure 41). These results supported the hypothesis that the probe alone enters the cells quite easily, unselectively binding DNA and proteins. In contrast, when bound to the aptamers, it is precisely driven to the target protein, in full accordance with the previosuly described EMSA experiments. Taken together, our results confirm the potential of these aptameric systems for the detection of this cancer-related protein, showing an efficiency comparable to the one of a fluorescently-labelled anti-VEGF antibody which is commercially available.

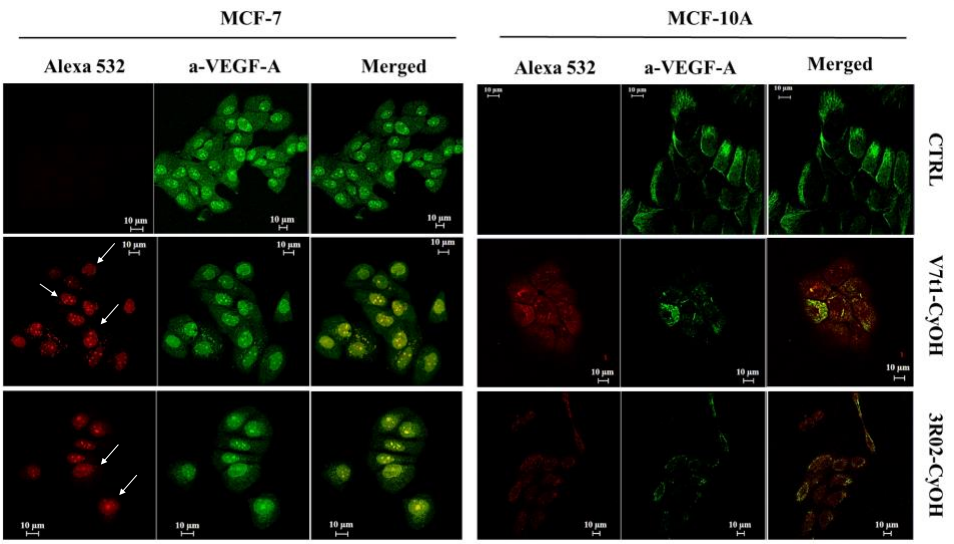

Figure 40. Confocal microscopy images relative to the internalization experiments on V7t1-CyOH and 3R02-CyOH into MCF-7 (left panel) and MCF-10A (right panel) cells. Cells were cultured on glass coverslips in 24-well plates, grown to semiconfluency and incubated for 24 h. VEGF-A was revealed by immunofluorescence experiments by using a fluorescent VEGF-A-specific antibody. After fixing the cells in 4% paraformaldehyde, these were analyzed by CLSM by using a 63x oil immersion objective (210).

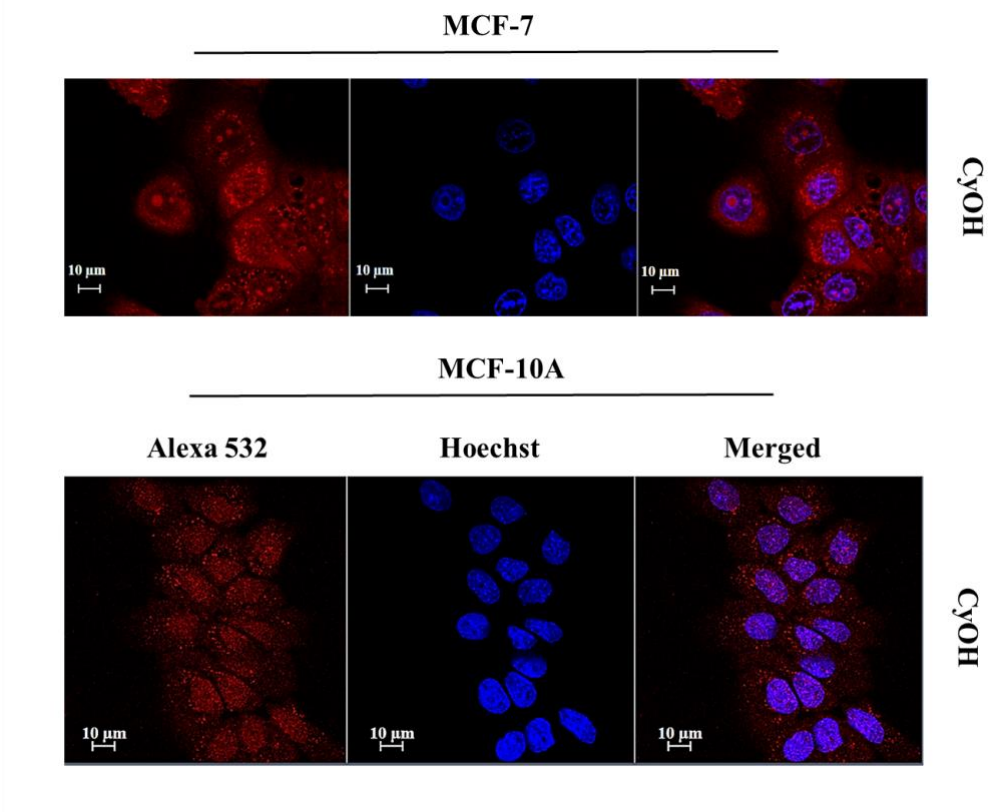

Figure 41. Confocal microscopy images relative to internalization experiments of CyOH into MCF-7 cells (up) and MCF-10A (down) cells. Cells were cultured on glass coverslips in 24-well plates, grown to semiconfluency and incubated for 24 h. After fixing the cells in 4% paraformaldehyde, these were analyzed by CLSM by using a 63x oil immersion objective (210).

3.3 Experimental section

3.3.1 Chemiluminescence-based binding studies on the interaction of V7t1 with $VEGF_{165}$

In these experiments, a copper-coated 96-well plate (Copper Coated High-Capacity Plates, Thermo Scientific) was incubated under gentle shaking for 1 h with 100 μL of 0.2 μM $VEGF_{165}$-His solution in phosphate-buffered saline (PBS: 137 mM NaCl, 2.7 mM KCl, 8.1 mM NaH_2PO_4/ Na_2HPO_4, 1.86 mM KH_2PO_4/K_2HPO_4). After supernatant removal, each well was washed three times using 200 μL of a HEPES/Na^+ solution containing 0.05 % (*v*/v) Tween-20 (Sigma- Aldrich). Then, the wells were incubated for 1 h with 100 μL of distinct solutions at various concentrations of either N.A. or A. V7t1-biotin in HEPES/Na^+ (so to have 2.5, 5.0, 10, 12.5, 15, 20, 30 and 50 pmol of each aptamer form). The supernatant was removed and the wells were washed in the same conditions indicated above. Then, each well was filled with streptavidin-HRP (Horseradish peroxidase, BPS Bioscience) diluted in Blocking Buffer (HEPES/Na^+ with 0.05 % (*v*/v) Tween 20 and 2 % (m/v) BSA) and incubated under gentle shaking for 1 h. The supernatant was then removed and three washings were performed. Finally, enhanced chemiluminescence (ECL) HRP substrate (BPS Bioscience) was added to each well and the HRP activity was measured by a multilabel plate reader (Glomax Discover System, GM3000). All experimental procedures were performed at r.t. in duplicate. The data were reported as a function of DNA concentration. The obtained points were then fitted with an independent and equivalent-sites model (212), using the Origin 8.0 program, with the following equation:

$$\alpha = \left(\frac{1}{2[L]_0}\right)\left\{\left([L]_0 + n[Qu] + \frac{1}{K_b}\right) - \sqrt{\left([L]_0 + n[Qu] + \frac{1}{K_b}\right)^2 - 4[L]_0 n[Qu]}\right\}$$

where α is the mole fraction of the ligand in the bound form, $[L]_0$ is the total ligand concentration, $[Qu]$ is the added DNA concentration, n is the number of the equivalent and independent sites on the DNA structure and K_b is the binding constant. The fraction of the bound ligand was determined by using the following equation:

$$\alpha = \frac{Y - Y_0}{Y_b - Y_0}$$

where Y, Y_0 and Y_b are the values of fluorescence emission intensity at the maximum, respectively, at each titrant concentration, at the initial and final state of the titration.

3.3.2 Synthesis of CyOH: general methods

For HPLC analyses and purifications, an aq. solution containing 0.1% TFA (trifluoroacetic acid) and acetonitrile were used as solvents A and B, respectively. The following methods were used: i) Method 1: first isocratic elution over 17 min with 95% solvent A/5% solvent B, then linear gradient to 60% solvent A/40% solvent B in 3 min, followed by isocratic elution for 2 min and then back to 95% solvent A/5% solvent B for 4 min (λ detection: 230, 256 and 300 nm); ii) Method 2: first isocratic elution over 2 min with 95% solvent A/5% solvent B, then linear gradient to 60% solvent A/40% solvent B in 14

min, followed by linear gradient to 40% solvent A/60% solvent B in 8 min, and then 95% solvent A/5% solvent B isocratic elution for 1 min (λ detection: 256, 300 and 500 nm). ^{1}H- and ^{13}C-NMR spectra were recorded on Bruker Avance 300 MHz. All the chemical shifts (δ) are expressed in ppm with respect to the residual solvent signal for ^{1}H-NMR spectra. UPLC-ESI-MS data were recorded using a surveyor UPLC system equipped with a BEH Acquity UPLC column (1.7 µm, 2.1 x 50 mm), and an LCQ ADV MAX ion-trap mass spectrometer, with an electrospray ionization (ESI) source.

3.3.2.1 Synthesis of 1-(3-hydroxypropyl)-4-methylquinolinium iodide (2)

A mixture of 4-methylquinoline **1** (1 eq, 100 mg, 84 µL, 0.70 mmol) and 3-iodo-1-propanol (2.5 eq, 325 mg, 168 µL, 1.75 mmol) in 700 µL ethanol was refluxed for 72 h. After cooling to r.t. the reaction mixture was treated with the minimum amount of methanol and then diethyl ether was added to allow the precipitation of the target compound as a white solid. The precipitate was collected, washed three times with diethyl ether, and purified by preparative HPLC using isocratic elution with a 95:5 CH_3CN:H_2O/0.1% TFA solution over 24 min. All the HPLC fractions containing the compound of interest were collected and taken to dryness, affording desired product **2** with 90% yield. The comparison of our NMR data with those available in the literature confirmed the identity and purity of the obtained compound (213). **^{1}H-NMR** (300 MHz, CD_3OD): δ (ppm) 2.27 (q, 2H), 3.07 (s, 3H), 3.68 (t, 2H), 5.15 (t, 2H), 7.95 – 8.10 (m, 2H), 8.18 – 8.21 (m, 1H), 8.23 – 8.31 (m, 2H), 9.23 (d, 1H). **UPLC-ESI-MS** (positive mode) m/z: 202.3 (**2** + $1H^+$)$^+$ a.m.u.

3.3.2.2 Synthesis of 3-methyl-2-(methylthio)benzo[d]thiazol-3-ium iodide (4)

Commercially available 2-(methylthio)benzo[d]thiazole **3** (1 eq, 70 mg, 0.39 mmol) was dissolved in methyl iodide (30 eq, 730 µL, 11.6 mmol) at r.t. and the reaction mixture was refluxed at 100 °C for 15 h. A white precipitate was obtained, filtered and repeatedly washed with diethyl ether to give product **4** with a 92% yield. The experimental data for the obtained compound were perfectly in accordance with the literature data, confirming its identity and purity. **^{1}H-NMR** (300 MHz, DMSO-d_6): δ (ppm) 3.12 (s, 3H), 4.10 (s, 3H), 7.71 (t, 1H), 7.83 (t, 1H), 8.19 (d, 1H), 8.40 (d, 1H). **UPLC-ESI-MS** (positive mode) m/z: 196.0 (**4** + H^+)$^+$ a.m.u.

3.3.2.3 Synthesis of (Z)-1-(3-hydroxypropyl)-4-((3-methylbenzo[d]thiazol-2(3H) ylidene)methyl) quinolin-1-ium iodide (CyOH)

1-(3-Hydroxypropyl)-4-methylquinolinium iodide **2** (1 eq, 73.2 mg, 0.362 mmol) was reacted with 3-methyl-2-(methylthio)-1,3-benzothiazol-3-ium iodide **4** (1 eq, 65.9 mg, 0.362 mmol) in 1.5 mL ethanol containing 50.4 µL of triethylamine (TEA). After 90 min under stirring at r.t., the solvent was evaporated under vacuum and the solid repeatedly washed with diethyl ether. The crude was purified by preparative HPLC eluting with Method 2. The desired CyOH probe was obtained with 77% yield as a red solid. Comparison of the experimental with literature data confirmed the identity and purity of the obtained compound (209). **^{1}H-NMR** (300 MHz, DMSO-d_6): δ (ppm) 2.01 (bs, 2H), 3.50 (bs, 2H), 4.02 (s, 3H), 4.66 (t, 2H), 4.82 (m, 1H, OH), 6.94 (s, 1H), 7.36-7.46 (m, 2H), 7.62 (t, 1H), 7.76-7.82 (m, 2H), 8.00-8.09 (m, 2H), 8.15 (d,

1H), 8.61 (d, 1H), 8.81 (d, 1H). **UPLC-ESI-MS** (positive mode) m/z: 349.5 $(CyOH + H^+)^+$ a.m.u.

3.3.3 Oligonucleotide, probe and protein samples

The oligonucleotides: V7t1 (5′TGTGGGGGTGGACGGGCCGGGTAGA3′), 3R02 (5′TGTGGGGGTGGACTGGGTGGGTACC3’) and V7t1-biotin (5′TGTGGGGGTGGACGGGCCGGGTAGA3′-biotin) were purchased as HPLC-purified oligonucleotides from biomers.net GmbH (Germany). The oligomer identity and purity were confirmed by MALDI-TOF mass spectrometry and high-performance liquid chromatography (HPLC) data provided by the commercial supplier. The oligonucleotides were dissolved in ultra-pure nuclease-free water (VWR) and their concentrations were determined by UV-vis analysis measuring the absorbance at 260 nm and 95 °C using the molar extinction coefficients $\varepsilon = 280504\ cm^{-1}M^{-1}$ and $\varepsilon = 270124\ cm^{-1}M^{-1}$ for V7t1 and 3R02, respectively. All the used aptamer solutions were obtained by diluting a stock solution (1 mM) prepared in water with the selected buffer, *i.e.* a pseudo-physiological Na^+-rich buffer (25 mM HEPES, 150 mM NaCl, pH 7.4), here indicated as HEPES/Na^+. Samples of annealed V7t1 and 3R02 were obtained by heating the appropriate oligonucleotide solutions at 95 °C for 5 min and leaving them to cool to r.t. overnight. Not-annealed (N.A.) and annealed (A.) V7t1 and 3R02 samples were then kept at 4 °C until use. The final compound CyOH was dissolved in ultra-pure nuclease-free water (VWR) in all the experiments. Recombinant human $VEGF_{165}$ and His-tag labelled $VEGF_{165}$ ($VEGF_{165}$-His, GenScript) were purchased from Twin Helix srl (Italy). Protein concentration was confirmed by Bradford assay (Bio-Rad) using Bovine Serum Albumin (BSA) as standard.

3.3.4 UV-vis spectroscopy experiments

The UV-vis spectra were obtained on a Jasco V-750 UV-vis spectrophotometer, using 1 cm path length cuvettes (1 mL internal volume, Hellma) and recording in the 230-650 nm range using a scanning speed of 100 nm/min with appropriate baseline subtraction. Titration experiments were carried out using independent solutions at a fixed concentration (8 μM) of CyOH in HEPES/Na^+ buffer. Increasing amounts of N.A. V7t1 or 3R02 up to 8 μM were used, taken from concentrated DNA solutions dissolved in HEPES/Na^+ buffer.

3.3.5 Gel electrophoresis experiments

Acrylamide/bis-acrylamide (19:1) 40% solution, glycerol and GelGreen Nucleic Acid Stain were purchased from VWR. Ammonium persulfate (APS) and tetramethylethylenediamine (TEMED) were purchased from Sigma Aldrich. N.A. and A. V7t1 or 3R02 samples (3.6 μM) in HEPES/Na^+ buffer were loaded on 20% polyacrylamide gels with TBE 1x (Tris–borate–EDTA) as running buffer. CyOH was incubated with the aptamers at 1:1 DNA:probe ratio for 30 min at r.t. just before loading, samples were supplemented with 5% glycerol and gels were run at constant 80 V for 3 h at r.t., stained with GelGreen Nucleic Acid Stain (supplemented with 0.1 M NaCl, according to manufacturer's instructions) for 30 min and visualized with a UV transilluminator (Bio-Rad ChemiDoc XRS). Each experiment was performed at least in triplicate.

3.3.6 Fluorescence spectroscopy experiments

Fluorescence spectra were recorded at 25 °C on HORIBA JobinYvon Inc. FluoroMax®-4 spectrofluorometer equipped with F-3004 Peltier using a quartz cuvette with a 1 cm path length (Hellma). For the fluorescence titration experiments, the excitation wavelength was set at 504 nm. Spectra were recorded in the 515-750 nm range, with entrance and exit slit set at 3 nm. Titrations were carried out using independent solutions at a fixed concentration (2 μM) of the ligand in HEPES/Na^+ buffer. Increasing amounts of V7t1 or 3R02 up to 4 μM were used from concentrated DNA solutions in HEPES/Na^+ buffer. ThT displacement assay was performed by adding to preformed N.A. V7t1 or 3R02-ThT complexes in a 2:1 aptamer-probe ratio (4 μM of aptamer and 2 μM of ThT) increasing amounts of CyOH up to 2 eq with respect to the aptamer (8 μM conc.). The excitation wavelength was set at 450 nm and spectra were recorded in the 455-650 nm range, with entrance and exit slit set at 3 nm.

3.3.7 Determination of fluorescence quantum yield of V7t1-CyOH complexes in HEPES/Na^+

In order to determine the fluorescence quantum yield of CyOH alone and in the presence of the dimeric or monomeric V7t1 aptamer (N.A. or A. V7t1 in HEPES/Na^+), a solution of fluorescein dissolved in 0.1 M NaOH solution was used as the reference standard, having absorbance and emission in similar regions as the tested samples. A series of solutions at different concentrations were prepared for the standard, for CyOH alone and for the V7t1-CyOH complexes (2:1 ratio) with maximum values of absorbance in the range from 0.01 to 0.1, in order to minimize re-absorption effects in the 1 cm fluorescence

cuvette (234). All measurements were performed at 20 °C. Standard 1 cm quartz cells were used for the absorbance and fluorescence measurements. Width of both excitation and emission slit was set at 2 nm. The excitation wavelength used for obtaining fluorescence spectra was 470 nm. Absorption spectra were recorded on a Jasco V-750 spectrophotometer. Fluorescence spectra were recorded on HORIBA JobinYvon Inc. FluoroMax®-4 spectrofluorimeter equipped with F-3004 Peltier.

The quantum yield of the V7t1-CyOH complexes in HEPES/Na^+ (Φ_x) was determined according to the following equation:

$$\Phi_x = \Phi_{st}\left(\frac{m_x}{m_{st}}\right)\left(\frac{\eta_x^2}{\eta_{st}^2}\right)$$

where Φ_{st} is the quantum yield of fluorescein in a 0.1 M NaOH solution (Φ_{st} = 95%), m_x is the slope of a linear fit for the integrated fluorescence intensity of CyOH alone or V7t1-CyOH complexes *vs*. absorbance, m_{st} is the slope of a linear fit for the integrated fluorescence intensity of fluorescein *vs*. absorbance, n_x is the refractive index of HEPES (ni = 1.33), n_{st} is the refractive index of a 0.1 M NaOH solution (n_{st} = 1.33) (235, 236).

3.3.8 Circular dichroism spectroscopy experiments

CD spectra and CD-monitored melting curves were recorded in a quartz cuvette with a path length of 1 cm (3 mL internal volume, Hellma) on a Jasco J-1500 spectropolarimeter equipped with a Jasco CTU-100 circulating thermostat unit. Spectra were registered at 25 °C in the 225-700 nm range with 2 s response, 200 nm/min scanning speed, and 2.0 nm bandwidth, corrected by subtraction of the background scan with buffer and averaged over 3 scans. The experiments were performed on N.A. and A. aptamer samples in HEPES/Na^+

buffer at 2 μM concentration. CD titration experiments were obtained by adding to fixed amounts of the DNA samples (2 μM conc.) increasing amounts of the probe up to 10 eq., corresponding to a 20 μM solution. For the melting experiments, the ellipticity at 263 nm was followed in the 15-90 °C range with 1 °C/min scan rate. Each experiment was performed in duplicate.

For the SVD analysis performed on N.A. and A. V7t1 or 3R02, the CD spectra were normalized to molar circular dichroism $\Delta\varepsilon$ = (M^{-1} cm^{-1}) using the equation $\Delta\varepsilon = \theta / (32980 \times C \times l)$, where θ is the observed CD ellipticity in millidegrees, *C* is the oligonucleotide concentration in mol/L, and *l* is the optical path length of the cell in cm. The resulting spectra were then analyzed using the advanced software developed by del Villar-Guerra et al. (232).

3.3.9 Electrophoresis mobility shift assays (EMSA)

EMSA assays were performed according to reported procedures (126, 198), with minor modifications. In detail, 30 pmol of V7t1 or 3R02 were incubated with 30 pmol of CyOH and 40 pmol of $VEGF_{165}$ at 4 °C for 30 min. Glycerol was added to the samples to a final concentration of 5% before loading. Electrophoresis was carried out at 45 V for 2.5 h on 7% polyacrylamide gels in 1× TAE (Tris-Acetate-EDTA), pH 7.8 (233). Gels were visualized on a UV transilluminator (BioRad ChemiDoc XRS) first without staining and then staining for 30 min with GelGreen Nucleic Acid Stain (supplemented with 0.1 M NaCl). Each experiment was repeated at least twice.

3.3.10 Cell cultures and cytotoxicity

Human MCF-7 breast cancer cells were obtained from the American Type Culture Collection (ATCC, Manassas, VA, USA), and were cultured in

Dulbecco's modified Eagle medium (DMEM). Non-tumorigenic human breast MCF-10A cells were also obtained from ATCC (CRL-10317™) and cultured in complete Mammary Epithelial Cell Growth Medium (MEGM, Bullet Kit, Lonza, Switzerland) supplemented with 100 ng/mL Cholera toxin (*Vibrio cholerae*) as previously described (237). Cytotoxic effects of CyOH and of the V7t1 or 3R02-CyOH complexes were evaluated by the 3-(4,5-dimethylthiazol-2-yl)-2,5 diphenyltetrazolium bromide reduction inhibition assay (MTT assay) after 48 h. To this purpose, cells (3,000/well) were seeded into 96-well plates and treated with increasing concentrations of each compound (from 0 to 30 µM). Cell survival was determined by measuring the absorbance of blue formazan at 570 nm with an automatic plate reader and expressed as the percentage of viable cells with respect to control untreated cells. Three independent experiments were performed with triplicate determinations. For all the experimental points, $*P < 0.05$, $**P < 0.01$ or $***P < 0.001$ were obtained for the control *vs.* the treated samples by performing Student's t-test analysis.

3.3.11 Analysis of cell internalization of CyOH, V7t1-CyOH and 3R02-CyOH by CLSM

Analyses were performed as previously described (238). MCF-7 and MCF-10A cells were seeded on glass coverslips in 24-well plates, grown to semi-confluency, and then incubated with each sample dissolved at 5 µM concentration of each sample. After incubation, the cells were washed with PBS 1x and then fixed with 4% paraformaldehyde in PBS for 15 min at r.t. To stain nuclei and VEGF-A protein in MCF-7 and MCF-10A cells, we employed Hoechst (0.001 mg/mL) for 15 min at r.t. and α-VEGF-A antibody (1:1000) at

4 °C overnight, respectively. Then, the cells were washed twice with PBS, mounted on coverslips and then observed by using a confocal laser-scanning microscope Zeiss LSM 700 and a 63x oil objective. Hoechst (Hoechst 33342, Trihydrochloride, Trihydrate) and α-VEGF-A antibody (Anti-VEGF-A antibody, Alexa Fluor® 488, Abcam) were purchased from ThermoFisher Scientific.

3.4 Conclusions

In the first part of this thesis work, we set up a useful diagnostic tool based on V7t1 and 3R02-CyOH complexation. These complexes showed a marked and selective fluorescence light-up when the anti-VEGF aptamers folded into dimeric and multimeric G4s (predominant in not-annealed aptamer samples), as reported in gel electrophoresis and fluorescence titration experiments. Remarkably, the target protein had much higher affinity for these dimeric or multimeric species compared to the monomeric ones, as demonstrated by EMSA and, representatively for V7t1, also by chemiluminescence-based protein binding experiments. The aptamer-probe complexes were then deeply investigated using UV–vis, CD, fluorescence spectroscopy and PAGE analysis, allowing an insight into their main features, *i.e.* high stability and very sensitive fluorescence response when bound to the target protein. The fluorescence response, attributable to the π-π stacking interactions of the cyanine probe with the terminal G-quartets of the aptamer, was almost doubled in the case of the interaction with the dimeric or multimeric G4 structures with respect to the monomeric species. Most probably, in the case of monomeric antiparallel G4 aptamers, CyOH in the 1:1 DNA/probe complex is better exposed to the polar solvent than when interacting with dimeric parallel G4

aptamers, where the probe can stack more efficiently. MTT assays showed significant toxicity of the CyOH probe alone on both human MCF-7 cancer cells and MCF10-A non-cancerogenic cells. In contrast, lower and, far more importantly, selective on cancer cells was the antiproliferative activity of this probe when complexed with V7t1 and 3R02. This clearly demonstrated that the aptamer-CyOH complexes are very stable in cells without releasing the free probe in solution, which is selectively driven by the aptamer to the target VEGF protein, overexpressed in cancer cells. Indeed, time course experiments showed a good internalization of the complexes into MCF-7 cells even without addition of transfecting agents, with an optimal uptake observed between 9 and 24 h incubation. Colocalization experiments with a fluorescently labelled anti-VEGF-A antibody confirmed the effective ability of both V7t1-CyOH and 3R02-CyOH complexes to recognize the target protein, allowing its detection with high efficiency, similar to the one of the anti-VEGF antibody, by exploiting the strong fluorescence of the aptamer-bound cyanine probe. These findings provide fundamental information to develop effective and selective targeting agents for both diagnostic and theranostic applications. In fact, V7t1-CyOH and 3R02-CyOH complexes represent an interesting proof-of-concept, being a valuable alternative not only to fluorescent antibodies, but also to aptamers covalently conjugated to specific fluorescent probes, in which the presence of the linker inserted to connect the probe may affect the aptamer folding and thus the protein recognition ability.

Chapter 4 - Studies towards V7t1 dimerization through pyridine-containing ligandosides

4.1 State of art and synopsis

Inspired by the nature's strategy of incorporating metal cofactors into biomolecular structures, several research groups started to introduce metal complexes into artificial DNA nanostructures with the aim of improving the properties of DNA secondary structures directly connected to DNA assembly and folding. Metal coordination plays important roles in maintenance and stabilization of biologically relevant structures in terms of molecular recognition and catalytic activity. These non-covalent interactions, combined with the high flexibility and efficacy of synthetic chemistry, can lead to the evolution of smart molecules with additional functionalities, previously found exclusively in biological systems, as versatile tools for catalysis, nanoelectronics or artificial photosynthesis (239). The concept of metal-mediated base pairing, which relies on the replacement of hydrogen-bonded base pairs with metal-based complexes (240, 241), acquired importance when, due to the limited binding capabilities of natural nucleobases to metal ions, artificial nucleobases decorated with various metal-binding functionalities (also named "ligandosides") were developed, resulting in a plethora of different metal-mediated base pairs containing different metal ions such as Hg^{2+}, Ag^{+}, Cu^{2+}, Cu^{+}, Zn^{2+} (242, 243). This concept was applied on different DNA secondary structures, *i.e.* DNA duplex and triplex, and more recently also to G4s (244, 245). Focusing on G4s, Gabelica, Mergny *et al.* crosslinked two thymidines in adjacent lateral loops in unimolecular G4s using the T-Hg^{2+}-T base pair, resulting in a marked structural stabilization and reduced conformational polymorphism (246). Sugimoto and coworkers incorporated into the loop of a bimolecular parallel G4 a 2,2'-bipyridine group obtaining, by adding Ni^{2+} ions, the assembly of a very stable G-wire structure with all-

parallel strand orientations due to Ni^{2+}-bipyridine complex formation (247). Clever et al. (248) used a different approach to obtain oligonucleotides self-assembling into a peculiar, well-defined 3D shape induced by metal complexation. Taking inspiration from metal-mediated base pairing, they designed a new pyridine-containing phosphoramidite scaffold (Figure 42) which could be incorporated at any position of oligonucleotide sequences (5' and/or 3'-end, or internal). In detail, four natural nucleotides within the G4 forming htel22 sequence (5'AGGGTTAGGGTTAGGGTTAGGG3') were replaced with this pyridine-containing scaffold, thus obtaining modified oligonucleotides which could still fold into G4s and selectively bind various transition metal cations. In this way, G4 folding topology changes could be triggered (249) and a switchable peroxidase mimic was realized (250). The thus modified G4 forming htel22 showed specific metal-based properties such as catalytic activity (251) and electron paramagnetic resonance (EPR) labeling character (252). On the basis of the precious features of the pyridine-containing phosphoramidites, during my period abroad in Prof. Guido Clever's group at TU Dortmund, Germany, we planned to insert this ligandoside into the sequence of anticancer aptamers aiming at improving their target recognition, thanks to the additional interactions of the donor groups, inducing the aptamer dimerization and selectively delivering transition metals (highly toxic in cells) to cancer cells. Indeed, the cytotoxicity of transition metal-complexes is well documented in the literature (253–257). This means that the design of a specific aptamer delivering them only to tumour cells and not to healthy ones would result into a very promising strategy for a therapeutic approach in cancer treatment.

To this purpose, we inserted, through solid phase synthesis, the mentioned pyridine-containing ligandoside in different positions at the 5' and 3'-end of the previously described V7t1 aptamer, obtaining the 5 different oligonucleotides reported in Table 1. In detail, two ligandosides per sequence were introduced with the aim of favouring the aptamer dimerization after the coordination with transition metals (two pyridines per sequence in a dimeric species allow coordinating a bivalent metal cation), according to the model proposed in Figure 43. Indeed, as we reported in the previous chapter, V7t1 dimerization is crucial for VEGF target recognition and toxicity to cancer cells (126, 210).

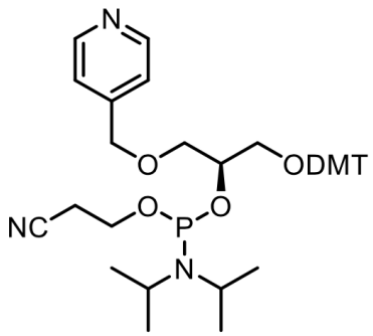

Figure 42: Phosphoramidite building block required to incorporate the artificial pyridine-containing ligandoside into the V7t1 sequence.

Table 1: Sequences of the V7t1 modified oligonucleotides. X= pyridine-containing ligandoside.

Name	**Sequence**
V7t1	$^{5'}$TGTGGGGGTGGACGGGCCGGGTAGA$^{3'}$ 25-mer
Modified V7t1 n1	$^{5'}$XXTGTGGGGGTGGACGGGCCGGGTAGA$^{3'}$ 27-mer
Modified V7t1 n2	$^{5'}$XTXTGTGGGGGTGGACGGGCCGGGTAGA$^{3'}$ 28-mer
Modified V7t1 n3	$^{5'}$TGTGGGGGTGGACGGGCCGGGTAGAXXT$^{3'}$ 28-mer
Modified V7t1 n4	$^{5'}$TGTGGGGGTGGACGGGCCGGGTAGAXTXT$^{3'}$ 29-mer
Modified V7t1 n5	$^{5'}$TGTGGGGGTGGACGGGCCGGGTAGAXTTXT$^{3'}$ 30-mer

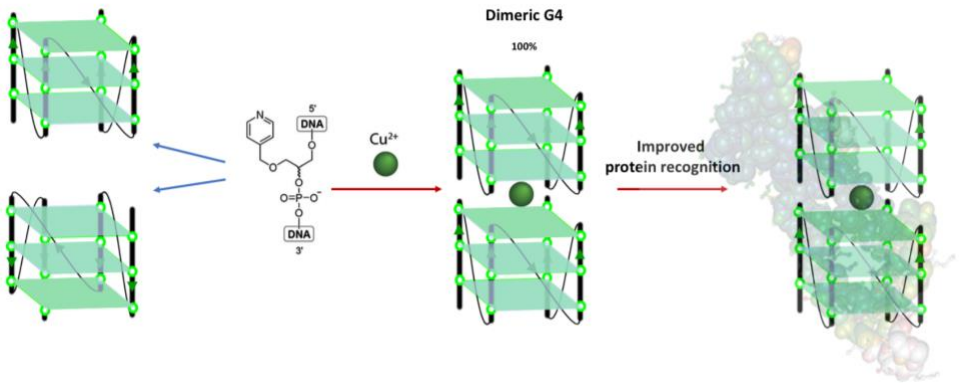

Figure 43: Schematic representation of the strategy here adopted to obtain metal-mediated dimerization of V7t1.

4.2 Results and discussion

4.2.1 Analysis of the V7t1 analogues by CD spectroscopy

To verify possible main conformational changes correlated to the inserted pyridine-containing modifications, a CD analysis was performed on the synthesized N.A. V7t1 analogues in HEPES/Na^+. All the investigated aptamers showed CD profiles indicative of mostly parallel G4 structures, with a main band at 263 nm, similar to the wild-type sequence, with the exception of modified V7t1 n4, which showed the band at 295 nm more intense that the one at 263 nm, attributable to a high content of antiparallel G4 structures. By adding 1 eq of $CuSO_4$ to a fixed concentration (4 μM) of the selected aptamers, slight-to-null variations of the CD profiles were observed, indicating no detectable change of the overall G4 folding of the aptamers (Figure 44).

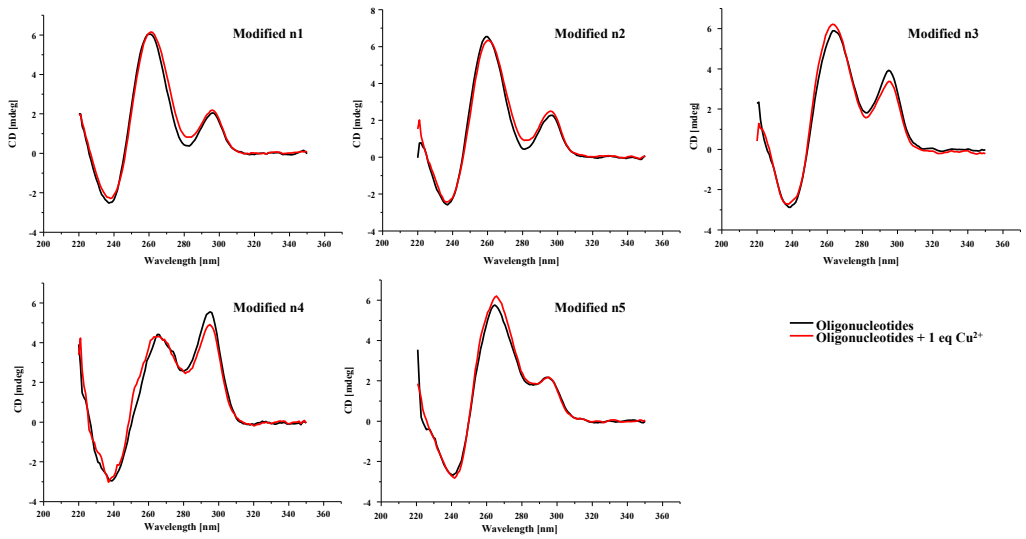

Figure 44: CD spectra of the V7t1 modified oligonucleotides alone (black line) and in the presence of 1 eq of $CuSO_4$ (red line).

4.2.2 Analysis of the V7t1 analogues by UV-vis spectroscopy

UV-melting experiments were performed to evaluate the thermal stability of the new V7t1 analogues alone and in the presence of 1 eq of $CuSO_4$ by monitoring the UV signal at 295 nm in the 20-85 °C range (Figure 45). The UV-melting profiles and the T_m values of the aptamers alone were similar to the ones of unmodified V7t1 (126). Moreover, by adding 1 eq of $CuSO_4$, no stabilizing effects were detected, except for modified n4, which showed a 2 °C stabilization.

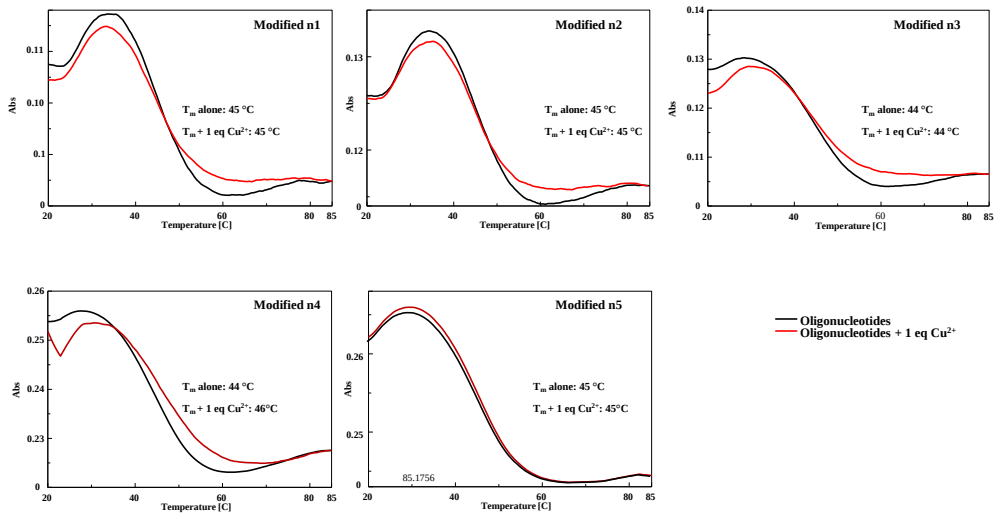

Figure 45: UV-melting spectra of the V7t1 analogues alone (black line) and in the presence of 1 eq of $CuSO_4$ (red line).

4.2.3 Analysis of the V7t1 analogues by native PAGE

In order to characterize the N.A. synthesized aptamers in terms of number and molecularity of the species present in solution, a native gel electrophoresis analysis was performed. Analogously to unmodified V7t1, the samples showed a band with high mobility, referred to monomeric G4 species, and a retarded one, attributable to dimeric G4 species (Figure 46 left). The difference observed in the gel mobility among the various bands was a consequence of the different length of the investigated sequences. Indeed, by increasing the length of the sequences, the bands on the gel migrated to a lesser extent. The same experiment was performed in the presence of 10 eq of $CuSO_4$, but no substantial differences were observed both in the migration and intensity of the bands (Figure 46, right).

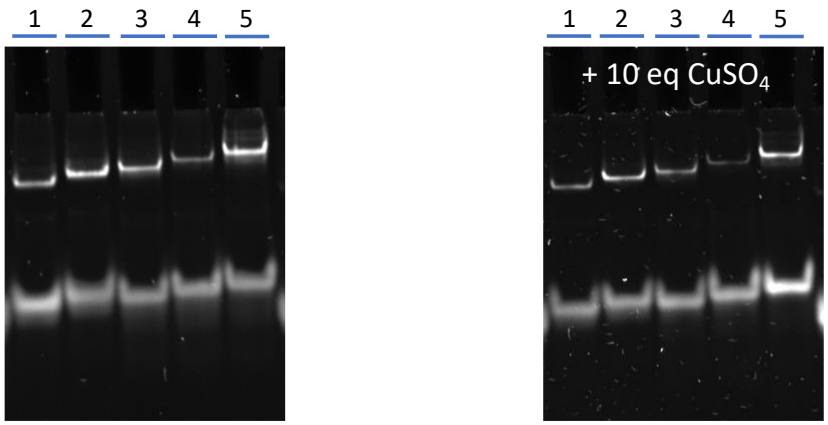

Figure 46: Representative 20% polyacrylamide gel electrophoresis analysis under native conditions of 3 μM V7t1 analogues in HEPES/Na^+ buffer alone (on the left) and in the presence of 10 eq of $CuSO_4$ (on the right). The gels were run at constant 80 V for 3 h at r.t. with TB 1x as running buffer. Modified n1, n2, n3, n4, n5 were loaded in lanes 1, 2, 3, 4, 5, respectively.

4.3 Experimental section

4.3.1 Solid phase oligonucleotide synthesis of the V7t1 analogues

All oligonucleotides were synthesized on a K&A Laborgeraete GbR H-8 synthesizer on a 1 μmol scale using the standard phosphoramidite method with Controlled Pore Glass (CPG) and 4,4'-Dimethoxytrityl (DMT), β-cyanoethyl (CE)-protected DNA phosphoramidites (DMT-dT-CEP, DMT-dG(iBu)-CEP, DMT-dA(bz)-CEP, DMT-dC(bz)-CEP). 5-(Benzylthio)-1*H*-tetrazole solution (BTT) was used as the activator. Cartridges with CPG solid supports (1000 Å, 25-35 μmol/g, DMT-dT-CPG, DMT- dA(bz)-CPG) were manually packed. Reagent solutions (Table 2) were purchased from Sigma Aldrich, with the exception of the oxidizing solution (OXI), which was prepared in house. As first step, the cartridges were treated three times with DCA to deprotect the 5'-OH groups. Then, coupling was achieved by mixing the respective phosphoramidite building block (0.1 M in acetonitrile) with BTT (1:1, v/v), with a coupling time of 0.5 min for standard phosphoramidites and 3.5 min for modified phosphoramidites. After that, the acetylation step of the unreacted 5'-OH groups was performed by treatment with a 1:1 (v/v) mixture of Cap A and Cap B, followed by oxidation with OXI. After each individual step of the cycle, the cartridge was exhaustively washed with acetonitrile followed by a drying step with anhydrous nitrogen. The described cycle was repeated for each incorporated nucleotide.

Table 2: Reagents for DNA synthesis.

Name	Reagent	Composition
DCA	Detritylation	3% (v/v) dichloroacetic acid in anhydrous dichloromethane
BTT	Activator	0.3 M 5-(benzylthio)-1H-tetrazole in anhydrous acetonitrile
Cap A	Capping A	10% (v/v) N-methyl imidazole in anhydrous tetrahydrofuran
Cap B	Capping B	2,6-lutidine / acetic anhydride / anhydrous tetrahydrofuran 1:1:8 (v/v/v)
OXI	Oxidizer	0.02 M iodine in tetrahydrofuran / pyridine / water 7:2:1 (v/v/v)

Cleavage of the DNA sequences from the solid support and removal of all protecting groups (except for the DMT group) were carried out treating them with concentrated aqueous NH_3 solution (0.5 mL) at 55 °C overnight. The supernatant was then filtered using VWR centrifugal filters and, after a washing of the solid support with 100 μL H_2O, NH_3 was evaporated under reduced pressure using a vacuum concentrator (H. Saur Laborbedarf S-Concentrator BA-VC-300H).

4.3.2 Purification of the V7t1 analogues

All the synthesized DMT-protected oligonucleotides were purified using semipreparative reversed-phase HPLC on an Agilent Technologies 1260 Infinity II HPLC system equipped with an autosampler, column oven, diode array detector (DAD) detector and a Macherey-Nagel VP 250/10 NUCLEODUR 100-5 C18ec column. The oven temperature was 60 °C and the flow rate 2.5 mL/min. The gradient was from 100% solvent A to 20% solvent A-80% solvent B in 30 min, where solvent A: 50 mM TEAA pH 7.0 and solvent B: 70:30 acetonitrile/50 mM TEAA pH 7.0. The samples were then

lyophilized using a Christ Alpha 2-4 LSC basic lyophilization device and dissolved with 2 mL 100 mM TEAA pH 7.0.

As last steps, the 5′-OH DMT protecting groups were removed by treatment with 2% trifluoroacetic acid and the oligonucleotide samples were then purified using Waters Sep-Pak C18 cartridges eluted with H_2O:acetonitrile 1:1. The final, pure oligonucleotides were lyophilized and redissolved in pure water.

4.3.3 Concentration determination of oligonucleotides

The concentrations of all the oligonucleotide stock solutions in water were determined by measuring their absorbance at 260 nm at 25 °C with a Thermo Scientific Nanodrop One instrument and using revised extinction coefficients for the canonical nucleosides (258) and for the artificial nucleoside (ε260 = 1971 L mol^{-1} cm^{-1}) (249).

4.3.4 CD spectroscopy analysis

CD spectra were recorded in a quartz cuvette with a path length of 1 cm (1 mL internal volume, Hellma) on an Applied Photophysics Chirascan qCD spectropolarimeter equipped with a Quantum Northwest temperature control unit. Spectra were registered at 25 °C in the 200-350 nm range with 0.5 s time-per-point, step size 1 nm and 0.5 nm bandwidth, corrected by subtraction of the background scan with buffer and averaged over 3 scans.

4.3.5 UV-vis spectroscopy analysis

UV-melting curves were recorded on a Jasco V-650 UV-visible spectrophotometer equipped with a PAC-743 6-cell thermostat using 1 cm path length cuvettes (1 mL internal volume, Hellma). The absorption of the samples at 295 nm was followed in the 20-85 °C range in a 0.5 °C interval with a temperature gradient set to 0.5 °C/min. The T_m values were calculated as the minima of the first derivative plots of the melting curves.

4.3.6 PAGE analysis

All the samples (3 μM) in HEPES/Na^+ buffer were loaded on 20% polyacrylamide gels with TB 1x (Tris-borate) as running buffer. $CuSO_4$ was added in excess with respect to the DNA (10 eq) and incubated with the aptamers overnight at r.t. before running the gel. In these experiments EDTA was removed from the running buffer to avoid its chelation of Cu^{2+} ions. Just before loading, samples were supplemented with 5% glycerol and gels were run at constant 80 V for 3 h at r.t., stained with GelGreen Nucleic Acid Stain for 30 min and visualized with a UV transilluminator (Bio-Rad ChemiDoc XRS).

4.4 Conclusions

During my 6-month research period abroad in Prof. Clever's group at TU Dortmund, Germany, I designed and synthesized a mini-library of V7t1 analogues aiming at obtaining improved VEGF target recognition and anticancer activity. A pyridine-containing ligandoside was installed in different positions of the previously described aptamer V7t1, obtaining 5

modified oligonucleotides that were characterized by preliminary biophysical experiments, *i.e.* CD, UV-vis and gel electrophoresis under native conditions, in the absence and presence of Cu^{2+} ions. The V7t1 analogues showed a behaviour similar to the unmodified sequence, with a mainly parallel G4 conformation (except for modified n4), similar melting temperatures and ability to form monomeric and dimeric species. So far, no relevant changes in terms of G4 folding, melting temperature or molecularity were observed in the presence of Cu^{2+}, suggesting that no complexation occurred. Further studies will be performed trying different complexation conditions, using other promising transition metals like Pt^{2+}, Cd^{2+}, Ni^{2+}, and synthesizing other V7t1 analogues, with the pyridine containing ligandoside also in different positions of V7t1 sequence. The aptamers will be then evaluated in their interaction with the target protein through EMSA or chemiluminescence ELISA-like assays using the protocols described in the previous chapter.

Chapter 5 - G-quadruplex forming aptamers for selective HMGB1 inhibition

5.1 State of art and synopsis

In the second part of my thesis work I focused on the search of novel G4 forming aptamers for selective HMGB1 inhibition. As already mentioned in Chapter 1.7, extracellular HMGB1 contributes to the pathogenesis of multiple diseases like sepsis, atherosclerosis, rheumatoid arthritis and Alzheimer (168, 170, 259). In particular, high expression of HMGB1 was observed in certain primary tumours including melanoma (260), hepatoma (261), mesothelioma (262) colorectal (263), breast (264) and pancreatic (265) cancers. Considering the crucial role of HMGB1 in a plethora of pathologies, the identification of HMGB1 inhibitors is of huge clinical interest, representing a promising approach to modulate the inflammatory activity of the protein, as well as to block tumour growth and metastasis (134, 175).

In this context, we here focused on the design and identification of proper novel G4 forming aptamers for selective HMGB1 inhibition. To this purpose, we took into account several important issues, *i.e.*: i) the ability of HMGB1 to recognize non-canonical (*i.e.* non-B) DNA structures, *e.g.* cruciform, cis-platinated, hemicatenated DNAs (141–143); ii) the good results of bent DNA duplexes as HMGB1-inhibitors, showing interesting results in terms of HMGB1 binding and inhibition of some cellular processes induced by the protein (134, 187); iii) the ability of HMGB1 to bind G4 forming oligonucleotides, being fished out by a 26-mer truncation of the human telomeric sequence (tel_{26}) from a human cellular nuclear extract (192, 266) and recognizing with high affinity a G4 tract in the promoter region of *KRAS* oncogene (193). In detail, we designed a partially randomized library of G-rich oligonucleotides using tel_{26} as the model G4 forming sequence. Successively, using SELEX technology, 14 aptamer sequences were selected as the best

HMGB1 binders. We investigated the conformational behavior of the selected aptamers in a Na^+-rich buffer − *i.e.* PBS (Phosphate-Buffered Saline), mimicking the extracellular environment where HMGB1 performs its pathological cytokine activity (149, 150) – using biophysical techniques. Then we evaluated their enzymatic stability in serum via gel electrophoretic experiments to determine their effective potential for *in vitro* and *in vivo* applications. Binding studies were performed in order to estimate their affinity to HMGB1. Finally, the ability of these aptamers to inhibit HMGB1-induced cellular migration, which is generally enhanced in the presence of inflammatory processes and cancer metastasis, was tested to evaluate their *in vitro* bioactivity.

5.2 Results and discussion

5.2.1 Selection of oligonucleotide aptamers as HMGB1 ligands from a library of G-rich sequences

In order to identify aptamers specifically recognizing the HMGB1 protein, a partially randomized DNA library of 57-mer oligonucleotides was initially designed. This oligonucleotide pool contained a G-rich core derived from the 26-mer DNA sequence [5'TTA(GGGTTA)$_3$GGGTT3'] of the human telomere (tel_{26}). Specifically, the library core is characterized by four GGG tracts, alternated with tracts of three variable bases (with restriction to thymine and adenine) repeated 3 times. In analogy to the well-studied sequence tel_{26}, the three TTA and the two TT bases at the 5' and 3' ends respectively, were maintained (5'TTA(GGGXXX)$_3$GGGTT3'). Further extensions were inserted at both the 5' and 3' ends to allow the amplification of the selected sequences

by PCR using suitable primers. Magnetic agarose beads functionalized through a suitable linker with the Ni-NTA (nitrilotriacetic acid) complex were used for the partitioning step of the SELEX cycle. The nickel ion on the surface of the beads, coordinated with NTA, has a square-based bipyramid coordination geometry, with two sites occupied by water molecules which are efficiently replaced by nitrogen-containing ligands, such as histidine residues. By exploiting this principle, proteins with 6 histidine tails (His-tag proteins) are easily and strongly immobilized on these particles. Before carrying out SELEX with the target of our interest, *i.e.* the HMGB1 protein, a counter-SELEX cycle was performed to reduce non-specific interactions with another protein competing with the selected protein. For the counter-selection, His–tag functionalized VEGF-A (Vascular Endothelial Growth Factor) was used (Figure 47). This protein was chosen based on the fact that high serum levels of VEGF-A are detected, in analogy to HMGB1, in various cancer cell types due to its involvement in angiogenesis of a large number of solid tumours (196). The library sequences were first heated at 85 °C for 5 min, then immediately cooled on ice for 2 min, allowed warming up to r. t. and then incubated with VEGF-A for 30 min. This thermal treatment favoured the formation of intramolecular rather than intermolecular oligonucleotide structures. The Ni-coated magnetic beads were then added, and a magnetic separation was performed by recovering the supernatant and discarding the beads containing the non-specific VEGF-bound sequences. Then, a positive SELEX cycle was carried out using the HMGB1 target protein (Figure 47). After incubation of the supernatant of the previous step with the protein, magnetic separation allowed recovering the HMGB1-bound sequences removing the unbound ones. The bound sequences were extracted, amplified by PCR (10 cycles), quantified, cloned and identified by sequencing. In this

way, 14 oligonucleotide sequences were obtained for the development of potential anti-HMGB1 aptamers. The final sequences, deprived of the primers and keeping the G4 core and the flanking bases as in the tel_{26} 26-mer, are the following:

A32	**5'TTAGGGTTAGGGAATGGGATAGGGTT3'**
B6	**5'TTAGGGATAGGGTTTGGGATAGGGTT3'**
D40	**5'TTAGGGTATGGGTATGGGATTGGGTT3'**
L12	**5'TTAGGGATTGGGAATGGGTATGGGTT3'**
L13	**5'TTAGGGTATGGGAAAGGGTAAGGGTT3'**
L16	**5'TTAGGGAAAGGGTTAGGGAAAGGGTT3'**
L17	**5'TTAGGGTATGGGATAGGGTATGGGTT3'**
L21	**5'TTAGGGTTAGGGTAAGGGATAGGGTT3'**
L23	**5'TTAGGGATTGGGATTGGGATTGGGTT3'**
L27	**5'TTAGGGTAAGGGAAAGGGTTTGGGTT3'**
L30	**5'TTAGGGTATGGGTTTGGGATAGGGTT3'**
L33	**5'TTAGGGTTAGGGTAAGGGATTGGGTT3'**
L37	**5'TTAGGGATAGGGATTGGGTTAGGGTT3'**
L41	**5'TTAGGGAAAGGGTATGGGAAAGGGTT3'**

It is interesting to note that in our conditions the sequence corresponding to tel_{26} was not present among the 14 selected ones. This was probably due to its interaction during the counter-selection process with VEGF or with the beads, or to its lower affinity for HMGB1 with respect to the selected sequences under the experimental conditions explored.

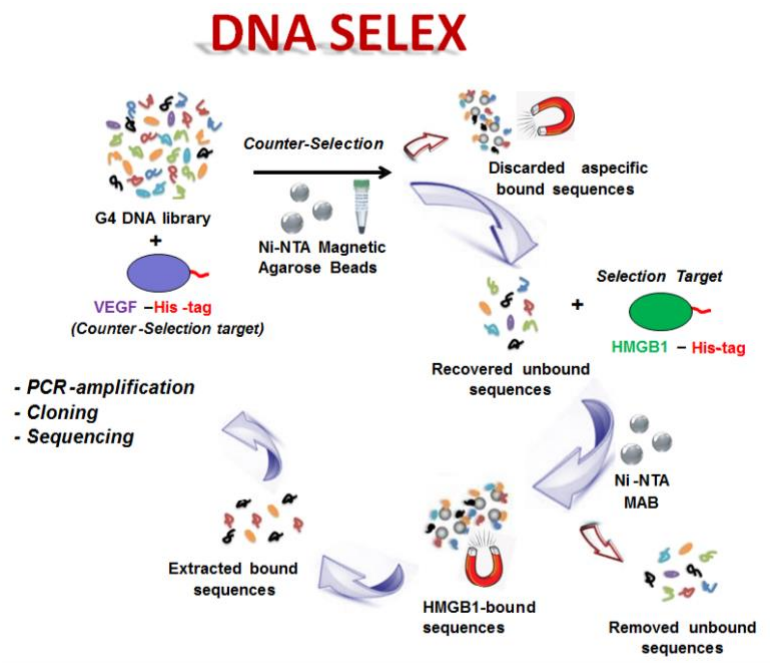

Figure 47. Schematic representation of the SELEX protocol applied for the selection of anti-HMGB1 aptamers.

5.2.2 Conformational analysis of the selected aptamers and evaluation of their thermal stability by spectroscopic experiments: studies on the annealed oligonucleotides

The 14 oligonucleotide sequences identified by SELEX along with the model oligonucleotide tel_{26}, after dilution in the proper buffer, were first studied by subjecting them to a slow annealing procedure, in order to obtain their thermodynamically favoured structures. To this purpose, each oligonucleotide solution was heated at 95 °C for 5 min and then left to slowly cool to room temperature overnight. Then a detailed analysis of the biophysical properties of the "annealed" (A) sequences was performed in order to explore their tendency to form G4 structures, investigating their molecularity and

preferential G4 conformation. In addition, the thermal and enzymatic stabilities of the A. sequences were also analyzed. Almost all the sequences gave CD spectra typical of G4 structures, even though each sample appeared generally as a mixture of two or more G4 conformations with an overall prevalence of the antiparallel and hybrid ones (Figure 48a,b). CD-monitored thermal denaturation studies on the G4 structures formed by these anti-HMGB1 oligonucleotides revealed that more than half of the studied sequences showed G4 structures featured by T_m values lower than, or close to 37 °C in PBS.

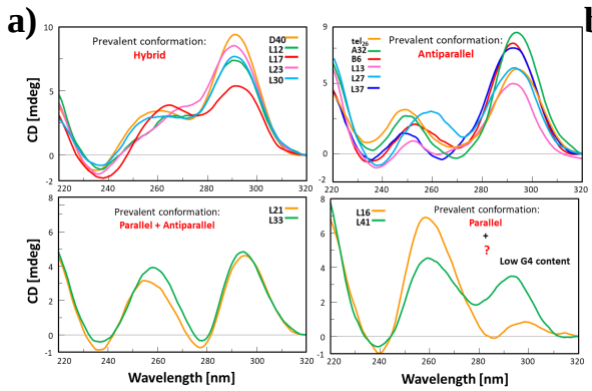

b)

SVD analysis

Aptamers	Parallel	Hybrid	Antiparallel
tel_{26}	20	20	61
A32	8	36	57
B6	12	39	50
D40	10	58	33
L12	12	53	35
L13	18	26	55
L17	26	35	38
L21	36	0	65
L23	6	67	28
L27	24	23	51
L30	15	48	37
L33	38	1	62
L37	5	46	50

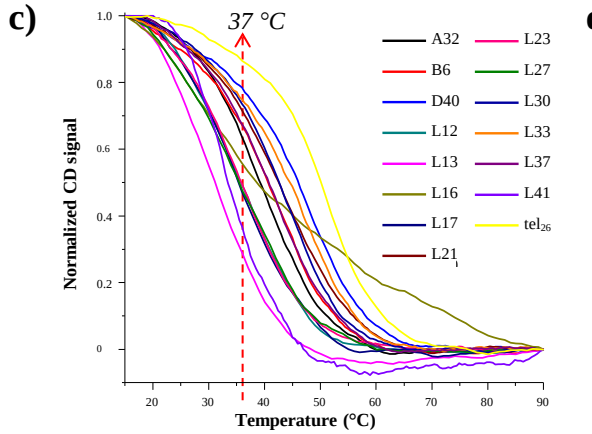

d)

Aptamers	Melting T_m in PBS (°C)
tel_{26}	51
A32	39
B6	43
D40	48
L12	36
L13	30
L16	30
L17	35
L21	44
L23	36
L27	36
L30	44
L33	47
L37	42
L41	32

Figure 48. Conformational characterization and thermal stability of the selected anti-HMGB1 aptamers annealed in PBS.

Therefore, these oligonucleotides – with the only exception of D40, having a T_m value of 48 °C – proved to be partially unfolded under physiological conditions (Figure 48c,d). The same aptamer sequences were thus investigated in physiological conditions, avoiding any thermal treatment of the samples after dilution from their stock solution ("not annealed", NA, samples), in order to potentially favour their kinetically preferred conformations.

5.2.3 UV-vis spectroscopic analysis

UV spectra of each N.A. aptamer sequence were recorded at 2 μM concentration in PBS at low and high temperatures (*i.e.* first at 10 and then at 95 °C; Figure 49a). The difference between the UV spectra of each completely unfolded (at 95 °C) and folded (at 10 °C) oligonucleotide allows obtaining the thermal difference spectrum (TDS, Figure 49b) for each sequence which can be considered as a "fingerprint" of a specific nucleic acid secondary structure and, in particular, allows identifying the presence in solution of a G4 structure (225, 267–269). In PBS, all the investigated sequences exhibited normalized TDS profiles featuring three positive (at ca. 240, 260 and 275 nm) and two negative bands (at around 230 and 295 nm), which are similar to those of tel_{26} (Figure 49b, light blue line), here used as a model compound, and are diagnostic of G4 structures (225, 267, 269).

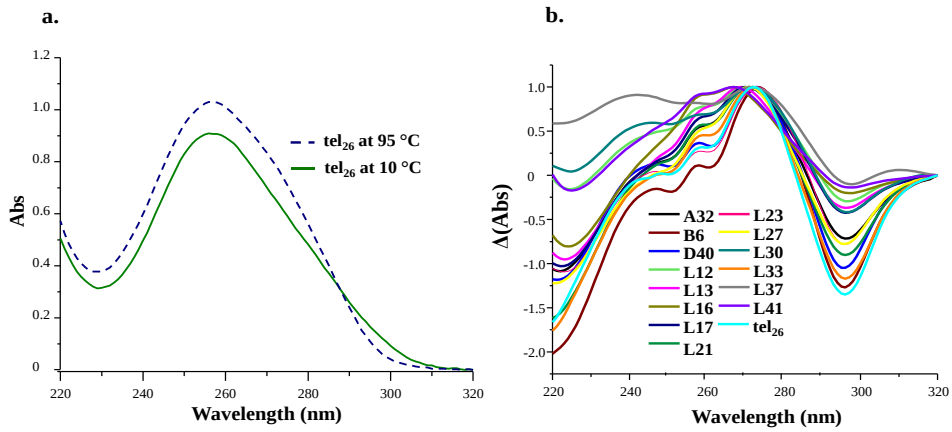

Figure 49. a) Overlapped UV spectra of N.A. tel_{26} (2 µM in PBS) at 10 (solid green line) and 95 °C (dashed blue line). **b**) Normalized TDS profiles of the N.A. aptamers investigated at 2 µM in PBS, in comparison with tel_{26} (light blue line). TDS profiles resulted from the subtraction of each UV spectrum registered at 10 °C from the corresponding one recorded at 95 °C.

5.2.4 CD spectra and CD-monitored thermal denaturation analysis

In order to deeply investigate the conformational properties of the examined G4-forming oligonucleotides as N.A. samples, CD spectra of the oligonucleotide sequences – at 20 °C in PBS, at 2 µM oligonucleotide concentration – were recorded in comparison with tel_{26}. The reference sequence tel_{26} adopted, under these conditions, mainly an antiparallel G4 conformation, in agreement with literature reports (270), showing a quite intense positive CD signal centered at around 295 nm and a weaker maximum at 250 nm (Figure 50).

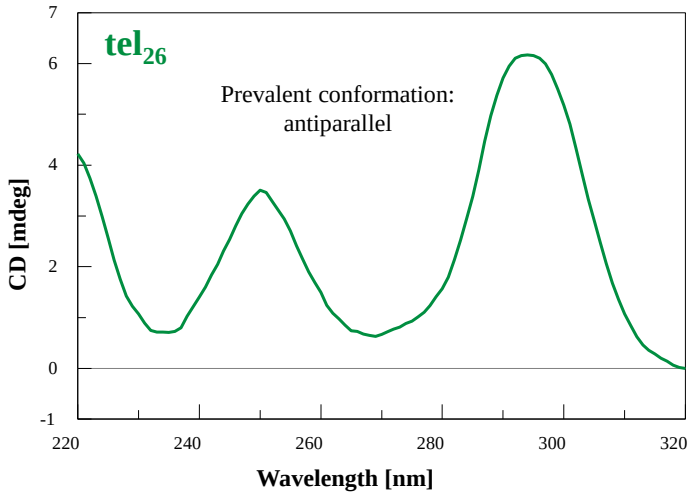

Figure 50. Representative CD spectrum for N.A. tel_{26} recorded at 20 °C in PBS at 2 µM concentration.

The CD spectra, consistently with the TDS data, confirmed the G4 folding, but with coexistence of different G4 topologies for all the studied aptamers. The observed CD profiles were classified into four different groups (Figure 51). A32, L21 and L33 showed CD spectra consistent with a mixture of parallel and antiparallel G4 structures, with maxima around 295 and 260 nm; B6, D40 and L37 formed predominantly hybrid and antiparallel G4 structures, with a main positive intense signal at 295 nm and a weaker one at around 260 nm; L23, L27 and L30 formed a mixture of G4 topologies, with no prevalence of one specific conformation; L12, L13, L16, L17 and L41 showed CD spectra typical of mainly parallel G4 structures. In order to get a deeper and quantitative insight into the G4 topologies adopted by the aptamers in solution, their CD spectra were also processed by singular value decomposition (SVD) analysis (232). The use of the software developed by del Villar-Guerra *et al.* allowed determining the percentage of each conformation that contributes to the overall

CD spectrum of each system (Table 3). The aptamers showed a marked G4-polymorphism, in no case evidencing a unique preferential conformation.

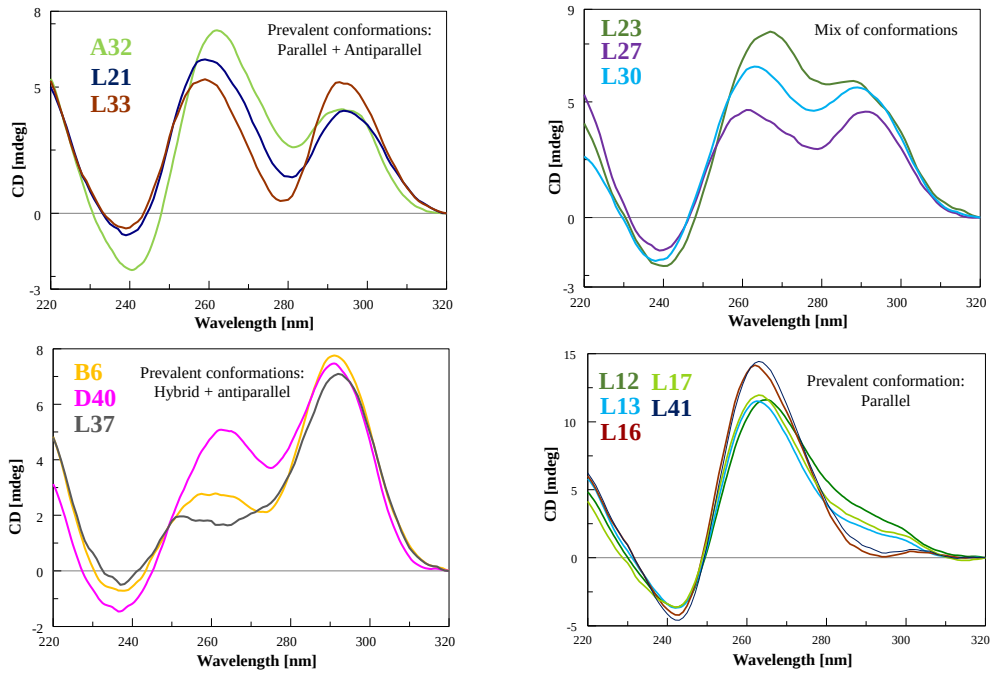

Figure 51. Representative CD spectra of all the N.A. anti-HMGB1 aptamers grouped by conformational similarity. CD spectra were recorded at 20 °C in PBS at 2 µM oligonucleotide concentration.

Table 3. Prediction of the relative abundance of the G-quadruplex topologies adopted by the here investigated anti-HMGB1 aptamers, as obtained by singular value decomposition (SVD) analysis of the CD spectra. Deviations from 100% (± 1%) are due to significant digit approximation of the values originally obtained by simulations.

Aptamers	*Parallel %*	*Hybrid %*	*Antiparallel %*
tel_{26}	**21**	**19**	**61**
A32	**44**	**22**	**34**
B6	**14**	**47**	**40**
D40	**22**	**49**	**30**
L12	**51**	**43**	**5**
L13	**61**	**22**	**16**
L16	**78**	**8**	**13**
L17	**62**	**24**	**14**
L21	**46**	**7**	**48**
L23	**31**	**55**	**15**
L27	**33**	**27**	**40**
L30	**33**	**41**	**27**
L33	**40**	**7**	**54**
L37	**13**	**44**	**44**
L41	**74**	**17**	**8**

Thermal stability of the G4 structures formed by the anti-HMGB1 sequences was studied by CD-melting experiments, obtained by monitoring the CD signal at the maximum ellipticity for each oligonucleotide system on varying the temperature. For these experiments, all the oligonucleotides were analyzed at 2 μM in PBS in the 10-90 °C range, in comparison with tel_{26}. The overlapped CD-melting profiles, normalized between 0 and 1, of all the studied oligonucleotides were reported in Figure 52. For some sequences, the increase of the CD intensity on increasing the temperature is attributable to the

conversion of relatively unstable conformations to higher-stability structures that occurs in the range 10-40 °C. The T_m values were estimated as the minima of the first derivative plots of the melting curves. These data showed that almost all the aptamers, in the examined conditions, folded into G4 structures with excellent thermal stability: indeed, most of them exhibited T_m values far higher than 37 °C in PBS, *i.e.* under conditions mimicking the physiological *in vivo* conditions. By comparing the CD data obtained for the analyzed N.A. oligonucleotide sequences with those previously collected for the same A. sequences, interesting features emerged. Specifically, in many cases, a remarkable increase of the thermal stability of N.A. aptamers, in comparison with the corresponding A. ones, was evidenced, as reported in Table 4.

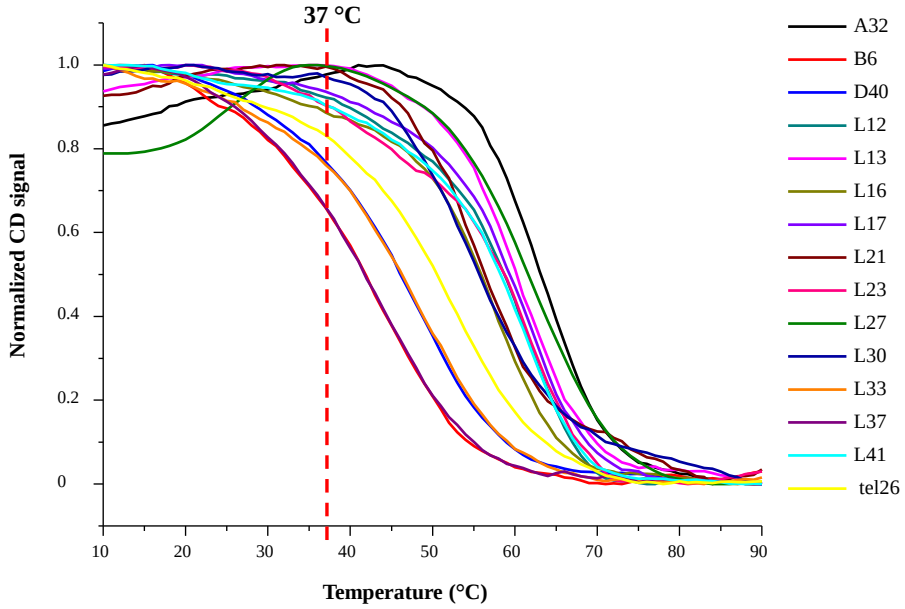

Figure 52. CD-melting profiles – at 2 μM in the 10-90 °C range using a scan rate of 1 °C/min – were recorded in PBS at the ellipticity maximum observed for each oligonucleotide system and are reported as normalized CD signal of each N.A. oligonucleotide system as a function of temperature.

Table 4. Melting temperatures of the selected aptamers and tel_{26} control sequence: comparison between their A. and N.A. forms. Green arrows evidence the species with the highest differences in T_m between the two aptamer forms.

Aptamers	T_m±1 (°C) "annealed" (λ_{max} - nm)	T_m ±1 (°C) "not annealed" (λ_{max} - nm)
tel_{26}	51 (295)	51 (295)
A32	39 (295) →	63 (262)
B6	43 (291)	44 (291)
D40	48 (292)	48 (291)
L12	36 (290) →	61 (265)
L13	30 (292) →	61 (262)
L16	n.d. →	58 (263)
L17	35 (292) →	61 (264)
L21	44 (295) →	56 (262)
L23	36 (291) →	61 (265)
L27	36 (293) →	62 (263)
L30	44 (292) →	55 (262)
L33	47 (293)	48 (295)
L37	42 (292)	43 (292)
L41	32 (292) →	61 (263)

Interestingly, large differences in T_m values between A. and N.A. aptamers were associated with significant conformational differences (Figure 53), whereas aptamers with similar conformations in both A. and N.A. conditions maintained similar T_m values.

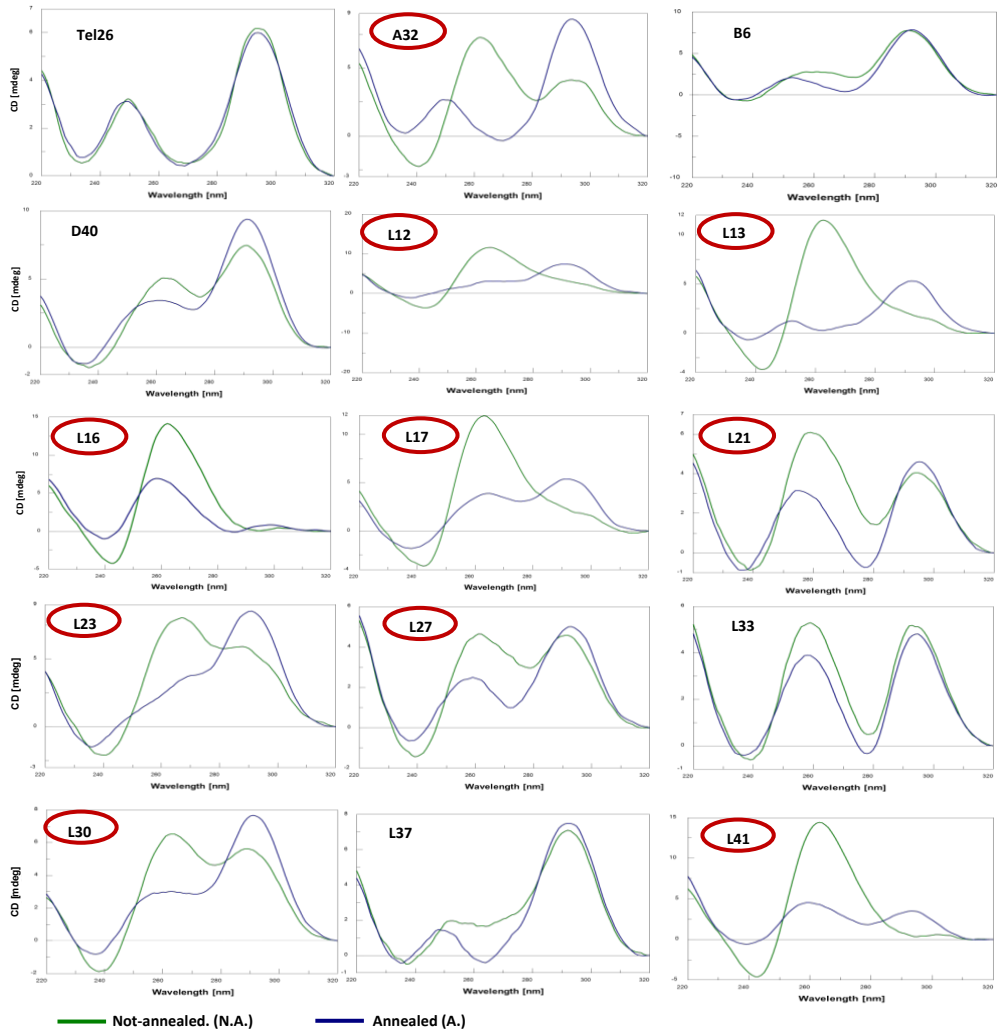

Figure 53. Superimposed CD profiles of "annealed" (A., blue line) and "not annealed" (N.A., green) aptamers and tel_{26} control. Sequences evidencing high differences in the CD spectra between the two forms are highlighted with red circles: these sequences showed high differences also in their melting temperatures (as highlighted in Table 4) with the highest values obtained for the N.A. sequences.

Intrigued by this behaviour, we further analyzed the conformational properties of the studied sequences, specifically investigating different thermal treatments. Indeed, we analyzed the CD profiles of some of the

oligonucleotides showing the highest conformational differences between A. and N.A. forms, after a “thermal shock” treatment, consisting in heating each sample at 85 °C for 5 min, then immediately cooling it on ice for 2 min, and successively warming it up to r. t.. The same treatment was indeed performed also on the initial 57-mer oligonucleotide library during the SELEX process before the incubation with the protein target. However, we observed that the CD spectra of all the samples after the “thermal shock” treatment were very similar to the ones of the slowly annealed (A.) oligonucleotides (black and red lines of Figure 54). Thus, the more stable conformations of the N.A. samples (where a general prevalence of the parallel G4 structures was evidenced) generally differed from the conformations obtained by the “thermal shock” treatment (blue lines of Figure 54).

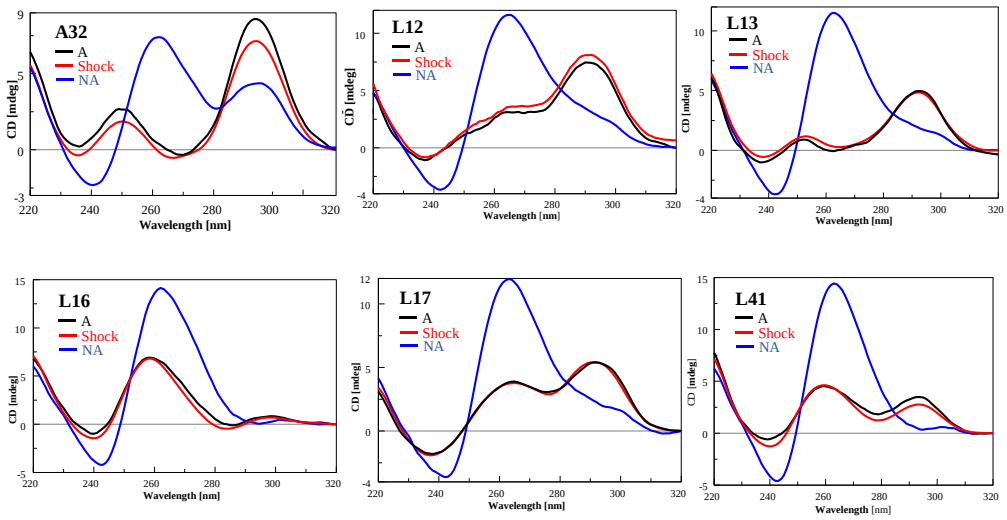

Figure 54. Superimposed CD spectra, recorded at 20°C, of representative aptamers treated according to annealing procedure (A., black line), “thermal shock” (Shock, red) and thermically untreated (N.A., blue).

Thus, we attempted to investigate the preferred conformations adopted by the aptamers in the stock concentrated solutions in water. To this purpose, starting from the initial 200 mM stock solution, we diluted the aptamers to 2 μM concentration in pure water and immediately recorded their CD spectra (Figure 55). Surprisingly, a good degree of pre-structuration in water was observed in all cases, even in the absence of high concentrations of G4-stabilizing metal cations.

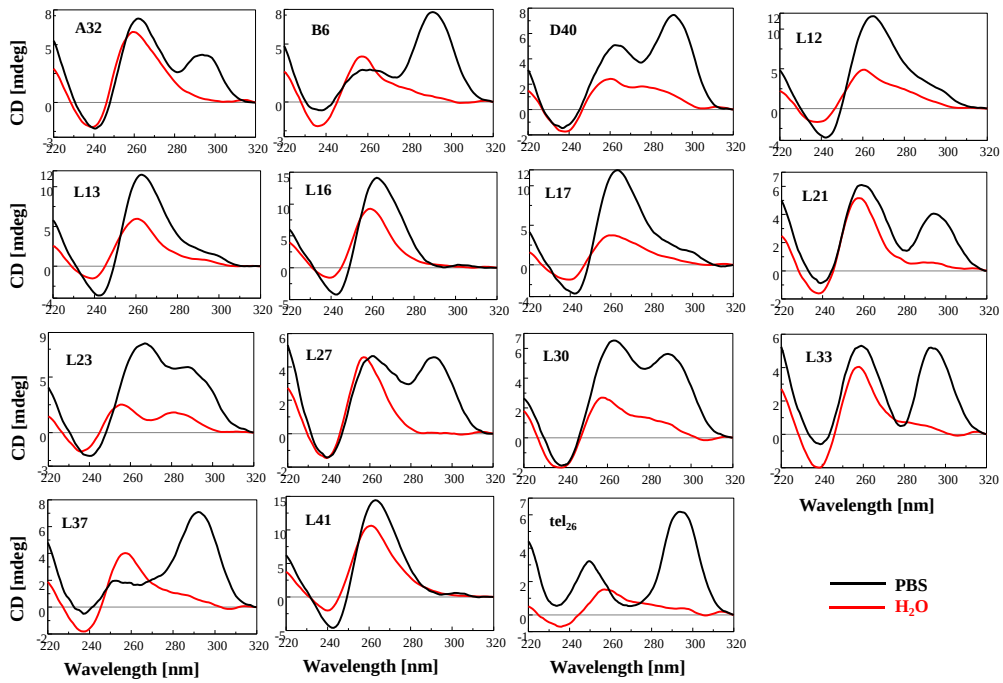

Figure 55. Superimposed CD spectra, recorded at 20°C, of 2 μM N.A. aptamer solutions in PBS (black lines) and water (red).

Furthermore, a general uniformity between the CD spectra, with overall prevalence of the parallel G4 conformation, was revealed for all the N.A. sequences in H_2O (Figure 56). We noticed that the spectra in water had almost the same profiles as those in PBS, when the contribution of the parallel

conformation in PBS was high. In contrast, they showed large differences among them when the parallel G4 conformations gave a lower contribution to the overall aptamer structure (Figure 55). Hence, we concluded that the parallel G4 structures endowed with high stability in PBS were already present in the concentrated stock solutions in water, where crowding conditions are realized, and could probably correspond to trapped structures with kinetic energy minima, which cannot be reformed once the samples are fully unfolded by thermal treatment (in the case of kinetic minima not coincident with thermodynamic ones).

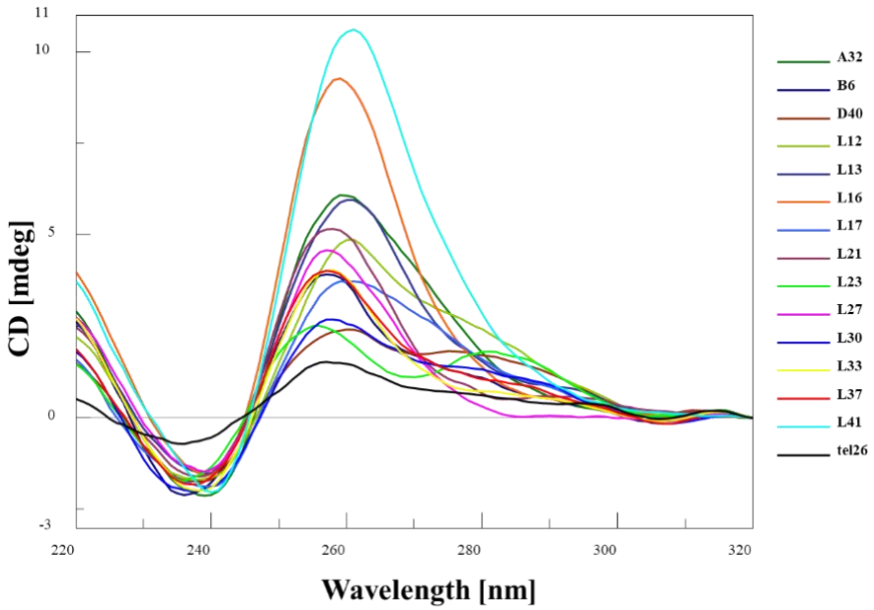

Figure 56. Superimposed CD spectra, recorded at 20°C, of 2 µM N.A. aptamer solutions in water.

In addition, we compared the CD spectra of the N.A. sequences in PBS recorded at 20 and 37 °C, to search for possible conformational switches in this temperature range. No evident conformational switch was observed in the 20 - 37 °C range in almost all the explored systems (Figure 57).

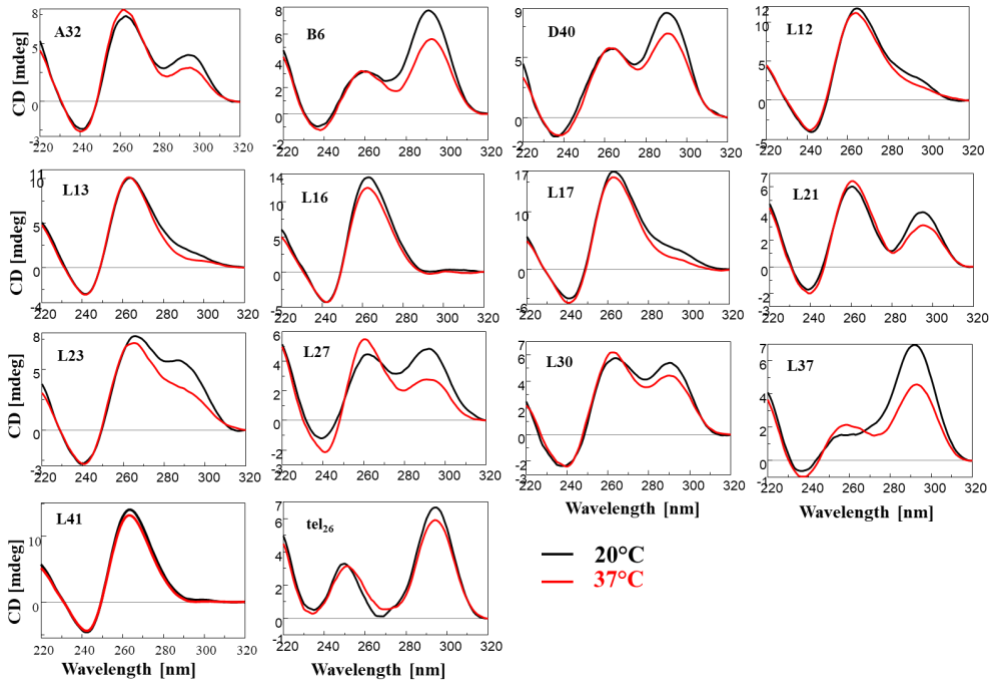

Figure 57. Superimposed CD profiles of N.A. aptamers in PBS, recorded at 20 (black line) and 37 °C (red line).

5.2.5 Studies on the molecularity of the selected aptamers

In order to explore the molecularity of the selected aptamers, polyacrylamide gel electrophoresis (PAGE) experiments under native conditions and size exclusion chromatography analysis were carried out on the N.A. samples in PBS.

5.2.5.1 Native polyacrylamide gel electrophoresis analysis

Electrophoretic experiments (20% polyacrylamide) carried out on the A. aptamers and tel_{26} control sequence showed a single band with the same migration rate, evidencing the exclusive formation of monomolecular species in all cases, including tel_{26} (126).

In the case of the N.A. samples, tel_{26} showed a single monomeric band comparable to the one observed for A. tel_{26}, confirming for this aptamer the exclusive presence of monomolecular species. On the other hand, the other N.A. sequences showed bands with the same electrophoretic mobility of monomeric tel_{26}, as well as retarded bands with different intensities, indicative of the presence of dimeric species in solution (Figure 58). The bands relative to the dimeric species appeared smeared probably as a consequence of fast equilibria occurring in the gel run.

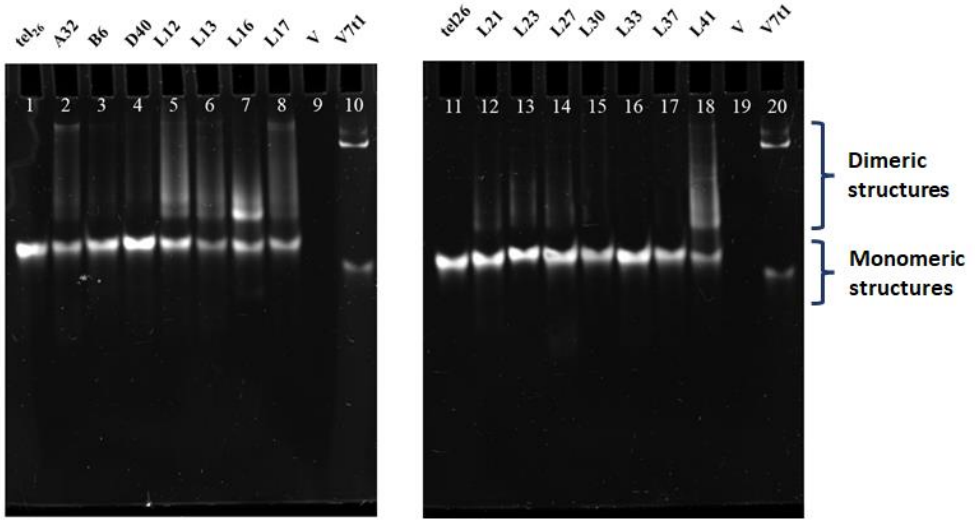

Figure 58. Representative 20% polyacrylamide gel electrophoresis under native conditions of the oligonucleotide samples at 3 µM in PBS, run at 80 V at r.t. for 3 h in TBE 1X buffer. The V7t1 aptamer and tel_{26} were used as controls; indeed, the anti-VEGF 25-mer V7t1 aptamer is known to form both monomeric and dimeric structures when not annealed in Na^+-rich buffer (126), whereas tel_{26} is characterized by a unique monomeric structure (126).

In addition to tel_{26}, also the 25-mer anti-VEGF aptamer V7t1, previously proved to form both monomeric and dimeric G4 structures when N.A. in a Na^+-rich buffer (126) was loaded on the native gel, as control for both monomeric and dimeric G4 species (Figure 58, lanes 10 and 20).

5.2.5.2 Size exclusion chromatography (SE-HPLC) analysis

In order to confirm the presence of dimeric species in the N.A. aptamers in PBS as indicated in the PAGE experiments, size-exclusion chromatography (SEC) analysis was performed.

SEC is a chromatographic method in which molecules in solution are separated on the basis of their size and molecular weight. In our case, we expected to

observe, in the chromatogram, peaks corresponding to dimeric structures, if present, eluted at lower elution time than those relative to monomeric species. The chromatographic profile of the control sequence tel_{26}, both in the A. and N.A. form in PBS, showed, as expected, a single peak, eluting at 9.3 min in our experimental conditions, corresponding to a monomeric G4 structure, in accordance with literature data (126) (Figure 59a).

The chromatograms of the N.A. aptamers in PBS, together with the one of the reference 25-mer V7t1, are reported in Figure 59b. This analysis clearly showed that almost all the aptamers were able to form dimeric G4 structures, even though to a different extent. The relative percentages of dimeric and monomeric species were calculated by peaks integration and are reported in Table 5.

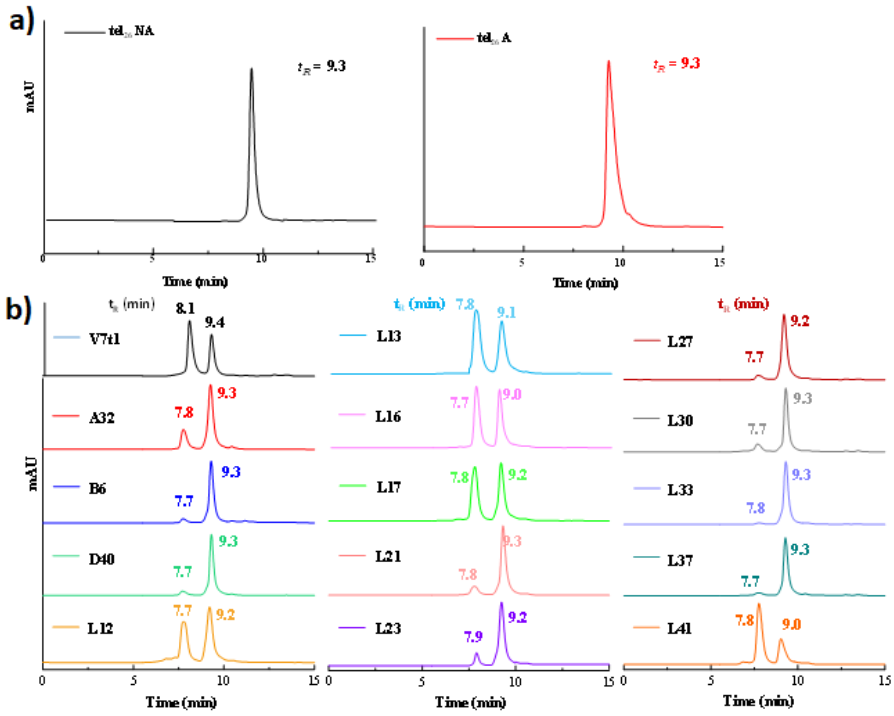

Figure 59. HPLC chromatograms of the oligonucleotide samples in PBS, injected on an analytical SE-HPLC column and eluted with PBS. a) tel_{26}, in both A. and N.A. form; b) N.A. aptamer samples (anti-VEGF V7t1 and anti-HMGB1) in PBS. For each aptamer, elution times of dimeric and monomeric structures are indicated in correspondence to the relative peaks.

From this analysis, the N.A. aptamers in PBS which were essentially monomeric or contained very low dimer percentage (<15%) were: B6, D40, L21, L23, L27, L30, L33 and L37; the aptamers containing an almost similar percentage of monomer and dimer were: L12, L13, L16 and L17. A32 showed a dimeric amount of 22%, whereas L41 showed the highest dimer percentage, i.e. 68% (Table 5).

Table 5. Percentage of monomeric (% monomer) and dimeric (% dimer) structures formed by each analyzed N.A. aptamer in PBS, as derived by the integration of the chromatographic peaks of the samples injected on an analytical SE-column eluted with PBS. tel_{26} only exists in monomeric form.

Aptamer	% dimer	% monomer
V7t1	**57.5**	**42.5**
A32	**22.4**	**77.4**
B6	**5.6**	**94.4**
D40	**8.0**	**92.0**
L12	**40.3**	**49.7**
L13	**54.1**	**45.9**
L16	**52.5**	**47.5**
L17	**49.7**	**50.3**
L21	**12.0**	**88.0**
L23	**12.4**	**87.6**
L27	**5.9**	**94.1**
L30	**12.6**	**87.4**
L33	**2.3**	**97.7**
L37	**6.2**	**93.8**
L41	**68.2**	**31.8**

5.2.6 HMGB1-aptamer interaction experiments: chemiluminescence ELISA (Enzyme-linked immunosorbent assay)-like assays

To explore the ability of the selected aptamers to interact with HMGB1 and estimate their affinity for the protein, binding assays in heterogeneous phase (ELISA-like assays) were designed and performed. For this experiment, we used as solid-phase system a copper-coated 96-well plate able to immobilize with high affinity His-tagged proteins. The assay was based on the following steps:

- immobilization of the HMGB1 protein, labelled with a His-tag tail (HMGB1-His), on the copper-coated 96-well plate, on which Cu^{2+} ions are coordinated with NTA;
- incubation of the N.A. biotinylated aptamers with the HMGB1-functionalized plate;
- binding of horseradish peroxidase (HRP) conjugated to streptavidin to the biotinylated aptamers retained on the plate;
- incubation of the so-assembled sandwich with an HRP-substrate able to produce a chemiluminescent product in solution in the presence of H_2O_2, generating a detectable luminescence signal.

The chemiluminescence intensity is correlated with the amount of aptamer attached to the plate, which is directly proportional to the affinity for HMGB1. The chemiluminescence signal in the wells treated as previously described, but with a non-biotinylated aptamer was indicated as “blank”. The experiment showed that all the aptamers interacted with the protein, as expected

considering that they were selected by a SELEX process using HMGB1 as the target, but with varying degrees (Figure 60). Specifically, A32, L12, L13, L16, L17 and L41 were able to bind HMGB1 with the highest affinity, while the other aptamers showed a lower affinity for the protein. Interestingly, the aptamers with the highest affinity for HMGB1 were also the ones containing the highest percentage of dimeric structures, as indicated by HPLC analysis, whereas tel_{26}, only monomeric, evidenced almost no affinity (chemiluminescence signal comparable to the blank) for HMGB1 in the studied experimental conditions. These findings suggested a correlation between molecularity of the analyzed sequences and affinity for the target protein. Moreover, we showed that aptamers with the highest percentage of dimeric species were the ones with the highest content of parallel G4 conformation, so we can hypothesize that HMGB1 preferably interacts with parallel dimeric G4 structures.

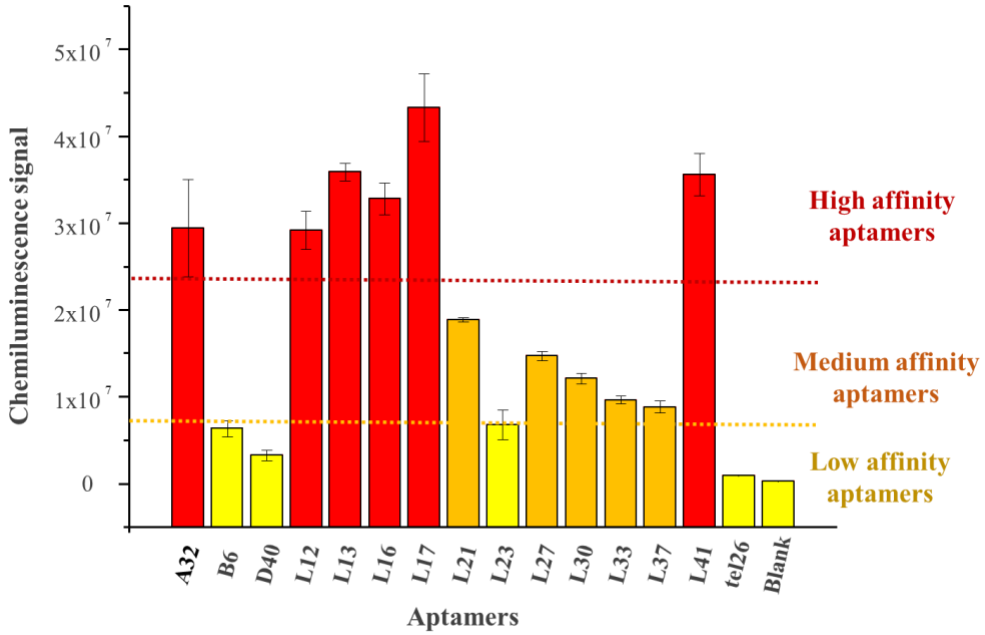

Figure 60. HMGB1-aptamers interaction assay: the measured chemiluminescence is correlated with the affinity of each N.A. aptamer for HMGB1.

Interestingly, ELISA-like assays performed on the A. aptamers showed very low chemiluminescence values (two orders of magnitude lower than those obtained for the N.A. aptamers) comparable to the blank (Figure 61). Therefore, no binding affinity could be measured for the A. aptamers with this technique.

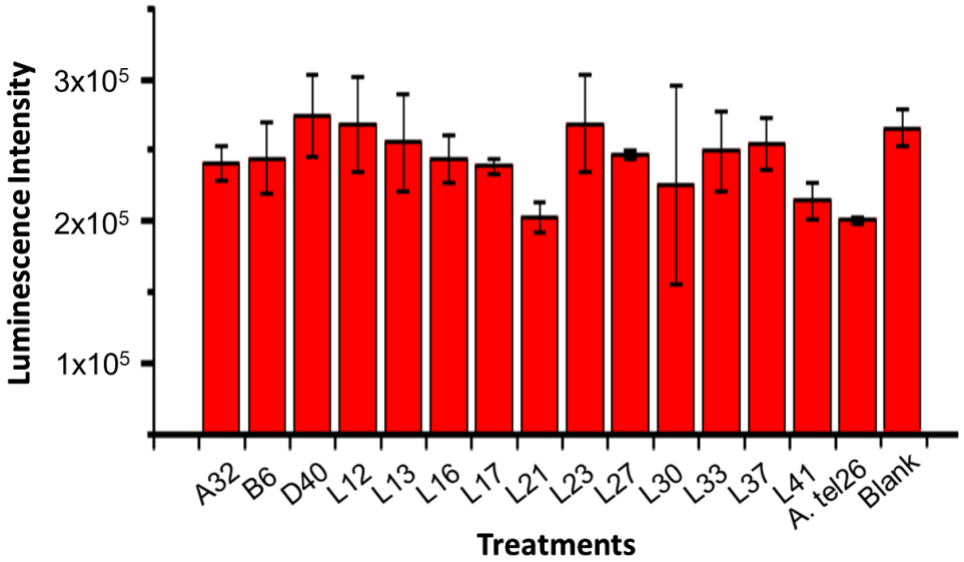

Figure 61. HMGB1-aptamers interaction assay with A aptamers: the measured chemiluminescence is correlated with the affinity of each aptamer for HMGB1.

5.2.7 Evaluation of the enzymatic stability of the selected aptamers

The susceptibility of a specific oligonucleotide to nuclease degradation in serum is one of the most crucial parameters for its potential *in vivo* applications. In order to evaluate the stability of the selected N.A. aptamers in serum, the resistance in FBS of the oligonucleotides with the highest affinity for HMGB1 (according to the ELISA-like assays described in section 5.2.6) was tested. In detail, N.A. A32, L12, L13, L17 and L41 in PBS were incubated in 80% (v/v) FBS at 37 °C for 48 h. Aptamers with low affinity for HMGB1, *i.e.* B6 and D40, and the control sequence tel_{26}, were also incubated in FBS and monitored over time. Aliquots of all these mixtures were collected at fixed times, supplemented with formamide to immediately stop the nuclease degradation, and stored at -20 °C until analysis. Thereafter, all the samples

were loaded on 20% polyacrylamide denaturing gel (Figure 62). The intensity of the bands on the gel for each N.A. sequence at the different analyzed time points was then measured and expressed as a normalized percentage with respect to that of the untreated oligonucleotide (Figure 63, black squares). The data obtained for the A. aptamers were reported in the same graphic for comparison (Figure 62, red dots). A classical exponential decay behavior was observed for all the N.A. aptamers up to a certain time, after which we observed an almost constant intensity of the remaining band up to 48 h. In particular, the time point for this trend change was ca. 24 h, with a % of the remaining band at 48 h of about 40% (L12), 47% (L13), 13% (L16), 29% (L17), 32% (L41), 20% (A32), 5% (B6), and 7 % (D40), respectively for each specified aptamer. This behaviour could be attributed to the coexistence of more than one species in solution for each aptamer, *i.e.* monomers and dimers, with very different enzymatic degradation rates. It is plausible that the monomeric G4s are more exposed to nuclease digestion and for this reason are degraded faster than the more compact dimeric ones, which in turn show a slower degradation. By considering that the percentage of the remaining bands at 48 h was higher in the samples with higher dimer percentage (Table 5), it is plausible that the dimers are actually the species with the highest resistance, left undegraded even after 48 h FBS incubation, particularly for L12, L13 and L17.

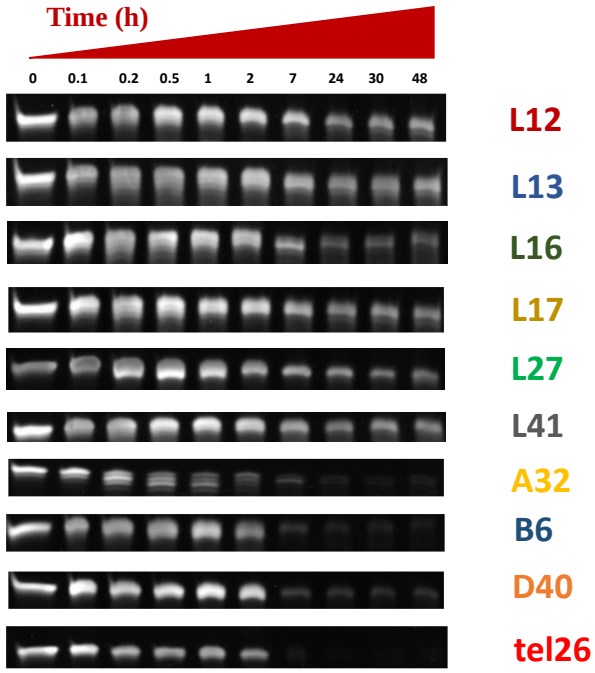

Figure 62. Enzymatic resistance experiments performed on N.A. oligonucleotide aptamers incubated in 80% (FBS), as monitored by 20% denaturing polyacrylamide gel electrophoresis for 24 h (time points: 0, 0.1, 0.2, 0.5, 1, 2, 7, 24, 48 h). For each compound, a representative 20% denaturing PAGE (8 M urea) is reported: samples were loaded at 3 µM, and the gels were run at 200 V constantly, at r.t., for 3 h in TBE (Tris, Borate, EDTA) 1X (running buffer).

Notably, the N.A. aptamers showing the highest enzymatic resistance (L12, L13, L16, L17 and L41) in the investigated series share the same main features, *i.e.*: a) prevalent parallel G4 conformation; b) high percentage of dimeric structures and c) high thermal stability. These N.A. aptamers strongly differed in conformational behavior and thermal stability from the A. ones. In contrast, the N.A. aptamers whose overall conformations and thermal stabilities did not significantly differ from the A. ones, *i.e.* B6 and D40, showed also similar enzymatic stability, as reported in Figure 62. These aptamers have the following features: a) prevalent antiparallel/hybrid conformations; b) lower

thermal stability; c) lower enzymatic stability and d) lower dimeric species content compared with L12, L13, L16, L17 and L41. A comparison of the aptamer band decay as a function of the incubation time in the enzymatic stability experiments for representative A. and N.A. aptamers is reported in Figure 63.

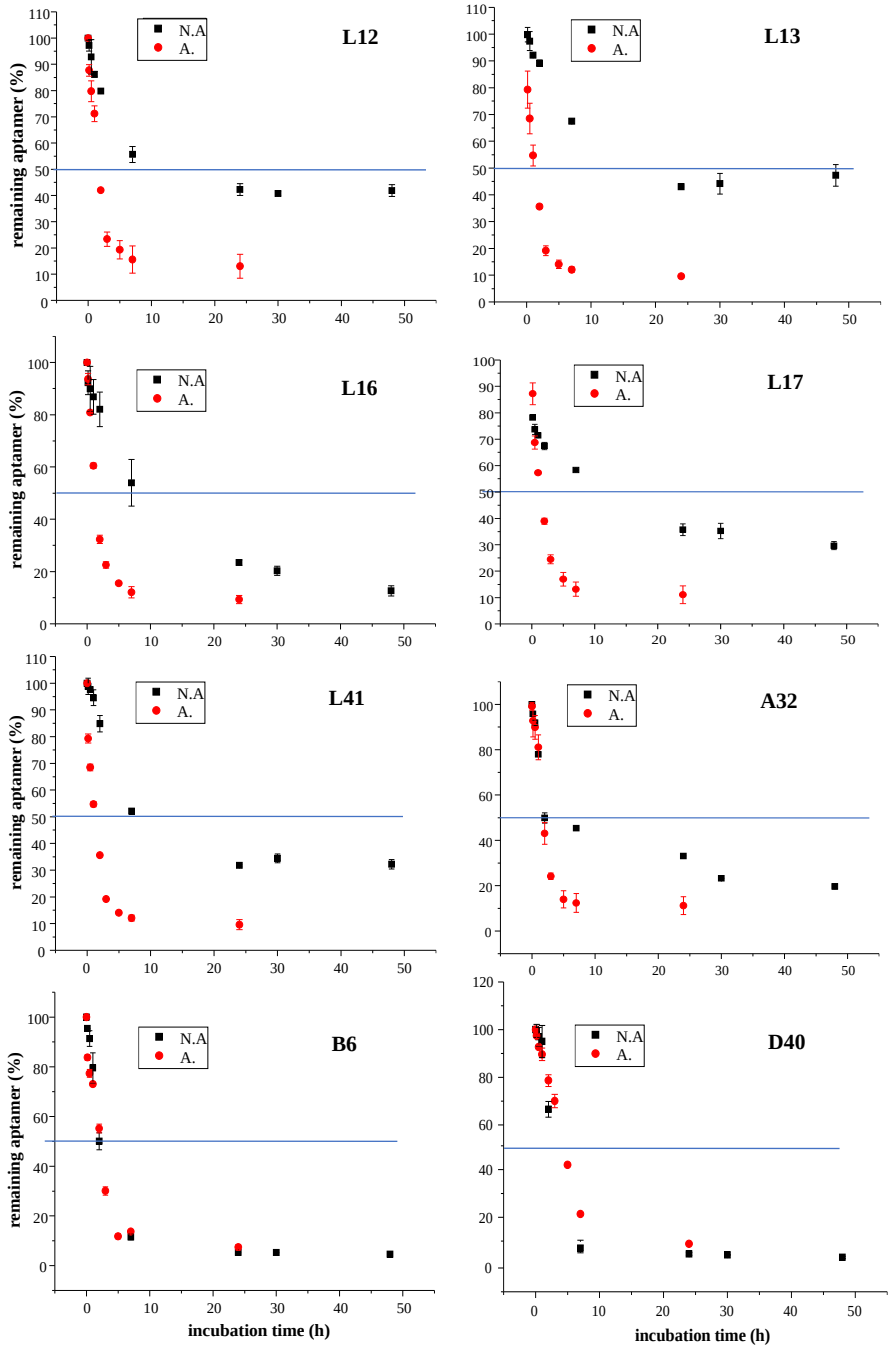

Figure 63. Comparison of the aptamer band decay as a function of the incubation time in the enzymatic stability experiments for representative A. and N.A. aptamers.

5.2.8 Evaluation of the anti-HMGB1 aptamers bioactivity by *in vitro* cellular migration assays

In order to evaluate the *in vitro* activity of the selected aptamers, we tested their ability to inhibit HMGB1-induced cell migration. Chemotaxis assays were performed according to the protocols described by Palumbo et al. (271). NIH3T3 cells (mouse embryonic fibroblasts) were suspended in serum-free DMEM (Dulbecco's Modified Eagle's Medium) and an aliquot was added to the upper layer of a cell culture insert equipped with a permeable membrane (transwell). N.A. aptamers were diluted in the same serum-free medium and added to the lower layer of the well on the plate with or without added HMGB1. HMGB1 concentration was optimized for migration in a separate experiment at 10 nM; the aptamers were used at 100 nM concentration. In the absence of HMGB1, cell migration was only basal (negative control, green column of the histogram in Figure 64). By adding HMGB1, cells migrated to a significant extent (positive control, orange column Figure 64). In the presence of the aptamers, in all the explored cases, the HMGB1-induced migration was inhibited, even though to a different extent. The obtained results showed that the best aptamers in blocking HMGB1-induced cell migration were A32, L12, L13, L16, L17 and L41 (Figure 64). Moreover, a good correlation between aptamer affinity and inhibitory activity towards the protein was evidenced. Interestingly, the most active aptamers proved to be the ones with the highest amount of dimeric parallel G4 structures.

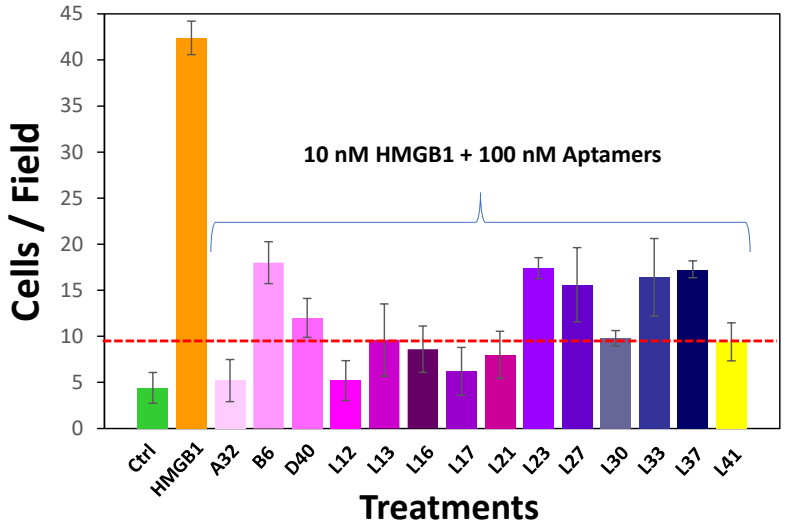

Figure 64. Chemotaxis assay data on NIH3T3 cells. Treatment "Ctrl": serum-free culture medium corresponding to the negative control (basal level of cell migration). Other treatments: 10 nM HMGB1 (positive control, orange column), and 10 nM HMGB1 combined with 100 nm of each aptamer.

The overall data collected for the N.A. aptamers, especially those relative to the thermal stability of their G4 structures, enzymatic resistance, HMGB1 binding affinity and above all *in vitro* anti-HMGB1 activity, allowed us selecting L12 as the best candidate aptamer. Indeed, L12 was then more in-depth investigated performing dose-response cellular experiments. Thus, when cells were incubated with 10 nM HMGB1 and increasing amounts of L12 in the 5-150 nM range, a concentration-dependent inhibition of migration was observed (Figure 65a) with a calculated IC_{50} value of ca. 28 nM (Figure 65b).

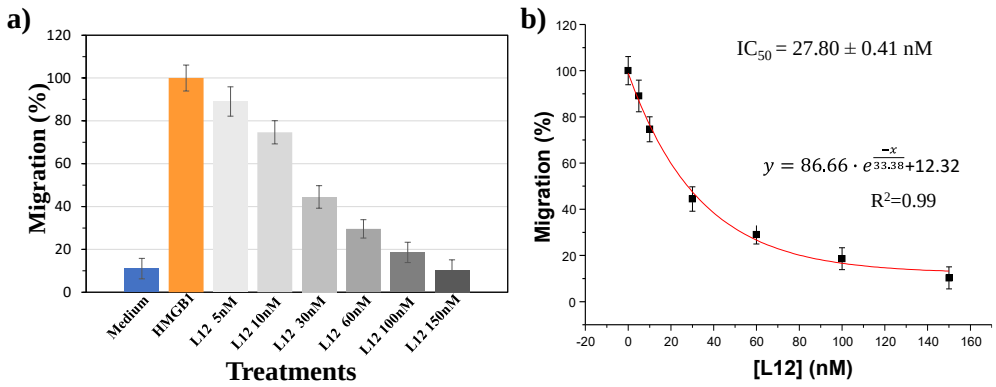

Figure 65. Chemotaxis assay data on NIH3T3 cells. a) Cell migration expressed as percentage of the positive control (10 nM HMGB1) at different treatments. "Medium": serum-free culture medium corresponding to the negative control (basal level of cell migration). Other treatments: 10 nM HMGB1 (positive control, orange column) and 10 nM HMGB1 with various concentrations (5-150 nM) of N.A. L12 aptamer. b) Evaluation of the IC_{50} for HMGB1 inhibition by L12, based on the cell migration – reported as percentage of the positive control - as a function of L12 concentration.

5.2.9 Separation and analysis of the dimeric and monomeric species of the NA L12 aptamer

In order to more deeply investigate the oligonucleotide selected as the best-performing aptamer for HMGB1 inhibition, we performed an HPLC separation of N.A. L12 in PBS on the analytical SE-column so to collect and separately analyze its dimeric and monomeric species. The collected peaks were then studied by CD and native gel electrophoresis analyses. The CD spectrum of the peak at lower retention time, identified as the dimer, showed the typical features of a parallel G4 structure, whereas the peak relative to the monomer (higher elution time) showed a CD spectrum characteristic of a hybrid type G4 (Figure 66a). No conformational equilibrium between the two species was observed up to 5 h, since their CD spectra remained unaffected in this time range.

Furthermore, we also analyzed the molecularity of each peak by gel electrophoresis under native conditions after 24 h from the HPLC separation, keeping the samples at r. t. before the analysis. No evidence of interconversion of the dimer into the monomer and *vice versa* was observed (Figure 66b), confirming their stability at r. t.

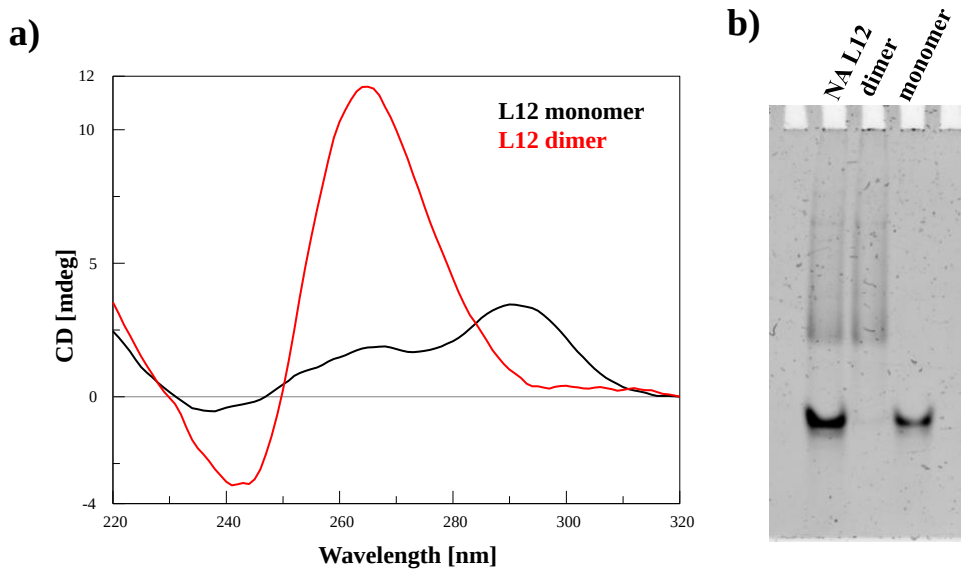

Figure 66. a) Overlapped CD spectra of the separated HPLC-peaks relative to the monomeric and dimeric N.A. L12; b) representative 20% polyacrylamide gel electrophoresis under native conditions of the N.A. L12 samples at 3 µM and of the separated HPLC-peaks relative to the monomeric and dimeric N.A. L12 in PBS. Run at 80 V at r.t. for 3 h in TBE 1X buffer.

Finally, we tested the isolated monomer and dimer species of L12 in their ability to inhibit HMGB1-induced cellular migration in chemotaxis assays with the proper controls. The obtained results showed that the isolated dimer was more active than L12 as a mixture of monomeric and dimeric species, whereas the monomeric species proved to be the least active species (Figure 67).

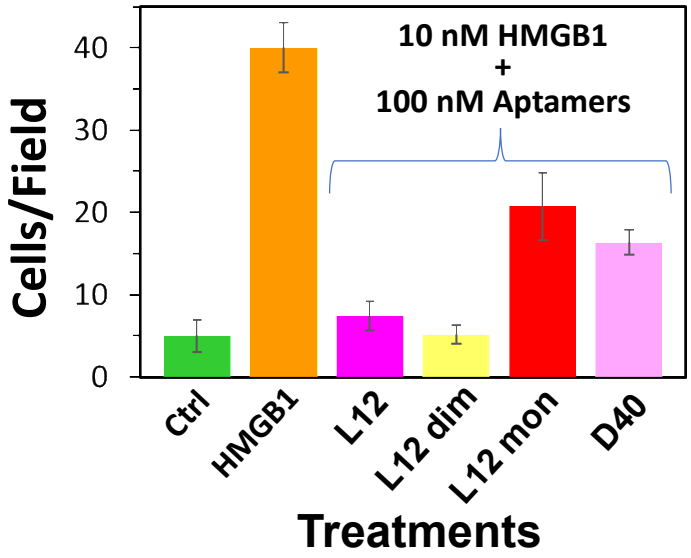

Figure 67. Chemotaxis assay on NIH3T3 cells. Number of migrated cells per field for different treatments. Medium: serum-free culture medium corresponding to the negative control (basal level of cell migration, green column). Other treatments: 10 nM HMGB1 (positive control, orange), and 10 nM HMGB1 together with 100 nM concentration of the indicated samples.

5.3 Experimental section

The oligonucleotide sequences reported in section 5.2.1 were purchased from biomers.net GmbH (Germany) in lyophilized form and their identity and purity were confirmed by MALDI-TOF mass spectrometry and high-performance liquid chromatography (HPLC) data provided by the commercial supplier. The oligonucleotides were dissolved in ultra-pure nuclease-free water (VWR) and their concentrations were determined by UV-vis analysis measuring the absorbance at 260 nm and 95 °C using their respective molar extinction coefficients. All the used aptamer solutions were obtained by diluting a stock solution (around 0.2 mM) prepared in water with the selected buffer, *i.e.* a pseudo-physiological Na^+-rich buffer (137 mM NaCl, 2.7 mM KCl, 10 mM

NaH_2PO_4/Na_2HPO_4, 1.8 mM KH_2PO_4/K_2HPO_4, pH = 7.3), here indicated as PBS. Annealed (A.) samples were obtained by heating the appropriate oligonucleotide solutions at 95 °C for 5 min and leaving them to cool to r.t. overnight. Not-annealed (N.A.) samples were obtained by simply diluting the stock solutions in PBS at r.t. to provide the required concentrations. N.A. and A. samples were then kept at 4 °C until use. Recombinant human HMGB1 (HMGBiotech, Milan, Italy) and His-tag labelled HMGB1 (GenScript) were purchased from Tecan Group Ltd. (Männedorf, Switzerland) and D.B.A. srl (Italy), respectively. Protein concentration was confirmed by Bradford assay (Bio-Rad) using Bovine Serum Albumin (BSA) as standard.

5.3.1 UV-vis spectroscopy experiments

The UV-vis spectra were obtained on a Jasco V-630 UV-vis spectrophotometer equipped with a Peltier Thermostat JASCO ETCS-761, using 1 cm path length cuvettes (1 mL internal volume, Hellma) and recording in the 230-650 nm range using a scanning speed of 100 nm/min with appropriate baseline subtraction.

UV thermal difference spectra (TDS) were obtained by subtracting the UV spectra recorded at a temperature well below the melting temperature (T_m), *i.e.* 10 °C, at which the aptamers are fully folded, from the UV spectra recorded well above the T_m, *i.e.* 90 °C, where the oligonucleotides are fully unfolded (267, 269). Spectra were registered at 20 °C in the 220-320 nm range with 2 s response, 100 nm/min scanning speed, and 2.0 nm bandwidth, corrected by subtraction of the background scan with buffer and averaged over 3 scans. The experiments were performed on N.A. and A. aptamer samples in PBS buffer at 2 μM concentration.

5.3.2 Circular dichroism spectroscopy experiments

CD spectra and CD-monitored melting curves were recorded in a quartz cuvette with a path length of 1 cm (3 mL internal volume, Hellma) on a Jasco J-1500 spectropolarimeter equipped with a Jasco CTU-100 circulating thermostat unit. For the melting experiments, the ellipticity, at the maximum observed for each oligonucleotide, was recorded in the 10-90 °C range with 1 °C/min scan rate. For the singular value decomposition (SVD) analysis, the CD spectra were normalized to molar circular dichroism $\Delta\varepsilon$ = (M^{-1} cm^{-1}) using the equation $\Delta\varepsilon = \theta / (32980 \times C \text{ x } l)$, where θ is the observed CD ellipticity in millidegrees, C is the oligonucleotide concentration in mol/L, and l is the optical path length of the cell in cm. The resulting spectra were then analyzed using the advanced software developed by del Villar-Guerra et al. (232). Data from the melting experiments were converted into normalized CD signal (α) calculated as: $\alpha = [\theta_{obs}(T) - \theta_U)/(\theta_F - \theta_U)]$, where $\theta_{obs}(T)$ is the CD maximum ellipticity in millidegrees observed for each oligonucleotide at each temperature, while θ_F and θ_U are the CD ellipticity values in millidegrees for the same folded (T = 10 °C) and unfolded (T = 90 °C) oligonucleotide, respectively. The T_m values were estimated as the minima of the first derivative plots of the melting curves and the error associated with the T_m determination was ±1 °C.

5.3.3 Denaturing gel electrophoresis experiments

Acrylamide/bis-acrylamide (19:1) 40% solution, glycerol and GelGreen Nucleic Acid Stain were purchased from VWR. Ammonium persulfate (APS) and tetramethylethylenediamine (TEMED) were purchased from Sigma Aldrich. Each oligonucleotide sample (30 pmol) in water was mixed with

formamide (1:2, v/v) at 95 °C for 5 min to completely unfold its structure, and then left in ice until loading on the gel. Just before loading, all the samples were supplemented with 5% glycerol and analyzed by electrophoresis on 20% denaturing polyacrylamide gels using 8 M urea in TBE 1X as running buffer. The gels were run at r.t., at constant 200 V for 3 h, then stained with Gel Green (supplemented with 0.1 M NaCl) for 30 min and visualized using UV transilluminator (BioRad ChemiDoc XRS, Milan, Italy).

5.3.4 Native PAGE experiments

Oligonucleotides samples (6 μM) in PBS were loaded on 20% polyacrylamide gels in TBE 1X as running buffer. All the samples were supplemented with 5% glycerol just before loading (final concentration 3 μM) and then run, under native conditions, at 80 V at r.t. for 3 h. Gels were stained with Gel Green and visualized using UV transilluminator (BioRad ChemiDoc XRS, Milan, Italy).

5.3.5 Size exclusion chromatography (SE-HPLC) analysis

SE-HPLC analyses were performed on an Agilent HPLC system, equipped with a UV/vis detector, using a Yarra 3 μm analytical column (300 × 4.60 mm; Phenomenex). The elution was monitored at $\lambda = 254$ nm using a 0.35 mL min^{-1} flow rate. The mobile phase used was PBS (pH 6.9). 2 μM solutions of each aptamer were loaded at each injection, while for the HPLC separation of the monomeric and dimeric species of L12, a 20 μM solution of the aptamer was used. The final concentration of the two separated samples was determined by UV analysis. The error associated with the retention time (t_R) determination is within ±5%.

5.3.6 Chemiluminescence-based binding studies on the interaction of HMGB1 with the selected aptamers

A copper-coated 96-well plate (Copper Coated High-Capacity Plates, Thermo Scientific) was incubated under gentle shaking for 1 h with 100 µL of 0.2 µM HMGB1-His solution in PBS. After supernatant removal, each well was washed three times using 200 µL of a PBS solution containing 0.05 % (*v*/v) Tween-20 (Sigma- Aldrich). The wells were treated with 100 µL of 1.5 µM biotinylated aptamer solutions in PBS and incubated at r.t. for 1 h under slow shaking. After another washing cycle, in each well was deposited a solution of streptavidin-HRP (BPS Bioscience) diluted in Blocking Buffer (PBS with 0.05 % (*v*/v) Tween 20 and 2 % (m/v) BSA) and the plate was then incubated under gentle shaking. After 1 h, the supernatant was removed and three washings were performed. Then, after addition to each well of 100 µL of the Blocking Buffer, enhanced chemiluminescence (ECL) HRP substrate (BPS Bioscience) was added and the HRP activity was measured by a multilabel plate reader (Glomax Discover System, GM3000). The experimental procedures were performed at r.t. in duplicate.

5.3.7 Serum stability assays of the aptamers monitored by gel electrophoresis analysis

The oligonucleotides were dissolved in PBS buffer (50 µM) and incubated in 80 % FBS 80% at 37 °C to a final concentration of 10 µM. Then, at fixed times, 3 µL of the samples (30 pmol) were collected, mixed with formamide (1:2, v/v) to immediately stop the enzymatic degradation, heated at 95 °C for 2 min, and stored at -20 °C until analysis. All the samples were supplemented with

5% glycerol and analyzed by electrophoresis on 20% denaturing polyacrylamide gels using 8 M urea in TBE 1X as running buffer. The gels were run at r.t., at constant 200 V for 3 h, then stained with Gel Green (supplemented with 0.1 M NaCl) for 30 min and visualized using UV transilluminator (BioRad ChemiDoc XRS, Milan, Italy). Each experiment was performed in triplicate. The intensity of the DNA bands on the gel, at each collected time, was then quantified by using the Image J software and normalized with respect to the untreated oligonucleotides. Percentages of the remaining oligonucleotides were reported as mean values ± SD for the multiple determinations.

5.3.8 Transwell cell migration assay (Boyden chamber assay)

Boyden chamber assays (272) were performed using transwell 24-well plates (Greiner) carrying two medium-containing chambers separated by a porous polycarbonate membrane PVP free filters (8 μm pore size, 6.4 mm diameter) (cellQART®) through which cells can migrate. The lower compartment was filled with: 1) 600 μL serum-free DMEM (negative control), 2) 600 μL serum-free DMEM containing the chemotactic agent (HMGB1 10 nM, positive control), 3) 600 μL serum-free DMEM containing 10 nM HMGB1 and 100 nM aptamers, 4) 600 μL serum-free DMEM containing 10 nM HMGB1 and various aptamer concentrations (5-150 nM), 5) 600 μL serum-free DMEM with 100 nM aptamer in the absence of HMGB1 (additional negative control). The membranes were first treated with 20 μL *per* filter of a 50 μg mL^{-1} fibronectin solution left to dry for 1 h inside a laminar flow hood. Then, 50 000 NIH3T3 fibroblast cells in 100 μL serum-free DMEM were seeded in the upper

compartment. After 4 h in incubator (37 °C, 5% CO_2), the upper suspension was removed, and the cells were fixed and stained with 0.1% crystal violet (145 mM NaCl, 0.5% formal saline, 50% ethanol) for 10 min. After exhaustive washings with water, the upper side of the filters was scraped using a cotton swab to remove cells that did not migrate in the lower compartment. The number of migrated cells was determined using a phase-contrast microscope and counting them at 40x zoom in 10 random fields per filter using the Image J software. All the data represent the mean ± SEM of duplicate measurements. The assays were performed at least in duplicate, with very good reproducibility.

5.4 Conclusions

In this work, 14 G-rich oligonucleotides interacting with HMGB1 were selected by SELEX, starting from a partially randomized library constructed using as a model the G4 forming sequence tel_{26}, a 26-mer truncated part of the human telomere 3'-overhang, previously demonstrated to interact with this protein.

To investigate the conformational behavior of these aptamers and evaluate their thermal and enzymatic stabilities in PBS − a buffer mimicking the extracellular environment where HMGB1 exerts its cytokine activity – an in-depth biophysical and biological characterization, using different techniques, was performed. First of all, the aptamers were analyzed after an annealing (A.) procedure, favouring their structuring into the thermodynamically preferred conformations. In these conditions, the A. aptamers showed: a) monomeric G4 structures largely preferring antiparallel/hybrid conformations over the parallel ones; b) melting temperatures in the 32-48 °C range, in many cases very close

to the physiological temperature; c) quite short half-life times in serum (FBS), ranging between 1 and 3.6 h; d) low binding affinities for HMGB1.

Then, the aptamers were studied without annealing (N.A.), *i.e.* without any prior thermal treatment, simply diluting in PBS at r. t. the concentrated stock solutions in pure water, following a procedure which favours their kinetic conformations.

TDS analysis demonstrated that, in the explored buffer conditions (PBS), all the N.A. aptamers adopted G4 conformations. The CD spectra of the N.A. oligonucleotide sequences in PBS confirmed this finding. The aptamers were thus classified into 4 different families based on their predominant G4 conformation, in accordance with the SVD analysis of the CD spectra, that gives an estimation of the percentages of each G4 topology in solution for each aptamer. The investigated aptamers showed a marked G4-polymorphism, in no case showing a single preferential conformation. CD-melting analysis on the N.A. aptamers showed excellent thermal stability for their G4 structures, with T_m values far higher than 37 °C in PBS. Interestingly, for several aptamers, a very different conformational behaviour between A. and N.A. samples was observed, together with a marked difference in the melting temperatures. In many cases, a noteworthy increase of the thermal stability of N.A. aptamers in comparison to the corresponding A. ones was evidenced, whereas aptamers having similar conformations under A. and N.A. conditions showed similar T_m values.

In order to study the molecularity of the investigated systems, PAGE and SE-HPLC analyses in PBS were carried out. The experiments showed that the sequences A32, L12, L13, L16, L17, L41 formed monomeric species, as well as significant amounts of dimeric G4 structures, under the studied conditions.

Preliminary data on the HMGB1–aptamers interactions were obtained with a chemiluminescence ELISA-like assay using copper–coated 96-well plates. All the N.A. anti–HMGB1 sequences showed ability to bind the protein, as expected considering that they were identified by a SELEX process using HMGB1 as the target. Remarkably, the protein showed particularly high binding affinity for those aptamers containing a medium-to-high-content of dimeric G4 structures. In contrast, using the same assay, the A. aptamers showed a very low affinity for the protein, since the luminescence signals were in all cases under the sensitivity limit of the technique, *i.e.* at least one order of magnitude lower with respect to their N.A. counterparts.

To explore the *in vitro* and *in vivo* applicability of the aptamers with the highest affinity for the target protein, their enzymatic stability in 80% FBS monitored over time was evaluated by denaturing PAGE assays, showing in all cases that the aptamers with the highest enzymatic stability were those with the highest content of dimeric parallel G4 structures.

Cell migration assays were then performed to evaluate the *in vitro* activity of the selected aptamers, evidencing A32 and L12 as the best aptamers in terms of inhibition of the cell migration induced by the protein. Correlating these data with all the other experimental results, such as thermal and enzymatic stabilities, as well as binding affinities for the target, L12 was identified as the best candidate aptamer, on which a more in-depth investigation was carried out. Particularly, dose-response migration assays were performed on this aptamer in N.A. conditions, obtaining a concentration-dependent inhibition of migration induced by HMGB1 with an IC_{50} value of about 28 nM.

Taken together, these data show this aptamer as a very promising anti-HMGB1 inhibitor, with properties well superior to other known specific HMGB1 ligands, as *e.g.* glycyrrhizin having an IC_{50} value of 50 μM.

General conclusions

In this PhD thesis I studied aptameric systems for diagnostics and theranostics targeting VEGF and HMGB1, two proteins involved in anti-inflammatory and cancer-related diseases. In the first project, described in Chapter 3, a novel fluorescent cyanine probe (CyOH), designed as an analogue of thiazole orange, a well-known G4 ligand, was synthesized, carrying a hydroxypropyl group instead of a methyl group, greatly improving its solubility in water, pivotal element for potential *in vitro* and *in vivo* applications. Remarkably, this probe was able to strongly bind the V7t1 or 3R02 aptamers, giving a dramatic fluorescence enhancement only in the presence of their dimeric or multimeric forms, which recognize the target protein with higher affinity than the monomeric species.

Interestingly, by simply mixing in solution CyOH with the not-annealed V7t1 or 3R02 aptamers, stable complexes between the probe and the dimeric or multimeric aptamers were obtained. These complexes were able to enter the cells, recognizing their specific VEGF target protein and giving a clear and intense fluorescent signal detectable by CLSM. In conclusion, I here realized a proof-of-concept based on non-covalently bound systems, ready-to-use after simple mixing in solution, that proved to be very promising for diagnostic applications, with efficacy comparable with that of a specific fluorescent anti-VEGF antibody. The major advantages of these systems can be resumed in two aspects: 1) the aptamers do not need any pretreatment; 2) they do not require any chemical modification with linkers to connect the probe, which of course may affect the aptamer correct folding for protein recognition.

During my research period abroad at TU Dortmund in prof. Guido Clever's group, as described in Chapter 4, intrigued by the ability of the dimeric V7t1 aptamer to recognize the target VEGF protein with higher affinity than the monomeric aptamer, through solid phase synthesis, I installed two pyridine-

containing ligandosides in different strategic position at 5' or 3'-end of the V7t1 sequence. A set of different modified oligonucleotides was thus obtained with the aim to force their dimerization through the coordination with transition metals of the pyridine moieties (two pyridines per sequence in a dimeric species allow coordinating a bivalent metal cation).

An in-depth biophysical characterization will be performed in the near future by evaluating the synthesized aptamers in the presence of different promising transition metals like Pt^{2+}, Cd^{2+}, Ni^{2+} with the aim of finding the best conditions for pyridine coordination and aptamer dimerization. The modified aptamers will be then evaluated in their interaction with the target VEGF protein through appropriate techniques, like EMSA and chemiluminescence ELISA-like assays.

In Chapter 5 I focused on anti-HMGB1 aptamers as potential drugs in anti-inflammatory and cancer therapies. Starting from a library of different oligonucleotide aptamers inspired by tel_{26} – the G4 forming 26-mer truncation of the human telomeric DNA, able to interact with HMGB1 – through SELEX I obtained 14 aptamers which were in-depth characterized by using biophysical and biological techniques in PBS, a Na^+-rich buffer mimicking the extracellular environment where HMGB1 exerts its pivotal cytokine activity. In this way, I selected 6 aptamers – A32, L12, L13, L16, L17, L41 – which proved to be the best ones in terms of melting temperatures, nuclease resistance, affinity for the target HMGB1 protein and ability to inhibit HMGB1-induced migration in cells. Interestingly, all the selected aptamers proved to fold into parallel G4s, with significant amounts of dimeric species, demonstrating that the target protein has a preference for this kind of structures. Among the tested oligonucleotide sequences, L12 was identified as the best anti-HMGB1 aptamer, being featured by high bioactivity (IC_{50} value of about

28 nM) and remarkable thermal and enzymatic stability, which indicate it as a very promising lead candidate for future *in vivo* studies. These results are of exceptional value for the future development of potential drugs based on anti-HMGB1 therapeutic strategies and specific biosensors for this protein, *e.g.* in liquid biopsies. Future studies will be performed to evaluate the interaction of L12 with specific fluorescent probes – *e.g.* CyOH – with the aim to combine diagnostics and theranostics in the battle against anti-inflammatory and cancer-related diseases.

Abbreviation

ACE2, angiotensin-converting enzyme 2;

AGE, advanced glycation end products;

ALI, acute lung injury;

AMD, age-related macular degeneration;

APS, ammonium persulfate;

ARDS, acute respiratory distress syndrome;

ATCC, american type culture collection;

BSA, bovine serum albumin;

C1q, component 1q protein;

CD, circular dichroism;

CD163, cluster of differentiation 163;

CEP, cyanoethyl phosphoramidite;

CLSM, confocal laser scanning microscopy;

CPG, controlled pore glass;

CS, cytokine storm;

DAD, diode array detector;

DAMP, damage-associated molecular pattern molecule;

DC, dendritic cells;

DMEM, Dulbecco's modified eagle medium;

DMT, 4,4'-dimethoxytrityl;

EC, endothelial cells;

ECL, enhanced chemiluminescence;

ECM, extracellular matrix;

EDTA, ethylenediaminetetraacetic acid;

EMSA, electrophoresis mobility shift assay;

EPR, electric paramagnetic resonance;

ERK, extracellular signal-regulated kinase;

ESI, electrospray ionization;

Et, ethyl;

FDA, Food and Drug Administration;

FLIM, fluorescence lifetime imaging;

G4, G-quadruplex;

HBD, heparin binding domain;

HIF, hypoxia-inducible factor;

HMGB1, High-Mobility Group Box 1;

Hp, protein haptoglobin;

HPLC, high performance liquid chromatography;

HRP, horseradish peroxidase;

ICD, induced circular dichroism;

IFN-γ, interferon gamma;

LAIR-1, leukocyte-associated immunoglobulin-like receptor 1;

MAPK, mitogen-activated protein kinase;

MCF, Michigan cancer foundation;

Me, methyl;

MEGM, mammary epithelial cell growth medium;

MS, mass spectrometry;

MTT, 3-(4,5-dimethylthiazol-2-yl)-2,5-diphenyltetrazolium bromide;

NDI, naphthalene diimide;

NET, neutrophil extracellular trap;

NF-kB, nuclear factor kappa-light-chain-enhancer of activated B cells;

NLRP3, node-like receptor pyrin 3;

NMR, nuclear magnetic resonance;

NTA, nitrilotriacetic acid;

PAGE, polyacrylamide gel electrophoresis;

PBS, phosphate buffered saline;

PCR, polymerase chain reaction;

PDAC, pancreatic ductal adenocarcinoma;

ppm, part per million;

PQS, putative G-quadruplex forming sequences;

PRR, pattern recognition receptor;

RBD, receptor binding domain;

SA, salicylic acid;

SELEX, systematic evolution of ligands by exponential enrichment;

SP-1, specificity protein 1;

SVD, singular value decomposition;

TAE, tris-acetate-EDTA;

TBE, tris-borate-EDTA;

TDS, thermal difference spectrum;

TEMED, tetramethylethylenediamine;

TFA, trifluoroacetic acid;

ThT, thioflavin T;

TLC, thin-layer chromatography;

TLR2/TLR4, toll-like receptors 2 and 4;

TM, thrombomodulin;

TNF, tumour necrosis factor;

TO, thiazole orange;

$\mathbf{T_m}$, melting temperature;

UPLC, ultra-performance liquid chromatography;

UV, ultraviolet spectroscopy;

VEGF, vascular endothelial growth factor.

References

1. Crick,F. and Watson,J. (1953) A structure for deoxyribose nucleic acid. *Nature*, **171**, 737–738.

2. Kaushik,M., Kaushik,S., Roy,K., Singh,A., Mahendru,S., Kumar,M., Chaudhary,S., Ahmed,S. and Kukreti,S. (2016) A bouquet of DNA structures: Emerging diversity. *Biochem. Biophys. Reports*, **5**, 388–395.

3. Mirkin,S.M. (2008) Discovery of alternative DNA structures: a heroic decade (1979-1989). *Front. Biosci.*, **13**, 1064–1071.

4. Wang,G. and Vasquez,K.M. (2014) Impact of alternative DNA structures on DNA damage, DNA repair, and genetic instability. *DNA Repair.*, **19**, 143–151.

5. Gellert,M., Lipsett,M.N. and Davies,D.R. (1962) Helix formation by guanylic acid. *Proc. Natl. Acad. Sci. U. S. A.*, **48**, 2013–2018.

6. Sen,D. and Gilbert,W. (1998) Formation of parallel four-stranded complexes by guanine-rich motif for meiosis. *Nature*, **334**, 364–366.

7. Davis,J.T. (2004) G-quartets 40 years later: from 5′-GMP to molecular biology and supramolecular chemistry. *Angew. Chemie - Int. Ed.*, **43**, 668–698.

8. Williamson,J.R., Raghuraman,M.K. and Cech,T.R. (1989) Monovalent cation-induced structure of telomeric DNA: the G-quartet model. *Cell*, **59**, 871–880.

9. Burge,S., Parkinson,G.N., Hazel,P., Todd,A.K. and Neidle,S. (2006) Quadruplex DNA: sequence, topology and structure. *Nucleic Acids Res.*, **34**, 5402–5415.

10. Platella,C., Riccardi,C., Montesarchio,D., Roviello,G.N. and Musumeci,D. (2017) G-quadruplex-based aptamers against protein targets in therapy and diagnostics. *Biochim. Biophys. Acta - Gen. Subj.*, **1861**, 1429–1447.

11. Ma,Y., Iida,K. and Nagasawa,K. (2020) Topologies of G-quadruplex: biological

functions and regulation by ligands. *Biochem. Biophys. Res. Commun.*, **531**, 3–17.

12. Neidle,S. (2009) The structures of quadruplex nucleic acids and their drug complexes. *Curr. Opin. Struct. Biol.*, **19**, 239–250.

13. Reshetnikov,R. V, Kopylov,A.M. and Golovin,A. V (2010) Classification of G-quadruplex DNA on the basis of the quadruplex twist angle and planarity of G-Quartets. *Acta Naturae*, **2**, 72–81.

14. Phan,A.T. and Patel,D.J. (2003) Two-repeat human telomeric d(TAGGGTTAGGGT) sequence forms interconverting parallel and antiparallel G-Quadruplexes in solution: distinct topologies, thermodynamic properties, and folding/unfolding kinetics. *J. Am. Chem. Soc.*, **125**, 15021–15027.

15. Guédin,A., Gros,J., Alberti,P. and Mergny,J.L. (2010) How long is too long? Effects of loop size on G-quadruplex stability. *Nucleic Acids Res.*, **38**, 7858–7868.

16. Webba da Silva,M., Trajkovski,M., Sannohe,Y., Hessari,N.M. ani, Sugiyama,H. and Plavec,J. (2009) Design of a G-quadruplex topology through glycosidic bond angles. *Angew. Chemie - Int. Ed.*, **48**, 9167–9170.

17. Cang,X., Šponer,J. and Cheatham,T.E. (2011) Explaining the varied glycosidic conformational, G-tract length and sequence preferences for anti-parallel G-quadruplexes. *Nucleic Acids Res.*, **39**, 4499–4512.

18. Włodarczyk,A., Grzybowski,P., Patkowski,A. and Dobek,A. (2005) Effect of ions on the polymorphism, effective charge, and stability of human telomeric DNA. Photon correlation spectroscopy and circular dichroism studies. *J. Phys. Chem. B*, **109**, 3594–3605.

19. Largy,E., Marchand,A., Amrane,S., Gabelica,V. and Mergny,J.L. (2016) Quadruplex turncoats: cation-dependent folding and stability of quadruplex-

DNA double switches. *J. Am. Chem. Soc.*, **138**, 2780–2792.

20. Hardin,C.C., Perry,A.G. and White,K. (2000) Thermodynamic and kinetic characterization of the dissociation and assembly of quadruplex nucleic acids. *Biopolymers*, **56**, 147–194.

21. Lee,J.S. (1990) The stability of polypurine tetraplexes in the presence of mono- and divalent cations. *Nucleic Acids Res.*, **18**, 6057–6060.

22. Miyoshi,D., Nakao,A. and Sugimoto,N. (2003) Structural transition from antiparallel to parallel G-quadruplex of d(G4T4G4) induced by Ca2+. *Nucleic Acids Res.*, **31**, 1156–1163.

23. Fujii,T., Podbevšek,P., Plavec,J. and Sugimoto,N. (2017) Effects of metal ions and cosolutes on G-quadruplex topology. *J. Inorg. Biochem.*, **166**, 190–198.

24. Bhattacharyya,D., Arachchilage,G.M. and Basu,S. (2016) Metal cations in G-quadruplex folding and stability. *Front. Chem.*, **4**, 1–14.

25. Chaires,J.B. (2010) Human telomeric G-quadruplex: thermodynamic and kinetic studies of telomeric quadruplex stability. *FEBS J.*, **277**, 1098–1106.

26. Rigo,R., Palumbo,M. and Sissi,C. (2017) G-quadruplexes in human promoters: a challenge for therapeutic applications. *Biochim. Biophys. Acta - Gen. Subj.*, **1861**, 1399–1413.

27. Huppert,J.L. and Balasubramanian,S. (2005) Prevalence of quadruplexes in the human genome. *Nucleic Acids Res.*, **33**, 2908–2916.

28. Bedrat,A., Lacroix,L. and Mergny,J.L. (2016) Re-evaluation of G-quadruplex propensity with G4Hunter. *Nucleic Acids Res.*, **44**, 1746–1759.

29. Kikin,O., D'Antonio,L. and Bagga,P.S. (2006) QGRS Mapper: a web-based server for predicting G-quadruplexes in nucleotide sequences. *Nucleic Acids Res.*, **34**, 676–682.

30. Biffi,G., Tannahill,D., McCafferty,J.M. and Balasubramanian,S. (2013) Quantitative visualization of DNA G-quadruplex structures in human cells. *Nat. Chem.*, **5**, 182–186.

31. Moye,A.L., Porter,K.C., Cohen,S.B., Phan,T., Zyner,K.G., Sasaki,N., Lovrecz,G.O., Beck,J.L. and Bryan,T.M. (2015) Telomeric G-quadruplexes are a substrate and site of localization for human telomerase. *Nat. Commun.*, **6**, 1–12.

32. Torry,D.S. and Cooper,G.M. (1991) Proto-oncogenes in development and cancer. *Am. J. Reprod. Immunol.*, **25**, 129–132.

33. Brooks,T.A., Kendrick,S. and Hurley,L. (2010) Making sense of G-quadruplex and i-motif functions in oncogene promoters. *FEBS J.*, **277**, 3459–3469.

34. Balasubramanian,S., Hurley,L.H. and Nei (2011) Targeting G-quadruplexes in gene promoters: a novel anticancer strategy? *Nat. Rev. Drug. Discov.*, **10**, 261–275.

35. Fajkus,J., Sýkorová,E. and Leitch,A.R. (2005) Telomeres in evolution and evolution of telomeres. *Chromosom. Res.*, **13**, 469–479.

36. Griffith,J.D., Comeau,L., Rosenfield,S., Stansel,R.M., Bianchi,A., Moss,H. and De Lange,T. (1999) Mammalian telomeres end in a large duplex loop. *Cell*, **97**, 503–514.

37. Bailey,S.M. and Murnane,J.P. (2006) Telomeres, chromosome instability and cancer. *Nucleic Acids Res.*, **34**, 2408–2417.

38. Jafri,M.A., Ansari,S.A., Alqahtani,M.H. and Shay,J.W. (2016) Roles of telomeres and telomerase in cancer, and advances in telomerase-targeted therapies. *Genome Med.*, **8**, 1–18.

39. Cong,Y.-S., Wright,W.E. and Shay,J.W. (2002) Human telomerase and its

regulation. *Microbiol. Mol. Biol. Rev.*, **66**, 407–425.

40. Jäger,K. and Walter,M. (2016) Therapeutic targeting of telomerase. *Genes (Basel).*, **7**, 1–24.

41. Chilka,P., Desai,N. and Datta,B. (2019) Small molecule fluorescent probes for G-quadruplex visualization as potential cancer theranostic agents. *Molecules*, **24**, 1–15.

42. Pirota,V., Stasi,M., Benassi,A. and Doria,F. (2020) An overview of quadruplex ligands: their common features and chemotype diversity. *Annu. Rep. Med. Chem.*, **54**, 163–196.

43. Suss,O., Motiei,L. and Margulies,D. (2021) Broad applications of thiazole orange in fluorescent sensing of biomolecules and ions. *Molecules*, **26**, 1–25.

44. Hanczyc,P., Rajchel-Mieldzioć,P., Feng,B. and Fita,P. (2021) Identification of Thioflavin T binding modes to DNA: a structure-specific molecular probe for lasing applications. *J. Phys. Chem. Lett.*, **12**, 5436–5442.

45. Chen,X., Wang,J., Jiang,G., Zu,G., Liu,M., Zhou,L. and Pei,R. (2016) The development of a light-up red-emitting fluorescent probe based on a G-quadruplex specific cyanine dye. *RSC Adv.*, **6**, 70117–70123.

46. Lin,D., Fei,X., Gu,Y., Wang,C., Tang,Y., Li,R. and Zhou,J. (2015) A benzindole substituted carbazole cyanine dye: a novel targeting fluorescent probe for parallel c-myc G-quadruplexes. *Analyst*, **140**, 5772–5780.

47. Liu,L., Liu,W., Wang,K., Zhu,B., Xia,X., Ji,L. and Mao,Z. (2020) Quantitative detection of G-quadruplex DNA in live cells based on photon counts and complex structure discrimination. *Angew. Chemie*, **132**, 9806–9813.

48. Chen,S. Bin, Hu,M.H., Liu,G.C., Wang,J., Ou,T.M., Gu,L.Q., Huang,Z.S. and Tan,J.H. (2016) Visualization of NRAS RNA G-quadruplex structures in cells

with an engineered fluorogenic hybridization probe. *J. Am. Chem. Soc.*, **138**, 10382–10385.

49. Hu,M.H. and Chen,X. (2020) New fluorescent light-up quinoxalines differentiate between parallel and nonparallel G-quadruplex topologies using different excitation/emission channels. *Chem. Commun.*, **56**, 4168–4171.

50. Xie,X., Reznichenko,O., Chaput,L., Martin,P., Teulade-Fichou,M.P. and Granzhan,A. (2018) Topology-selective, fluorescent "Light-Up" probes for G-quadruplex DNA based on photoinduced electron transfer. *Chemistry.*, **24**, 12638–12651.

51. Chen,X.C., Chen,S. Bin, Dai,J., Yuan,J.H., Ou,T.M., Huang,Z.S. and Tan,J.H. (2018) Tracking the dynamic folding and unfolding of RNA G-quadruplexes in live cells. *Angew. Chemie - Int. Ed.*, **57**, 4702–4706.

52. Hestand,N.J. and Spano,F.C. (2018) Expanded theory of H- and J-molecular aggregates: the effects of vibronic coupling and intermolecular charge transfer. *Chem. Rev.*, **118**, 7069–7163.

53. Jiang,G., Chen,X., Xu,L., Cao,Y., Hong,S., Liu,M., Cao,W. and Pei,R. (2017) Design and synthesis of a dimethylindole red trimer: a new light-up red-emitting fluorescent probe for G-quadruplexes. *ChemistrySelect*, **2**, 2783–2788.

54. Gavathiotis,E., Heald,R.A., Stevens,M.F.G. and Searle,M.S. (2003) Drug recognition and stabilisation of the parallel-stranded DNA quadruplex d(TTAGGGT)4 containing the human telomeric repeat. *J. Mol. Biol.*, **334**, 25–36.

55. Salvati,E., Leonetti,C., Rizzo,A., Scarsella,M., Mottolese,M., Galati,R., Sperduti,I., Stevens,M.F.G., D'Incalci,M., Blasco,M., *et al.* (2007) Telomere damage induced by the G-quadruplex ligand RHPS4 has an antitumor effect. *J. Clin. Invest.*, **117**, 3236–3247.

56. Read,M., Harrison,R.J., Romagnoli,B., Tanious,F.A., Gowan,S.H., Reszka,A.P., Wilson,W.D., Kelland,L.R. and Neidle,S. (2001) Structure-based design of selective and potent G quadruplex-mediated telomerase inhibitors. *Proc. Natl. Acad. Sci. U. S. A.*, **98**, 4844–4849.

57. Ezzatizadeh,V., Mouro Pinto,R., Sandi,C., Sandi,M., Al-Mahdawi,S., te Riele,H. and A. Pook,M. (2009) Targeting human gastrointestinal stromal tumour cells with a quadruplex-binding small molecule. *J. Med. Chem.*, **52**, 3774–3783.

58. Doria,F., Nadai,M., Sattin,G., Pasotti,L., Richter,S.N. and Freccero,M. (2012) Water soluble extended naphthalene diimides as pH fluorescent sensors and G-quadruplex ligands. *Org. Biomol. Chem.*, **10**, 3830–3840.

59. Cuenca,F., Greciano,O., Gunaratnam,M., Haider,S., Munnur,D., Nanjunda,R., Wilson,W.D. and Neidle,S. (2008) Tri- and tetra-substituted naphthalene diimides as potent G-quadruplex ligands. *Bioorganic Med. Chem. Lett.*, **18**, 1668–1673.

60. Collie,G.W., Promontorio,R., Hampel,S.M., Micco,M., Neidle,S. and Parkinson,G.N. (2012) Structural basis for telomeric G-quadruplex targeting by naphthalene diimide ligands. *J. Am. Chem. Soc.*, **134**, 2723–2731.

61. Marchetti,C., Zyner,K.G., Ohnmacht,S.A., Robson,M., Haider,S.M., Morton,J.P., Marsico,G., Vo,T., Laughlin-Toth,S., Ahmed,A.A., *et al.* (2018) Targeting multiple effector pathways in pancreatic ductal adenocarcinoma with a G-quadruplex-binding small molecule. *J. Med. Chem.*, **61**, 2500–2517.

62. Köhler, G., Milstein,C. (1975) Continuous cultures of fused cells secreting antibody of predefined specificity. *Nature*, **256**, 495–497.

63. Ellington,A.D. and Szostak,J.W. (1990) In vitro selection of RNA molecules that bind specific ligands. *Nature*, **346**, 818–822.

64. Röthlisberger,P. and Hollenstein,M. (2018) Aptamer chemistry. *Adv. Drug Deliv.*

Rev., **134**, 3–21.

65. Adachi,T. and Nakamura,Y. (2019) Aptamers: a review of their chemical properties and modifications for therapeutic application. *Molecules*, **24**.

66. Odeh,F., Nsairat,H., Alshaer,W., Ismail,M.A., Esawi,E., Qaqish,B., Bawab,A. Al and Ismail,S.I. (2020) Aptamers chemistry: chemical modifications and conjugation strategies. *Molecules*, **25**, 1–51.

67. Ali,M.H., Elsherbiny,M.E. and Emara,M. (2019) Updates on aptamer research. *Int. J. Mol. Sci.*, **20**, 1–23.

68. Zhang,Y., Lai,B.S. and Juhas,M. (2019) Recent advances in aptamer discovery and applications. *Molecules*, **24**, 1–22.

69. Wang,T., Chen,C., Larcher,L.M., Barrero,R.A. and Veedu,R.N. (2019) Three decades of nucleic acid aptamer technologies: lessons learned, progress and opportunities on aptamer development. *Biotechnol. Adv.*, **37**, 28–50.

70. Chandola,C., Kalme,S., Casteleijn,M.G., Urtti,A. and Neerathilingam,M. (2016) Application of aptamers in diagnostics, drug-delivery and imaging. *J. Biosci.*, **41**, 535–561.

71. Musumeci,D., Platella,C., Riccardi,C., Moccia,F. and Montesarchio,D. (2017) Fluorescence sensing using DNA aptamers in cancer research and clinical diagnostics. *Cancers.*, **9**, 1–43.

72. Dhiman,A., Kalra,P., Bansal,V., Bruno,J.G. and Sharma,T.K. (2017) Aptamer-based point-of-care diagnostic platforms. *Sensors Actuators, B Chem.*, **246**, 535–553.

73. Hori,S.I., Herrera,A., Rossi,J.J. and Zhou,J. (2018) Current advances in aptamers for cancer diagnosis and therapy. *Cancers.*, **10**, 1–33.

74. Tuerk,C. and Gold,L. (1990) Systematic evolution of ligands by exponential

enrichment: RNA ligands to bacteriophage T4 DNA polymerase. *Science.*, **249**, 505–510.

75. Robertson,D.L. and Joyce,G.F. (1990) Selection in vitro of an RNA enzyme that specifically cleaves single-stranded DNA. *Nature*, **344**, 467–468.

76. Antipova,O.M., Zavyalova,E.G., Golovin,A. V., Pavlova,G. V., Kopylov,A.M. and Reshetnikov,R. V. (2018) Advances in the application of modified nucleotides in SELEX technology. *Biochem. (Mosc).*, **83**, 1161–1172.

77. Bayat,P., Nosrati,R., Alibolandi,M., Rafatpanah,H., Abnous,K., Khedri,M. and Ramezani,M. (2018) SELEX methods on the road to protein targeting with nucleic acid aptamers. *Biochimie*, **154**, 132–155.

78. Sola,M., Menon,A.P., Moreno,B., Meraviglia-Crivelli,D., Soldevilla,M.M., Cartón-García,F. and Pastor,F. (2020) Aptamers against live targets: is in vivo SELEX finally coming to the edge? *Mol. Ther. - Nucleic Acids*, **21**, 192–204.

79. Cruz-Toledo,J., McKeague,M., Zhang,X., Giamberardino,A., McConnell,E., Francis,T., DeRosa,M.C. and Dumontier,M. (2012) Aptamer base: a collaborative knowledge base to describe aptamers and SELEX experiments. *Database*, **2012**, 1–8.

80. Jellinek,D., Green,L.S., Bell,C. and Janjić,N. (1994) Inhibition of receptor binding by high-affinity RNA ligands to vascular endothelial growth factor. *Biochemistry*, **33**, 10450–10456.

81. Ambati,J., Ambati,B.K., Yoo,S.H., Ianchulev,S. and Adamis,A.P. (2003) Age-related macular degeneration: etiology, pathogenesis, and therapeutic strategies. *Surv. Ophthalmol.*, **48**, 257–293.

82. Que-Gewirth,N.S. and Sullenger,B.A. (2007) Gene therapy progress and prospects: RNA aptamers. *Gene Ther.*, **14**, 283–291.

83. Ruckman,J., Green,L.S., Beeson,J., Waugh,S., Gillette,W.L., Henninger,D.D., Claesson-Welsh,L. and Janjic,N. (1998) 2′-fluoropyrimidine RNA-based aptamers to the 165-amino acid form of vascular endothelial growth factor (VEGF165). *J. Biol. Chem.*, **273**, 20556–20567.

84. Ferrara,N. and Adamis,A.P. (2016) Ten years of anti-vascular endothelial growth factor therapy. *Nat. Rev. Drug Discov.*, **15**, 385–403.

85. Chakravarthy,U., Adamis,A., Cunningham,E.J., Goldbaum,M., Guyer,D., Katz,B. and Patel,M. (2006) Year 2 efficacy results of 2 randomized controlled clinical trials of pegaptanib for neovascular age-related macular degeneration. *Ophthalmology*, **113**, 1508.e1-1508.e25.

86. Ferrara,N., Hillan,K.J. and Novotny,W. (2005) Bevacizumab (Avastin), a humanized anti-VEGF monoclonal antibody for cancer therapy. *Biochem. Biophys. Res. Commun.*, **333**, 328–335.

87. Semeraro,F., Morescalchi,F., Duse,S., Parmeggiani,F., Gambicorti,E. and Costagliola,C. (2013) Aflibercept in wet AMD: specific role and optimal use. *Drug Des. Devel. Ther.*, **7**, 711–722.

88. Senger,D.R., Van De Water,L., Brown,L.F., Nagy,J.A., Yeo,K.T., Yeo,T.K., Berse,B., Jackman,R.W., Dvorak,A.M. and Dvorak,H.F. (1993) Vascular permeability factor (VPF, VEGF) in tumor biology. *Cancer Metastasis Rev.*, **12**, 303–324.

89. Dvorak,H.F. (2002) Vascular permeability factor/vascular endothelial growth factor: a critical cytokine in tumor angiogenesis and a potential target for diagnosis and therapy. *J. Clin. Oncol.*, **20**, 4368–4380.

90. Ferrara,N. and Kerbel,R.S. (2005) Angiogenesis as a therapeutic target. *Nature*, **438**, 967–974.

91. Berse,B., Brown,L.F., Van de Water,L., Dvorak,H.F. and Senger,D.R. (1992)

Vascular permeability factor (vascular endothelial growth factor) gene is expressed differentially in normal tissues, macrophages, and tumors. *Mol. Biol. Cell*, **3**, 211–220.

92. Breier,G., Albrecht,U., Sterrer,S. and Risau,W. (1992) Expression of vascular endothelial growth factor during embryonic angiogenesis and endothelial cell differentiation. *Development*, **114**, 521–532.

93. Shifren,J.L. (1994) In the human fetus, vascular endothelial growth factor is expressed in epithelial cells and myocytes, but not vascular endothelium: implications for mode of action. *J. Clin. Endocrinol. Metab.*, **79**, 316–322.

94. Apte,R.S., Chen,D.S. and Ferrara,N. (2019) VEGF in signaling and disease: beyond discovery and development. *Cell*, **176**, 1248–1264.

95. Kaelin,W.G. (2008) The von Hippel-Lindau tumour suppressor protein: O2 sensing and cancer. *Nat. Rev. Cancer*, **8**, 865–873.

96. Krock,B.L., Skuli,N. and Simon,M.C. (2011) Hypoxia-induced angiogenesis: good and evil. *Genes Cancer*, **2**, 1117–1133.

97. Houck,K.A., Ferrara,N., Winer,J., Cachianes,G., Li,B. and Leung,D.W. (1991) The vascular endothelial growth factor family: identification of a fourth molecular species and characterization of alternative splicing of RNA. *Mol. Endocrinol.*, **5**, 1806–1814.

98. Tischer,E., Mitchell,R., Hartman,T., Silva,M., Gospodarowicz,D., Fiddes,J.C. and Abraham,J.A. (1991) The human gene for vascular endothelial growth factor: multiple protein forms are encoded through alternative exon splicing. *J. Biol. Chem.*, **266**, 11947–11954.

99. Bernatchez,P.N., Soker,S. and Sirois,M.G. (1999) Vascular endothelial growth factor effect on endothelial cell proliferation, migration, and platelet-activating factor synthesis is Flk-1- dependent. *J. Biol. Chem.*, **274**, 31047–31054.

100. Olofsson,B., Pajusola,K., Kaipainen,A., Von Euler,G., Joukov,V., Saksela,O., Orpana,A., Pettersson,R.F., Alitalo,K. and Eriksson,U. (1996) Vascular endothelial growth factor B, a novel growth factor for endothelial cells. *Proc. Natl. Acad. Sci. U. S. A.*, **93**, 2576–2581.

101. Alitalo,K., Tammela,T. and Petrova,T. V. (2005) Lymphangiogenesis in development and human disease. *Nature*, **438**, 946–953.

102. Ogawa,S., Oku,A., Sawano,A., Yamaguchi,S., Yazaki,Y. and Shibuya,M. (1998) A novel type of vascular endothelial growth factor, VEGF-E (NZ-7 VEGF), preferentially utilizes KDR/Flk-1 receptor and carries a potent mitotic activity without heparin-binding domain. *J. Biol. Chem.*, **273**, 31273–31282.

103. Cao,Y., Chen,H., Zhou,L., Chiang,M.-K., Anand-Apte,B., Weatherbee,J.A., Wang,Y., Fang,F., Flanagan,J.G. and Tsang,M.L.-S. (1996) Heterodimers of placenta growth factor/vascular endothelial growth factor. *J. Biol. Chem.*, **271**, 3154–3162.

104. Wakelin,S.J., Marson,L., Howie,S.E.M., Garden,J., Lamb,J.R. and Forsythe,J.L.R. (2005) The role of vascular endothelial growth factor in the kidney in health and disease. *Nephron - Physiol.*, **25**, 111–118.

105. Koch,A.E., Harlow,L.A., Haines,G.K., Amento,E.P., Unemori,E.N., Wong,W.L., Pope,R.M. and Ferrara,N. (1994) Vascular endothelial growth factor. A cytokine modulating endothelial function in rheumatoid arthritis. *J. Immunol.*, **152**, 4149–4156.

106. Detmar,M., Brown,L.F., Claffey,K.P., Yeo,K.T., Kocher,O., Jackman,R.W., Berse,B. and Dvorak,H.F. (1994) Overexpression of vascular permeability factor/vascular endothelial growth factor and its receptors in psoriasis. *J. Exp. Med.*, **180**, 1141–1146.

107. Pietrowski,D., Szabo,L., Sator,M., Just,A. and Egarter,C. (2012) Ovarian

hyperstimulation syndrome is correlated with a reduction of soluble VEGF receptor protein level and a higher amount of VEGF-A. *Hum. Reprod.*, **27**, 196–199.

108. Jonas,J.B. and Neumaier,M. (2007) Vascular endothelial growth factor and basic fibroblast growth factor in exudative age-related macular degeneration and diffuse diabetic macular edema. *Ophthalmic Res.*, **39**, 139–142.

109. Nagy,J.A., Chang,S.H., Dvorak,A.M. and Dvorak,H.F. (2009) Why are tumour blood vessels abnormal and why is it important to know? *British. Journal. of Cancer.*, **100**, 865–869.

110. Frezzetti,D., Gallo,M., Maiello,M.R., D'Alessio,A., Esposito,C., Chicchinelli,N., Normanno,N. and De Luca,A. (2017) VEGF as a potential target in lung cancer. *Expert Opin. Ther. Targets*, **21**, 959–966.

111. Guo,P., Fang,Q., Tao,H.Q., Schafer,C.A., Fenton,B.M., Ding,I., Hu,B. and Cheng,S.Y. (2003) Overexpression of vascular endothelial growth factor by MCF-7 breast cancer cells promotes estrogen-independent tumor growth in vivo. *Cancer Res.*, **63**, 4684–4691.

112. Guidi,A.J., Abu-Jawdeh,G., Tognazzi,K., Dvorak,H.F. and Brown,L.F. (1993) Expression of vascular permeability factor (vascular endothelial growth factor) and its receptors in endometrial carcinoma. *Cancer*, **53**, 4727–4735.

113. Yamaguchi,R., Yano,H., Iemura,A., Ogasawara,S., Haramaki,M. and Kojiro,M. (1998) Expression of vascular endothelial growth factor in human hepatocellular carcinoma. *Hepatology*, **28**, 68–77.

114. Mukherjee,S., Pal,M., Mukhopadhyay,S., Das,I., Hazra,R., Ghosh,S., Mondal,R.K. and Bal,R. (2017) VEGF expression to support targeted therapy in ovarian surface epithelial neoplasms. *J. Clin. Diagnostic Res.*, **11**, 43–46.

115. Plate,K.H., Breier,G., Weich,H.A. and Risau,W. (1992) VEGF is a potential

tumour angiogenesis factor in human gliomas in vivo. *Nature*, **359**, 845–848.

116. Konno,H., Tanaka,T., Baba,M., Kanai,T., Matsumoto,K., Kamiya,K., Nakamura,S. and Baba,S. (1998) Quantitative analysis of vascular endothelial growth factor in colon cancer. *Eur. Surg. Res.*, **30**, 273–278.

117. Tawada,K., Ishihara,T., Kobayashi,A., Yamaguchi,T., Tsuyuguchi,T., Matsuyama,M. and Yokosuka,O. (2008) Quantitative analysis of vascular endothelial growth factor in liver metastases from pancreatic carcinoma as a predictor of chemotherapeutic effect and prognosis. *Clin. Cancer Res.*, **14**, 7438–7443.

118. Catena,R., Muniz-Medina,V., Moralejo,B., Javierre,B., Best,C.J.M., Emmert-Buck,M.R., Green,J.E., Baker,C.C. and Calvo,A. (2007) Increased expression of VEGF121/VEGF165-189 ratio results in a significant enhancement of human prostate tumor angiogenesis. *Int. J. Cancer*, **120**, 2096–2109.

119. Keyt,B.A., Nguyen,H. V, Berleau,L.T., Duarte,C.M., Park,J., Chen,H. and Ferrara,N. (1996) Identification of vascular endothelial growth factor determinants for binding KDR and FLT-1 receptors. Generation of receptor-selective VEGF variants by site-directed mutagenesis. *J. Biol. Chem.*, **271**, 5638–5646.

120. Riccardi,C., Napolitano,E., Platella,C., Musumeci,D. and Montesarchio,D. (2020) Anti-VEGF DNA-based aptamers in cancer therapeutics and diagnostics. *Med. Res. Rev.*, **41**, 464–506.

121. Meadows,K.L. and Hurwitz,H.I. (2012) Anti-VEGF therapies in the clinic. *Cold Spring Harb. Perspect. Med.*, **2**, 1–27.

122. Kong,D., Kim,M.R., Jang,J.H., Na,H. and Lee,S. (2017) A Review of anti-angiogenic targets for monoclonal antibody cancer therapy. *Int. J. Mol. Sci.*, **18**, 1–25.

123. Platella,C., Riccardi,C., Montesarchio,D., Roviello,G.N. and Musumeci,D. (2017) G-quadruplex-based aptamers against protein targets in therapy and diagnostics. *Biochim. Biophys. Acta*, **1861**, 1429–1447.

124. Nonaka,Y., Sode,K. and Ikebukuro,K. (2010) Screening and improvement of an anti-VEGF DNA aptamer. *Molecules*, **15**, 215–225.

125. Nonaka,Y., Yoshida,W., Abe,K., Ferri,S., Schulze,H., Bachmann,T.T. and Ikebukuro,K. (2013) Affinity improvement of a VEGF aptamer by in silico maturation for a sensitive VEGF-detection system. *Anal. Chem.*, **85**, 1132–1137.

126. Moccia,F., Riccardi,C., Musumeci,D., Leone,S., Oliva,R., Petraccone,L. and Montesarchio,D. (2019) Insights into the G-rich VEGF-binding aptamer V7t1: when two G-quadruplexes are better than one! *Nucleic Acids Res.*, **47**, 8318–8331.

127. Riccardi,C., Napolitano,E., Musumeci,D. and Montesarchio,D. (2020) Dimeric and multimeric DNA aptamers for highly effective protein recognition. *Molecules*, **25**, 7–15.

128. Bustin,M. (1999) Regulation of DNA-dependent activities by the functional motifs of the high-mobility-group chromosomal proteins. *Mol. Cell. Biol.*, **19**, 5237–5246.

129. Goodwin,G.H., Sanders,C. and Johns,E.W. (1973) A new group of chromatin-associated proteins with a high content of acidic and basic amino acids. *Eur. J. Biochem.*, **38**, 14–19.

130. Müller,S., Scaffidi,P., Degryse,B., Bonaldi,T., Ronfani,L., Agresti,A., Beltrame,M. and Bianchi,M.E. (2001) The double life of HMGB1 chromatin protein: architectural factor and extracellular signal. *EMBO J.*, **20**, 4337–4340.

131. Thomas,J.O. (2001) HMG1 and 2: “architectural” DNA-binding proteins. *Biochem. Soc. Trans.*, **29**, 395–401.

132. Read,C.M., Cary,P.D., Crane-robinson,C., Driscoll,P.C. and Norman,D.G. (1993) Solution structure of a DNA-binding domain from HMG1. *Nucleic Acids Res.*, **21**, 3427–3436.

133. Weir,H.M., Kraulis,P.J., Hill,C.S., Raine,A.R.C., Laue,E.D. and Thomas,J.O. (1993) Structure of the HMG box motif in the B-domain of HMG1. *EMBO J.*, **12**, 1311–1319.

134. Musumeci,D., Roviello,G.N. and Montesarchio,D. (2014) An overview on HMGB1 inhibitors as potential therapeutic agents in HMGB1-related pathologies. *Pharmacol. Ther.*, **141**, 347–357.

135. Hardman,C.H., William Broadhurst,R., Raine,A.R.C., Grasser,K.D., Thomas,J.O. and Laue,E.D. (1995) Structure of the A-Domain of HMG1 and its interaction with DNA as studied by heteronuclear three- and four-dimensional NMR spectroscopy. *Biochemistry*, **34**, 16596–16607.

136. Wang,Q., Zeng,M., Wang,W. and Tang,J. (2007) The HMGB1 acidic tail regulates HMGB1 DNA binding specificity by a unique mechanism. *Biochem. Biophys. Res. Commun.*, **360**, 14–19.

137. Walker,J.M., Gooderham,K., Hastings,J.R.B., Mayes,E. and Johns,E.W. (1980) The primary structures of non-histone chromosomal proteins HMG 1 and 2. *FEBS Lett.*, **122**, 264–270.

138. Bustin,M., A. Lehn,D. and Landsman,D. (1990) Structural features of the HMG chromosomal proteins and their genes. *Biochim. Biophys. Acta,* **1049**, 231–243.

139. Yotov,W. V and St-Arnaud,R. (1992) Nucleotide sequence of a mouse cDNA encoding the non-histone chromosomal high mobility group protein-1 (HMG1). *Nucleic Acids Res.*, **20**, 3516.

140. Paull,T.T., Haykinson,M.J. and Johnson,R.C. (1993) The nonspecific DNA-binding and -bending proteins HMG1 and HMG2 promote the assembly of

complex nucleoprotein structures. *Genes Dev.*, **7**, 1521–1534.

141. Pasheva,E.A., Pashev,I.G. and Favre,A. (1998) Preferential binding of high mobility group 1 protein to UV-damaged DNA: role of the COOH-terminal domain. *J. Biol. Chem.*, **273**, 24730–24736.

142. Bianchi,M.E., Beltrame,M. and Paonessa,G. (1989) Specific recognition of cruciform DNA by nuclear protein HMG1. *Science.*, **243**, 1056–1059.

143. Pil,P.M. and Lippard,S.J. (1992) Specific binding of chromosomal protein HMG1 to DNA damaged by the anticancer drug cisplatin. *Science.*, **256**, 234–237.

144. Topalova,D., Ugrinova,I., Pashev,I.G. and Pasheva,E.A. (2008) HMGB1 protein inhibits DNA replication in vitro: a role of the acetylation and the acidic tail. *Int. J. Biochem. Cell Biol.*, **40**, 1536–1542.

145. Bonaldi,T., Längst,G., Strohner,R., Becker,P.B. and Bianchi,M.E. (2002) The DNA chaperone HMGB1 facilitates ACF/CHRAC-dependent nucleosome sliding. *EMBO J.*, **21**, 6865–6873.

146. Ugrinova,I., Pashev,I.G. and Pasheva,E.A. (2009) Nucleosome binding properties and co-remodeling activities of native and in vivo acetylated HMGB-1 and HMGB-2 proteins. *Biochemistry*, **48**, 6502–6507.

147. Ugrinova,I., Zlateva,S., Pashev,I.G. and Pasheva,E.A. (2009) Native HMGB1 protein inhibits repair of cisplatin-damaged nucleosomes in vitro. *Int. J. Biochem. Cell Biol.*, **41**, 1556–1562.

148. Scaffidi,P., Misteli,T. and Bianchi,M.E. (2002) Release of chromatin protein HMGB1 by necrotic cells triggers inflammation. *Nature*, **418**, 191–195.

149. Li,G., Liang,X. and Lotze,M.T. (2013) HMGB1: the central cytokine for all lymphoid cells. *Front. Immunol.*, **4**, 1–9.

150. Dumitriu,I.E., Baruah,P., Valentinis,B., Voll,R.E., Herrmann,M., Nawroth,P.P., Arnold,B., Bianchi,M.E., Manfredi,A.A. and Rovere-Querini,P. (2005) Release of high mobility group box 1 by dendritic cells controls T cell activation via the receptor for advanced glycation end products. *J. Immunol.*, **174**, 7506–7515.

151. Palumbo,R., De Marchis,F., Pusterla,T., Conti,A., Alessio,M. and Bianchi,M.E. (2009) Src family kinases are necessary for cell migration induced by extracellular HMGB1. *J. Leukoc. Biol.*, **86**, 617–623.

152. Stilhano,R.S., Costa,A.J., Nishino,M.S., Shams,S., Bartolomeo,C.S., Breithaupt-Faloppa,A.C., Silva,E.A., Ramirez,A.L., Prado,C.M. and Ureshino,R.P. (2020) SARS-CoV-2 and the possible connection to ERs, ACE2, and RAGE: focus on susceptibility factors. *FASEB J.*, **34**, 14103–14119.

153. Freeman,T.L. and Swartz,T.H. (2020) Targeting the NLRP3 Inflammasome in Severe COVID-19. *Front. Immunol.*, **11**, 1–12.

154. Kerkeni,M. and Gharbi,J. (2020) RAGE receptor: may be a potential inflammatory mediator for SARS-COV-2 infection? *Med. Hypotheses*, **144**, 1–2.

155. Vogel,S., Bodenstein,R., Chen,Q., Feil,S., Feil,R., Rheinlaender,J., Schäffer,T.E., Bohn,E., Frick,J.S., Borst,O., *et al.* (2015) Platelet-derived HMGB1 is a critical mediator of thrombosis. *J. Clin. Invest.*, **125**, 4638–4654.

156. Lupu,L., Palmer,A. and Huber-lang,M. (2020) Inflammation , thrombosis , and destruction : the three-headed cerberus of trauma- and SARS-CoV-2-induced ARDS. *Front. Immunol.*, **11**, 1–11.

157. Al-kuraishy,H.M., Al-Gareeb,A.I., Alkazmi,L., Habotta,O.A. and Batiha,G.E.S. (2022) High-mobility group box 1 (HMGB1) in COVID-19: extrapolation of dangerous liaisons. *Inflammopharmacology*, **30**, 811–820.

158. Koch,M., Chitayat,S., Dattilo,B.M., Schiefner,A., Diez,J., Chazin,W.J. and

Fritz,G. (2010) Structural basis for ligand recognition and activation of RAGE. *Structure*, **18**, 1342–1352.

159. Park,H.J. and Boyington,J.C. (2010) The 1.5 Å crystal structure of human receptor for advanced glycation endproducts (RAGE) ectodomains reveals unique features determining ligand binding. *J. Biol. Chem.*, **285**, 40762–40770.

160. Borsi,V., Cerofolini,L., Fragai,M. and Luchinat,C. (2012) NMR characterization of the C-terminal tail of full-length RAGE in a membrane mimicking environment. *J. Biomol. NMR*, **54**, 285–290.

161. Brett,J., Schmidt,A.M., Shi Du Yan, Yu Shan Zou, Weidman,E., Pinsky,D., Nowygrod,R., Neeper,M., Przysiecki,C., Shaw,A., *et al.* (1993) Survey of the distribution of a newly characterized receptor for advanced glycation end products in tissues. *Am. J. Pathol.*, **143**, 1699–1712.

162. Huttunen,H.J., Fages,C. and Rauvala,H. (1999) Receptor for advanced glycation end products (RAGE)-mediated neurite outgrowth and activation of NF-κB require the cytoplasmic domain of the receptor but different downstream signaling pathways. *J. Biol. Chem.*, **274**, 19919–19924.

163. Schmidt,A.M., Yan,S. Du, Yan,S.F. and Stern,D.M. (2001) The multiligand receptor RAGE as a progression factor amplifying immune and inflammatory responses. *J. Clin. Invest.*, **108**, 949–955.

164. Li,J., Qu,X. and Schmidt,A.M. (1998) Sp1-binding elements in the promoter of RAGE are essential for amphoterin-mediated gene expression in cultured neuroblastoma cells. *J. Biol. Chem.*, **273**, 30870–30878.

165. Sárkány,Z., Ikonen,T.P., Ferreira-da-Silva,F., Saraiva,M.J., Svergun,D. and Damas,A.M. (2011) Solution structure of the soluble receptor for advanced glycation end products (sRAGE). *J. Biol. Chem.*, **286**, 37525–37534.

166. Bierhaus,A., Humpert,P.M., Morcos,M., Wendt,T., Chavakis,T., Arnold,B.,

Stern,D.M. and Nawroth,P.P. (2005) Understanding RAGE, the receptor for advanced glycation end products. *J. Mol. Med.*, **83**, 876–886.

167. Ostendorp,T., Leclerc,E., Galichet,A., Koch,M., Demling,N., Weigle,B., Heizmann,C.W., Kroneck,P.M.H. and Fritz,G. (2007) Structural and functional insights into RAGE activation by multimeric S100B. *EMBO J.*, **26**, 3868–3878.

168. Kokkola,R., Andersson,Å., Mullins,G., Östberg,T., Treutiger,C.J., Arnold,B., Nawroth,P., Andersson,U., Harris,R.A. and Harris,H.E. (2005) RAGE is the major receptor for the proinflammatory activity of HMGB1 in rodent macrophages. *Scand. J. Immunol.*, **61**, 1–9.

169. Liliensiek,B., Weigand,M.A., Bierhaus,A., Nicklas,W., Kasper,M., Hofer,S., Plachky,J., Gröne,H.J., Kurschus,F.C., Schmidt,A.M., *et al.* (2004) Receptor for advanced glycation end products (RAGE) regulates sepsis but not the adaptive immune response. *J. Clin. Invest.*, **113**, 1641–1650.

170. Yang,H., Ochani,M., Li,J., Qiang,X., Tanovic,M., Harris,H.E., Susarla,S.M., Ulloa,L., Wang,H., DiRaimo,R., *et al.* (2004) Reversing established sepsis with antagonists of endogenous high-mobility group box 1. *Proc. Natl. Acad. Sci. U. S. A.*, **101**, 296–301.

171. Lutterloh,E.C., Opal,S.M., Pittman,D.D., Keith,J.C., Tan,X.Y., Clancy,B.M., Palmer,H., Milarski,K., Sun,Y., Palardy,J.E., *et al.* (2007) Inhibition of the RAGE products increases survival in experimental models of severe sepsis and systemic infection. *Crit. Care*, **11**, 1–9.

172. Logsdon,C., Fuentes,M., Huang,E. and Arumugam,T. (2007) RAGE and RAGE ligands in cancer. *Curr. Mol. Med.*, **7**, 777–789.

173. Sparvero,L.J., Asafu-Adjei,D., Kang,R., Tang,D., Amin,N., Im,J., Rutledge,R., Lin,B., Amoscato,A.A., Zeh,H.J., *et al.* (2009) RAGE (receptor for advanced glycation endproducts), RAGE ligands, and their role in cancer and

inflammation. *J. Transl. Med.*, **7**, 1–21.

174. Han,S.H., Kim,Y.H. and Mook-Jung,I. (2011) RAGE: the beneficial and deleterious effects by diverse mechanisms of actions. *Mol. Cells*, **31**, 91–97.

175. Todorova,J. and Pasheva,E. (2012) High mobility group B1 protein interacts with its receptor RAGE in tumor cells but not in normal tissues. *Oncol. Lett.*, **3**, 214–218.

176. Yang,H., Wang,H., Levine,Y.A., Gunasekaran,M.K., Wang,Y., Addorisio,M., Zhu,S., Li,W., Li,J., de Kleijn,D.P.V., *et al.* (2016) Identification of CD163 as an antiinflammatory receptor for HMGB1-haptoglobin complexes. *JCI Insight*, **1**, 1–15.

177. Abeyama,K., Stern,D.M., Ito,Y., Kawahara,K.I., Yoshimoto,Y., Tanaka,M., Uchimura,T., Ida,N., Yamazaki,Y., Yamada,S., *et al.* (2005) The N-terminal domain of thrombomodulin sequesters high-mobility group-B1 protein, a novel antiinflammatory mechanism. *J. Clin. Invest.*, **115**, 1267–1274.

178. Ito,T., Kawahara,K.I., Okamoto,K., Yamada,S., Yasuda,M., Imaizumi,H., Nawa,Y., Meng,X., Shrestha,B., Hashiguchi,T., *et al.* (2008) Proteolytic cleavage of high mobility group box 1 protein by thrombin-thrombomodulin complexes. *Arterioscler. Thromb. Vasc. Biol.*, **28**, 1825–1830.

179. Venereau,E., De Leo,F., Mezzapelle,R., Careccia,G., Musco,G. and Bianchi,M.E. (2016) HMGB1 as biomarker and drug target. *Pharmacol. Res.*, **111**, 534–544.

180. Benoit,M.E., Clarke,E. V., Morgado,P., Fraser,D.A. and Tenner,A.J. (2012) Complement protein C1q directs macrophage polarization and limits inflammasome activity during the uptake of apoptotic cells. *J. Immunol.*, **188**, 5682–5693.

181. Son,M., Porat,A., He,M., Suurmond,J., Santiago-Schwarz,F., Andersson,U.,

Coleman,T.R., Volpe,B.T., Tracey,K.J., Al-Abed,Y., *et al.* (2016) C1q and HMGB1 reciprocally regulate human macrophage polarization. *Blood*, **128**, 2218–2228.

182. Barnay-Verdier,S., Fattoum,L., Borde,C., Kaveri,S., Gibot,S. and Maréchal,V. (2011) Emergence of autoantibodies to HMGB1 is associated with survival in patients with septic shock. *Intensive Care Med.*, **37**, 957–962.

183. Mollica,L., De Marchis,F., Spitaleri,A., Dallacosta,C., Pennacchini,D., Zamai,M., Agresti,A., Trisciuoglio,L., Musco,G. and Bianchi,M.E. (2007) Glycyrrhizin binds to high-mobility group box 1 protein and inhibits its cytokine activities. *Chem. Biol.*, **14**, 431–441.

184. Vanpatten,S. and Al-Abed,Y. (2018) High Mobility Group Box-1 (HMGb1): current wisdom and advancement as a potential drug target. *J. Med. Chem.*, **61**, 5093–5107.

185. Bucci,E.M., Valente,M., Musumeci,D., Sapio,R., Anrò,V., Roviello,G.N. and Moccia,M. (2007) ODN-based drugs for targeting of extracellular proteins. *Nucleosides. Nucleotides Nucleic Acids*, **26**, 1047–1050.

186. Musumeci,D., Bucci,E.M., Roviello,G.N., Sapio,R., Valente,M., Moccia,M., Bianchi,M.E. and Pedone,C. (2011) DNA-based strategies for blocking HMGB1 cytokine activity: design, synthesis and preliminary in vitro/in vivo assays of DNA and DNA-like duplexes. *Mol. Biosyst.*, **7**, 1742–1752.

187. Musumeci,D., Roviello,G.N., Montesarchio,D., Sapio,R., Valente,M., Anrò,V. and Bucci,E.M. (2013) Hairpin ODN-based ligands as potential inhibitors of HMGB1 cytokine activity. *RSC Adv.*, **3**, 12176–12184.

188. Napoli,L. De, Messere,A., Montesarchio,D. and Pepe,A. (1997) Synthesis and triple helix formation by alternate strand recognition of oligonucleotides containing 3′-3′ phosphodiester bonds. *J. Org. Chem.*, **62**, 9024–9030.

189. De Napoli,L., Di Fabio,G., Messere,A., Montesarchio,D., Musumeci,D. and Piccialli,G. (1999) Synthesis and characterization of new 3′-3′ linked oligodeoxyribonucleotides for alternate strand triple helix formation. *Tetrahedron*, **55**, 9899–9914.

190. Oliviero,G., Borbone,N., Galeone,A., Varra,M., Piccialli,G. and Mayol,L. (2004) Synthesis and characterization of a bunchy oligonucleotide forming a monomolecular parallel quadruplex structure in solution. *Tetrahedron Lett.*, **45**, 4869–4872.

191. Moggio,L., Napoli,L. De, Blasio,B. Di, Fabio,G. Di, Onofrio,J.D., Montesarchio,D. and Messere,A. (2006) Solid-phase synthesis of cyclic PNA and PNA − DNA chimeras. *Org. Lett.*, **8**, 2015–2018.

192. Pagano,B., Margarucci,L., Zizza,P., Amato,J., Iaccarino,N., Cassiano,C., Salvati,E., Novellino,E., Biroccio,A., Casapullo,A., *et al.* (2015) Identification of novel interactors of human telomeric G-quadruplex DNA. *Chem. Commun.*, **51**, 2964–2967.

193. Amato,J., Madanayake,T.W., Iaccarino,N., Novellino,E., Randazzo,A., Hurley,L.H. and Pagano,B. (2018) HMGB1 binds to the KRAS promoter G-quadruplex: a new player in oncogene transcriptional regulation? *Chem. Commun.*, **54**, 9442–9445.

194. Sung,H., Ferlay,J., Siegel,R.L., Laversanne,M., Soerjomataram,I., Jemal,A. and Bray,F. (2021) Global Cancer Statistics 2020 : GLOBOCAN estimates of incidence and mortality worldwide for 36 cancers in 185 countries. *CA. Cancer J. Clin.*, **71**, 209–249.

195. Hackshaw,A., Clarke,C.A. and Hartman,A. (2022) New genomic technologies for multi-cancer early detection : rethinking the scope of cancer screening. *Cancer Cell*, **40**, 109–113.

196. Melincovici,C.S., Boşca,A.B., Şuşman,S., Mărginean,M., Mihu,C., Istrate,M., Moldovan,I.M., Roman,A.L. and Mihu,C.M. (2018) Vascular endothelial growth factor (VEGF) – key factor in normal and pathological angiogenesis. *Rom. J. Morphol. Embryol.*, **59**, 455–467.

197. Medford,A.R.L., Douglas,S.K., Godinho,S.I.H., Uppington,K.M., Armstrong,L., Gillespie,K.M., van Zyl,B., Tetley,T.D., Ibrahim,N.B.N. and Millar,A.B. (2009) Vascular Endothelial Growth Factor (VEGF) isoform expression and activity in human and murine lung injury. *Respir. Res.*, **10**, 1–12.

198. Riccardi,C., Musumeci,D., Platella,C., Gaglione,R., Arciello,A. and Montesarchio,D. (2020) Tuning the polymorphism of the anti-VEGF G-rich V7t1 aptamer by covalent dimeric constructs. *Int. J. Mol. Sci.*, **21**, 1–24.

199. Sun,Z.Y., Wang,X.N., Cheng,S.Q., Su,X.X. and Ou,T.M. (2019) Developing novel G-quadruplex ligands: from interaction with nucleic acids to interfering with nucleic acid–protein interaction. *Molecules*, **24**, 396.

200. Umar,M.I., Ji,D., Chan,C.Y. and Kwok,C.K. (2019) G-quadruplex-based fluorescent turn-on ligands and aptamers: from development to applications. *Molecules*, **24**, 2416.

201. Kumar,R., Chand,K., Bhowmik,S., Das,R.N., Bhattacharjee,S., Hedenström,M., Hedenström,H. and Chorell,E. (2020) Subtle structural alterations in G-quadruplex DNA regulate site specificity of fluorescence light-up probes. *Nucleic Acids Res.*, **48**, 1108–1119.

202. Chen,X., Wang,J., Jiang,G., Zu,G., Liu,M., Zhou,L. and Pei,R. (2016) The development of a light-up red-emitting fluorescent probe based on a G-quadruplex specific cyanine dye. *RSC Adv.*, **6**, 70117–70123.

203. Ihmels,H., Jiang,S., Mahmoud,M.M.A., Schönherr,H., Wesner,D. and Zamrik,I. (2018) Fluorimetric detection of G-quadruplex DNA in solution and adsorbed

on surfaces with a selective trinuclear cyanine dye. *Langmuir*, **34**, 11866–11877.

204. Wang,Y.Q., Hu,M.H., Guo,R.J., Chen,S. Bin, Huang,Z.S. and Tan,J.H. (2018) Tuning the selectivity of a commercial cyanine nucleic acid dye for preferential sensing of hybrid telomeric G-quadruplex DNA. *Sens. Actuators B Chem.*, **266**, 187–194.

205. Zhao,Z., Cao,S., Li,H., Li,D., He,Y., Wang,X., Chen,J., Zhang,S., Xu,J. and Knutson,J.R. (2022) Ultrafast excited-state dynamics of thiazole orange. *Chem. Phys.*, **553**, 1–16.

206. Largy,E., Hamon,F. and Teulade-Fichou,M.P. (2011) Development of a high-throughput G4-FID assay for screening and evaluation of small molecules binding quadruplex nucleic acid structures. *Anal. Bioanal. Chem.*, **400**, 3419–3427.

207. Biancardi,A., Biver,T., Marini,A., Mennucci,B. and Secco,F. (2011) Thiazole orange (TO) as a light-switch probe: combined quantum-mechanical and spectroscopic study. *Phys. Chem. Chem. Phys.*, **13**, 12595–12602.

208. Owens,E.A., Huynh,H.T., Stroeva,E.M., Barman,A., Ziabrev,K., Paul,A., Nguyen,S. V., Laramie,M., Hamelberg,D., Germann,M.W., *et al.* (2019) Second generation G-quadruplex stabilizing trimethine cyanines. *Bioconjugate Chem.*, **30**, 2647–2663.

209. Menacher,F., Rubner,M., Berndl,S., Wagenknecht,H. and Uni,V. (2008) Thiazole orange and Cy3: improvement of fluorescent DNA probes with use of short range electron transfer. *J. Org. Chem.*

210. Napolitano,E., Riccardi,C., Gaglione,R., Arciello,A., Pirota,V., Triveri,A., Doria,F., Musumeci,D. and Montesarchio,D. (2023) Selective light-up of dimeric G-quadruplex forming aptamers for efficient VEGF165 detection. *Int. J. Biol. Macromol.*, **224**, 344–357.

211. Stadler,A.L., Delos Santos,J.O., Stensrud,E.S., Dembska,A., Silva,G.L., Liu,S., Shank,N.I., Kunttas-Tatli,E., Sobers,C.J., Gramlich,P.M.E., *et al.* (2011) Fluorescent DNA nanotags featuring covalently attached intercalating dyes: synthesis, antibody conjugation, and intracellular imaging. *Bioconjugate Chem.*, **22**, 1491–1502.

212. Giancola,C. and Pagano,B. (2013) Energetics of ligand binding to G-quadruplexes. *Top. Curr. Chem.*, **330**, 211–242.

213. Wang,M.Q., Xu,J., Zhang,L., Liao,Y., Wei,H., Yin,Y.Y., Liu,Q. and Zhang,Y. (2019) Tuning the selectivity of N-alkylated styrylquinolinium dyes for sensing of G-quadruplex DNA. *Bioorg. Med. Chem.*, **27**, 552–559.

214. Nygren,J., Svanvik,N. and Kubista,M. (1998) The interactions between the fluorescent dye thiazole orange and DNA. *Biopolymers*, **46**, 39–51.

215. Guo,R.J., Yan,J.W., Chen,S. Bin, Gu,L.Q., Huang,Z.S. and Tan,J.H. (2016) A simple structural modification to thiazole orange to improve the selective detection of G-quadruplexes. *Dye. Pigm.*, **126**, 76–85.

216. Guan,A.J., Zhang,X.F., Sun,X., Li,Q., Xiang,J.F., Wang,L.X., Lan,L., Yang,F.M., Xu,S.J., Guo,X.M., *et al.* (2018) Ethyl-substitutive Thioflavin T as a highly-specific fluorescence probe for detecting G-quadruplex structure. *Sci. Rep.*, **8**, 1–12.

217. Verma,S., Ghuge,S.A., Ravichandiran,V. and Ranjan,N. (2019) Spectroscopic studies of Thioflavin-T binding to c-Myc G-quadruplex DNA. *Spectrochim. Acta - Part A Mol. Biomol. Spectrosc.*, **212**, 388–395.

218. Doria,F., Manet,I., Grande,V., Monti,S. and Freccero,M. (2013) Water-soluble naphthalene diimides as singlet oxygen sensitizers. *J. Org. Chem.*, **78**, 8065–8073.

219. Vummidi,B.R., Alzeer,J. and Luedtke,N.W. (2013) Fluorescent probes for G-

quadruplex structures. *ChemBioChem*, **14**, 540–558.

220. Mohanty,J., Barooah,N., Dhamodharan,V., Harikrishna,S., Pradeepkumar,P.I. and Bhasikuttan,A.C. (2013) Thioflavin T as an efficient inducer and selective fluorescent sensor for the human telomeric G-quadruplex DNA. *J. Am. Chem. Soc.*, **135**, 367–376.

221. Gabelica,V., Maeda,R., Fujimoto,T., Yaku,H., Murashima,T., Sugimoto,N. and Miyoshi,D. (2013) Multiple and cooperative binding of fluorescence light-up probe thioflavin T with human telomere DNA G-quadruplex. *Biochemistry*, **52**, 5620–5628.

222. De La Faverie,A.R., Guédin,A., Bedrat,A., Yatsunyk,L.A. and Mergny,J.L. (2014) Thioflavin T as a fluorescence light-up probe for G4 formation. *Nucleic Acids Res.*, **42**, 1–8.

223. Livendahl,M., Jamroskovic,J., Ivanova,S., Demirel,P., Sabouri,N. and Chorell,E. (2016) Design and synthesis of 2,2′-diindolylmethanes to selectively target certain G-quadruplex DNA structures. *Chem.Eur.J.*, **22**, 13004–13009.

224. Jamroskovic,J., Livendahl,M., Eriksson,J., Chorell,E. and Sabouri,N. (2016) Identification of compounds that selectively stabilize specific G-quadruplex structures by using a thioflavin T-displacement assay as a tool. *Chem.Eur.J.*, **22**, 18932–18943.

225. Karsisiotis,A.I., Hessari,N.M.A., Novellino,E., Spada,G.P., Randazzo,A. and Webba Da Silva,M. (2011) Topological characterization of nucleic acid G-quadruplexes by UV absorption and circular dichroism. *Angew. Chemie - Int. Ed.*, **50**, 10645–10648.

226. Ihmels,H., Mahmoud,M.M.A. and Patrick,B.O. (2017) Optical differentiation between quadruplex DNA and duplex DNA with a [2.2.2]heptamethinecyanine dye. *J. Phys. Org. Chem.*, **30**, 1–9.

227. Wang,Z., Li,M., Chen,W., Hsu,S.D. and Chang,T. (2016) A novel transition pathway of ligand-induced topological conversion from hybrid forms to parallel forms of human telomeric G-quadruplexes. *Nucleic Acids Res.*, **44**, 3958–3968.

228. Trizna,L., Janovec,L., Halaganová,A. and Víglaský,V. (2021) Rhodamine 6g-ligand influencing G-quadruplex stability and topology. *Int. J. Mol. Sci.*, **22**, 1–15.

229. Demkovičová,E., Bauer,Ľ., Krafčíková,P., Tlučková,K., Tóthova,P., Halaganová,A., Valušová,E. and Víglaský,V. (2017) Telomeric G-quadruplexes: from human to tetrahymena repeats. *J. Nucleic Acids*, **2017**.

230. Mikulin,I., Ljubić,I., Piantanida,I., Vasilev,A., Mondeshki,M., Kandinska,M., Uzelac,L., Martin-Kleiner,I., Kralj,M. and Tumir,L.M. (2021) Polycationic monomeric and homodimeric asymmetric monomethine cyanine dyes with hydroxypropyl functionality—strong affinity nucleic acids binders. *Biomolecules*, **11**, 1–20.

231. Garoff,R.A., Litzinger,E.A., Connor,R.E., Fishman,I. and Armitage,B.A. (2002) Helical aggregation of cyanine dyes on DNA templates: effect of dye structure on formation of homo- and heteroaggregates. *Langmuir*, **18**, 6330–6337.

232. del Villar-Guerra,R., Trent,J.O. and Chaires,J.B. (2018) G-Quadruplex secondary structure sbtained from circular dichroism spectroscopy. *Angew. Chemie - Int. Ed.*, **57**, 7171–7175.

233. Hellman,L.M. and Fried,M.G. (2007) Electrophoretic mobility shift assay (EMSA) for detecting protein-nucleic acid interactions. *Nat. Protoc.*, **2**, 1849–1861.

234. Dhami,S., Mello,A.J.D., Rumbles,G., Bishop,S.M., Phillips,D. and Beeby,A. (1995) Phthalocyanine fluorescence at high concentration: dimers or reabsorption effect? *Photochem. Photobiol.*, **61**, 341–346.

235. Rhys Williams,A.T., Winfield,S.A. and Miller,J.N. (1983) Relative fluorescence quantum yields using a computer-controlled luminescence spectrometer. *Analyst*, **108**, 1067–1071.

236. Würth,C., Grabolle,M., Pauli,J., Spieles,M. and Resch-Genger,U. (2013) Relative and absolute determination of fluorescence quantum yields of transparent samples. *Nat. Protoc.*, **8**, 1535–1550.

237. Gaglione,R., Smaldone,G., Di Girolamo,R., Piccoli,R., Pedone,E. and Arciello,A. (2018) Cell milieu significantly affects the fate of AApoAI amyloidogenic variants: predestination or serendipity? *Biochim. Biophys. Acta - Gen. Subj.*, **1862**, 377–384.

238. Lampitella,E., Landi,N., Oliva,R., Gaglione,R., Bosso,A., de Lise,F., Ragucci,S., Arciello,A., Petraccone,L., Pizzo,E., *et al.* (2021) Toxicity and membrane perturbation properties of the ribotoxin-like protein Ageritin. *J. Biochem.*, **170**, 473–482.

239. Yang,H., Metera,K.L. and Sleiman,H.F. (2010) DNA modified with metal complexes: applications in the construction of higher order metal-DNA nanostructures. *Coord. Chem. Rev.*, **254**, 2403–2415.

240. Stulz,E., Clever,G., Shionoya,M. and Mao,C. (2011) DNA in a modern world. *Chem. Soc. Rev.*, **40**, 5633–5635.

241. Clever,G.H., Kaul,C. and Carell,T. (2007) DNA-metal base pairs. *Angew. Chemie - Int. Ed.*, **46**, 6226–6236.

242. Clever,G.H. and Shionoya,M. (2010) Metal-base pairing in DNA. *Coord. Chem. Rev.*, **254**, 2391–2402.

243. Müller,J. (2019) Nucleic acid duplexes with metal-mediated base pairs and their structures. *Coord. Chem. Rev.*, **393**, 37–47.

244. Naskar,S., Guha,R. and Müller,J. (2020) Metal-modified nucleic acids: metal-mediated base pairs, triples, and tetrads. *Angew. Chemie - Int. Ed.*, **59**, 1397–1406.

245. Ihara,T., Ishii,T., Araki,N., Wilson,A.W. and Jyo,A. (2009) Silver ion unusually stabilizes the structure of a parallel-motif DNA triplex. *J. Am. Chem. Soc.*, **131**, 3826–3827.

246. Smith,N.M., Amrane,S., Rosu,F., Gabelic,V. and Mergny,J.L. (2012) Mercury–thymine interaction with a chair type G-quadruplex architecture. *Chem. Commun.*, **48**, 11464–11466.

247. Miyoshi,D., Karimata,H., Wang,Z.M., Koumoto,K. and Sugimoto,N. (2007) Artificial G-wire switch with 2,2′-bipyridine units responsive to divalent metal ions. *J. Am. Chem. Soc.*, **129**, 5919–5925.

248. Engelhard,D.M., Pievo,R. and Clever,G.H. (2013) Reversible stabilization of transition-metal-binding DNA G-quadruplexes. *Angew. Chemie - Int. Ed.*, **52**, 12843–12847.

249. Engelhard,D.M., Nowack,J. and Clever,G.H. (2017) Copper-induced topology switching and thrombin inhibition with telomeric DNA G-quadruplexes. *Angew. Chemie - Int. Ed.*, **56**, 11640–11644.

250. Punt,P.P. and Clever,G.H. (2019) Imidazole-modified G-quadruplex DNA as metal-triggered peroxidase. *Chem. Sci.*, **10**, 2513–2518.

251. Jiang,X., Li,H., Zhou,Q., Wei,Q., Wei,M., Jiang,L., Wang,Z., Peng,Z., Wang,F., Zang,Z., *et al.* (2021) One-step synthesis of SnI2·(DMSO)xadducts for high-performance tin perovskite solar cells. *J. Am. Chem. Soc.*, **143**, 10970–10976.

252. Stratmann,L.M., Kutin,Y., Kasanmascheff,M. and Clever,G.H. (2021) Precise distance measurements in DNA G-quadruplex dimers and sandwich complexes by pulsed dipolar EPR spectroscopy. *Angew. Chemie - Int. Ed.*, **60**, 4939–4947.

253. Martins,A.S., Batista de Carvalho,A.L.M., Lamego,I., Marques,M.P.M. and Gil,A.M. (2020) Cytotoxicity of platinum and palladium chelates against osteosarcoma. *ChemistrySelect*, **5**, 5993–6000.

254. Zhang,C., Xu,C., Gao,X. and Yao,Q. (2022) Platinum-based drugs for cancer therapy and anti-tumor strategies. *Theranostics*, **12**, 2115–2132.

255. Borovansky,J.A.N. and Riley,P.A. (1989) Cytotoxicity of zink in vitro. *Chem.-Biol. Interact.*, **69**, 279–291.

256. Tchounwou,P.B., Newsome,C., Williams,J. and Glass,K. (2008) Copper-induced cytotoxicity and transcriptional activation of stress genes in human liver carcinoma (HepG(2)) cells. *Met. ions Biol. Med.*, **10**, 285–290.

257. Denoyer,D., Clatworthy,S.A.S. and Cater,M.A. (2018) Copper complexes in cancer therapy. *Met. Ions Life Sci.*, **18**, 469–506.

258. Cavaluzzi,M.J. and Borer,P.N. (2004) Revised UV extinction coefficients for nucleoside-5'-monophosphates and unpaired DNA and RNA. *Nucleic Acids Res.*, **32**, 1–9.

259. Yang,H., Antoine,D.J., Andersson,U. and Tracey,K.J. (2013) The many faces of HMGB1: molecular structure-functional activity in inflammation, apoptosis, and chemotaxis. *J. Leukoc. Biol.*, **93**, 865–873.

260. Li Pomi,F., Borgia,F., Custurone,P., Vaccaro,M., Pioggia,G. and Gangemi,S. (2022) Role of HMGB1 in cutaneous melanoma: state of the art. *Int. J. Mol. Sci.*, **23**, 1–18.

261. Zhu,W., Li,J., Zhang,Y., Zhu,Z., Liu,H., Lin,Y., Hu,A., Zhou,J., Ren,H. and Shi,X. (2021) Inhibition of HMGB1 suppresses hepatocellular carcinoma progression via HIPK2-mediated autophagic degradation of ZEB1. *Front. Oncol.*, **11**, 1–14.

262. Jube,S., Rivera,Z., Bianchi,M.E., Powers,A., Wang,E., Pagano,I., Pass,H.I., Gaudino,G., Carbone,M. and Yang,H. (2012) Cancer cell secretion of the DAMP protein HMGB1 supports progression in malignant mesothelioma. *Cancer Res.*, **72**, 3290–3301.

263. Süren,D., Yildirim,M., Demirpençe,Ö., Kaya,V., Alikanoğlu,A.S., Bülbüller,N., Yildiz,M. and Sezer,C. (2014) The role of High Mobility Group Box 1 (HMGB1) in colorectal cancer. *Med. Sci. Monit.*, **20**, 530–537.

264. Di Lorenzo,A., Bolli,E., Ruiu,R., Ferrauto,G., Di Gregorio,E., Avalle,L., Savino,A., Poggio,P., Merighi,I.F., Riccardo,F., *et al.* (2022) Toll-like receptor 2 promotes breast cancer progression and resistance to chemotherapy. *Oncoimmunology*, **11**, 1–18.

265. Zhu,L., Ren,S., Daniels,M.J., Qiu,W., Song,L., You,T., Wang,D. and Wang,Z. (2021) Exogenous HMGB1 promotes the proliferation and metastasis of pancreatic cancer cells. *Front. Med.*, **8**, 1–10.

266. Amato,J., Cerofolini,L., Brancaccio,D., Giuntini,S., Iaccarino,N., Zizza,P., Iachettini,S., Biroccio,A., Novellino,E., Rosato,A., *et al.* (2019) Insights into telomeric G-quadruplex DNA recognition by HMGB1 protein. *Nucleic Acids Res.*, **47**, 9950–9966.

267. Mergny,J.L., Li,J., Lacroix,L., Amrane,S. and Chaires,J.B. (2005) Thermal difference spectra: a specific signature for nucleic acid structures. *Nucleic Acids Res.*, **33**, 1–6.

268. Małgowska,M., Gudanis,D., Teubert,A., Dominiak,G. and Gdaniec,Z. (2012) How to study G-quadruplex structures. *J. Biotechnol. Comput. Biol. Bionanotechnol.*, **93**, 381–390.

269. Mergny,J.L. and Lacroix,L. (2009) UV melting of G-quadruplexes. *Curr. Protoc. Nucleic Acid Chem.*, **17**, 1–15.

270. Lim,K.W., Ng,V.C.M., Martín-Pintado,N., Heddi,B. and Phan,A.T. (2013) Structure of the human telomere in Na+ solution: an antiparallel (2+2) G-quadruplex scaffold reveals additional diversity. *Nucleic Acids Res.*, **41**, 10556–10562.

271. Palumbo,R., Sampaolesi,M., De Marchis,F., Tonlorenzi,R., Colombetti,S., Mondino,A., Cossu,G. and Bianchi,M.E. (2004) Extracellular HMGB1, a signal of tissue damage, induces mesoangioblast migration and proliferation. *J. Cell Biol.*, **164**, 441–449.

272. Justus,C.R., Leffler,N., Ruiz-Echevarria,M. and Yang,L. V. (2014) In vitro cell migration and invasion assays. *J. Vis. Exp.*, **88**, 1–8.

Other projects in the context of my PhD course

During my PhD I also worked at other parallel projects, carried out in my research group, aimed at the identification of effective natural or synthetic ligands selectively targeting the G-quadruplex structures, most commonly found in human telomeres and oncogenes, as potential drugs in anticancer therapies.
These pieces of research led to the publication of the following papers, of which I am co-author:

- Platella,C., Gaglione,R., **Napolitano,E.**, Arciello,A., Pirota,V., Doria,F., Musumeci,D. and Montesarchio,D. (2021) DNA binding mode analysis of a core-extended naphthalene diimide as a conformation-sensitive fluorescent probe of G-quadruplex structures. *Int. J. Mol. Sci.*, **22**, 1–20. https://doi.org/10.3390/ijms221910624
- Platella,C., Mazzini,S., **Napolitano,E.**, Mattio,L.M., Beretta,G.L., Zaffaroni,N., Pinto,A. Montesarchio,D. and Dallavalle,S. (2021) Plant-derived stilbenoids as DNA-binding agents: from monomers to dimers. *Chem. - A Eur. J.*, **27**, 8832–8845. https://doi.org/10.1002/chem.202101229

I also focused on preparing several reviews offering an updated literature state-of-the-art on different key-topics of my PhD project. This activity was carried out especially during the lockdown months, due to the COVID-19 pandemic in 2020, in which no - or very limited - access to the laboratories was allowed. This literature research led to the publication of the following papers, of which I am co-author:

- Criscuolo,A., **Napolitano,E.**, Riccardi,C., Musumeci,D., Platella,C. and Montesarchio,D. (2022) Insights into the small molecule targeting of biologically relevant G-quadruplexes: an overview of NMR and crystal structures. *Pharmaceutics*, **14**, 1–33. https://doi.org/10.3390/pharmaceutics14112361
- Platella,C., **Napolitano,E.**, Riccardi,C., Musumeci,D. and Montesarchio,D. (2022) Affinity chromatography-based assays for the screening of potential ligands selective for G-quadruplex structures. *ChemistryOpen*, **11**, 1–18. https://doi.org/10.1002/open.202200090
- Scognamiglio,P.L., Platella,C., **Napolitano,E.**, Musumeci,D. and Roviello,G.N. (2021) From prebiotic chemistry to supramolecular biomedical materials: Exploring the properties of self-assembling nucleobase-containing peptides. *Molecules*, **26**, 1–16. https://doi.org/10.3390/molecules26123558
- Platella,C., **Napolitano,E.**, Riccardi,C., Musumeci,D. and Montesarchio,D. (2021) Disentangling the structure–activity relationships of naphthalene diimides as anticancer G-quadruplex-targeting drugs. *J. Med. Chem.*, **64**, 3578–3603. https://doi.org/10.1021/acs.jmedchem.1c00125

- Riccardi,C., **Napolitano,E.**, Musumeci,D. and Montesarchio,D. (2020) Dimeric and multimeric DNA aptamers for highly effective protein recognition. *Molecules*, **25**, 7–15. https://doi.org/10.3390/molecules25225227
- Riccardi,C., **Napolitano,E.**, Platella,C., Musumeci,D. and Montesarchio,D. (2020) G-quadruplex-based aptamers targeting human thrombin: discovery, chemical modifications and antithrombotic effects. *Pharmacol. Ther.*, **217**, 1–52. https://doi.org/10.1016/j.pharmthera.2020.107649
- Riccardi,C., **Napolitano,E.**, Platella,C., Musumeci,D. and Montesarchio,D. (2020) Anti-VEGF DNA-based aptamers in cancer therapeutics and diagnostics. *Med. Res. Rev.*, **41**, 464–506. https://doi.org/10.1002/med.21737.

List of the oral communications and posters presented to conferences and PhD schools

- **E. Napolitano,** A. Criscuolo, C. Riccardi, C. Esposito, D. Musumeci, D. Montesarchio. **G-quadruplex-forming aptamers for HMGB1 inhibition in cancer therapy.** INTERACTION WINS 2023. Virtual meeting, February 20-24, 2023. Abstract selected for an **oral presentation**.
- **E. Napolitano,** C. Riccardi, D. Musumeci, F. Doria, R. Gaglione, A. Arciello, D. Montesarchio. **Selectively lighting-up dimeric G-quadruplex forming aptamers with a thiazole orange derivative for efficient $VEGF_{165}$ targeting.** Nucleic Acid Secondary Structures G4s and Beyond. Webinar series 2022-VIII, February 09, 2023. Abstract selected for an **oral presentation**.
- **E. Napolitano,** A. Criscuolo, C. Riccardi, C. Esposito, D. Musumeci, D. Montesarchio. **Novel anti-HMGB1 aptamers as potential drugs in anti-inflammatory and cancer therapies.** The 8th International Electronic Conference on Medicinal Chemistry. Virtual meeting, November 01-30, 2022. Abstract selected for an **oral presentation**.
- **E. Napolitano,** C. Riccardi, D. Musumeci, F. Doria, R. Gaglione, A. Arciello, D. Montesarchio. **Selectively lighting-up dimeric G-quadruplex forming aptamers with a thiazole orange derivative for efficient $VEGF_{165}$ targeting.** XXIV International Round Table on Nucleosides, Nucleotides and Nucleic Acids. Stockholm, Sweden, August 28-31, 2022. Abstract selected for a **poster presentation**.
- **E. Napolitano,** C. Riccardi, D. Musumeci, F. Doria, R. Gaglione, A. Arciello, D. Montesarchio. **A fluorescent probe selectively lightning up upon binding with dimeric G-quadruplex forming aptamers**. VIII International Meeting on Quadruplex Nucleic Acids. Marienbad, Czech Republic, June 27-Luly 01, 2022. Abstract selected for a **poster presentation**.
- **E. Napolitano,** C. Riccardi, D. Musumeci, F. Doria, R. Gaglione, A. Arciello, D. Montesarchio. **Cyanine-bound G-quadruplex forming aptamers for theranostics**. XLVI "A. Corbella" International Summer School of Organic Synthesis. Gargnano (BS) (Italy), June 12-16, 2022. Abstract selected for an **oral presentation**.
- **E. Napolitano,** C. Riccardi, D. Musumeci, F. Doria, R. Gaglione, A. Arciello, D. Montesarchio. **An aptamer-based sandwich system for VEGF fluorescence detection.** INTERACTION WINS 2021. Virtual meeting, November 23-26, 2021. Abstract selected for both a poster and an **oral presentation**.
- **E. Napolitano**, C. Riccardi, D. Musumeci, F. Doria, R. Gaglione, A. Arciello, D. Montesarchio. **A VEGF-targeting aptamer labelled with a fluorescence light-up probe for diagnostics and theranostics.** XVII National Congress of the Italian Chemical Society (SCI). Virtual meeting, September 14-23, 2021. Abstract selected for a **poster presentation**.
- **E. Napolitano**, C. Riccardi, D. Musumeci, F. Doria, R. Gaglione, A. Arciello, D. Montesarchio. **A selective fluorescent light-up aptameric system for diagnostics and theranostics.** CINMPIS Days, Messina (Italy), September 07-08, 2021. Abstract selected for an **oral presentation**.

- **E. Napolitano**, C. Platella, S. Mazzini, L. M. Mattio, G. L. Beretta, N. Zaffaroni, A. Pinto, D. Montesarchio, S. Dallavalle. **Plant-derived stilbenoids as DNA-binding agents: from monomers to dimers.** XLV "A. Corbella" International Summer School of Organic Synthesis. Gargnano (BS) (Italy), June 14-17, 2021. Abstract selected for a **poster presentation**.

Full list of publications

- **Napolitano, E.**, Criscuolo, A., Riccardi, C., Esposito, C.L., Roviello, G.N., Montesarchio and D., Musumeci. G-quadruplex forming aptamers for efficient inhibition of HMGB1 pathological activity. *Manuscript in preparation.*

Abstract
High-Mobility Group Box 1 (HMGB1) is an abundant, highly conserved, non-histone nuclear protein present in almost all eukaryotic cell. In inflammatory conditions, HMGB1 is actively secreted from immune cells in the extracellular matrix, where it behaves as a proinflammatory cytokine. Once released, it can bind to cell-surface receptors, such as the Receptor for Advanced Glycation End products (RAGE) and Toll-Like Receptors (TLR) 2, 4 and 9, and mediate various cellular responses, including the induction of cell migration/proliferation and the release of other proinflammatory cytokines. Moreover, HMGB1 is able to contribute to the pathogenesis of various chronic inflammatory and autoimmune diseases as well as of cancer. Given the multiple roles of HMGB1 in these pathologies, identification of inhibitors of this protein is of considerable clinical interest. We here identified novel G-quadruplex (G4) forming aptamers as potential HMGB1 inhibitors. Using SELEX technology, we selected 14 G4-forming DNA sequences from a properly designed G-rich oligonucleotide library. These aptamers have been fully characterized in a biologically relevant buffer using several biophysical techniques to determine their preferred conformation as well as their thermal and enzymatic stability. Moreover, we evaluated the interaction between these aptamers and HMGB1, as well as their ability to inhibit HMGB1-induced migration in cancer cells so to identify the best candidates for future *in vivo* assays aimed at repressing the pathological functions induced by the target protein.

- **Napolitano,E.**, Riccardi,C., Gaglione,R., Arciello,A., Pirota,V., Triveri,A., Doria,F., Musumeci,D. and Montesarchio,D. (2023) Selective light-up of dimeric G-quadruplex forming aptamers for efficient VEGF165 detection. *Int. J. Biol. Macromol.*, **224**, 344–357. https://doi.org/10.1016/j.ijbiomac.2022.10.128

Abstract
To develop efficient anticancer theranostic systems, we studied the interaction between a cyanine dye, analogue of thiazole orange (named CyOH), and two G-quadruplex-forming aptamers, V7t1 and 3R02, recognizing the Vascular Endothelial Growth Factor 165 (VEGF165) - an angiogenic protein overexpressed in cancer cells, responsible for the rapid growth and metastases of solid tumours. We demonstrated, by exploiting different biophysical techniques - *i.e.* gel electrophoresis, circular dichroism (CD), UV–vis and fluorescence spectroscopy - that this cyanine interacted with both aptamers giving a marked fluorescence light-up only when bound to their dimeric forms. Interestingly, both oligonucleotides recognized VEGF165 with higher affinity when adopting dimeric G-quadruplexes, largely prevalent over their monomeric forms in pseudo-physiological conditions. Notably, the fluorescence light-up produced by the probe was maintained

when the dimeric aptamer-CyOH complexes bound to the target protein. These complexes, tested on MCF-7 cancer cells using non-tumorigenic MCF-10A cells as control, were effectively internalized in cells and colocalized with a fluorescently-labelled anti-VEGF-A antibody, allowing both recognition and detection of the target. Our experiments showed that the studied systems are promising tools for anticancer theranostic strategies, combining the therapeutic potential of the G4-forming anti-VEGF aptamers with the diagnostic efficacy of the cyanine selective fluorescence light-up.

- Criscuolo,A., **Napolitano,E.**, Riccardi,C., Musumeci,D., Platella,C. and Montesarchio,D. (2022) Insights into the small molecule targeting of biologically relevant G-quadruplexes: an overview of NMR and crystal structures. *Pharmaceutics*, **14**, 1–33. https://doi.org/10.3390/pharmaceutics14112361

Abstract
G-quadruplexes turned out to be important targets for the development of novel targeted anticancer/antiviral therapies. More than 3000 G-quadruplex small-molecule ligands have been described, with most of them exerting anticancer/antiviral activity by inducing telomeric damage and/or altering oncogene or viral gene expression in cancer cells and viruses, respectively. For some ligands, in-depth NMR and/or crystallographic studies were performed, providing detailed knowledge on their interactions with diverse G-quadruplex targets. Here, the PDB-deposited NMR and crystal structures of the complexes between telomeric, oncogenic or viral G-quadruplexes and small-molecule ligands, of both organic and metal-organic nature, have been summarized and described based on the G-quadruplex target, from telomeric DNA and RNA G-quadruplexes to DNA oncogenic G-quadruplexes, and finally to RNA viral G-quadruplexes. An overview of the structural details of these complexes is here provided to guide the design of novel ligands targeting more efficiently and selectively cancer- and virus-related G-quadruplex structures.

- Platella,C., **Napolitano,E.**, Riccardi,C., Musumeci,D. and Montesarchio,D. (2022) Affinity chromatography-based assays for the screening of potential ligands selective for G-quadruplex structures. *ChemistryOpen*, **11**, 1–18. https://doi.org/10.1002/open.202200090

Abstract
DNA G-quadruplexes (G4s) are key structures for the develop- ment of targeted anticancer therapies. In this context, ligands selectively interacting with G4s can represent valuable anti- cancer drugs. Aiming at speeding up the identification of G4- targeting synthetic or natural compounds, we developed an affinity chromatography-based assay, named G-quadruplex on Oligo Affinity Support (G4-OAS), by synthesizing G4-forming sequences on commercially available polystyrene OAS. Then, due to unspecific binding of several hydrophobic ligands on nude OAS, we moved to Controlled Pore Glass (CPG). We thus conceived an ad hoc functionalized, universal support on which both the on-support elongation and deprotection of the G4-forming oligonucleotides can be performed, along with the successive affinity chromatography-based assay, renamed as

G- quadruplex on Controlled Pore Glass (G4-CPG) assay. Here we describe these assays and their applications to the screening of several libraries of chemically different putative G4 ligands. Finally, ongoing studies and outlook of our G4-CPG assay are reported.

- Platella,C., Gaglione,R., **Napolitano,E.**, Arciello,A., Pirota,V., Doria,F., Musumeci,D. and Montesarchio,D. (2021) DNA binding mode analysis of a core-extended naphthalene diimide as a conformation-sensitive fluorescent probe of G-quadruplex structures. *Int. J. Mol. Sci.*, **22**, 1–20. https://doi.org/10.3390/ijms221910624

  Abstract
  G-quadruplex existence was proved in cells by using both antibodies and small molecule fluorescent probes. However, the G-quadruplex probes designed thus far are structure- but not conformation-specific. Recently, a core-extended naphthalene diimide (**c_{ex}-NDI**) was designed and found to provide fluorescent signals of markedly different intensities when bound to G-quadruplexes of different conformations or duplexes. Aiming at evaluating how the fluorescence behaviour of this compound is associated with specific binding modes to the different DNA targets, **c_{ex}-NDI** was here studied in its interaction with hybrid G-quadruplex, parallel G-quadruplex, and B-DNA duplex models by biophysical techniques, molecular docking, and biological assays. **c_{ex}-NDI** showed different binding modes associated with different amounts of stacking interactions with the three DNA targets. The preferential binding sites were the groove, outer quartet, or intercalative site of the hybrid G-quadruplex, parallel G-quadruplex, and B-DNA duplex, respectively. Interestingly, our data show that the fluorescence intensity of DNA-bound **c_{ex}-NDI** correlates with the amount of stacking interactions formed by the ligand with each DNA target, thus providing the rationale behind the conformation-sensitive properties of **c_{ex}-NDI** and supporting its use as a fluorescent probe of G-quadruplex structures. Notably, biological assays proved that **c_{ex}-NDI** mainly localizes in the G-quadruplex-rich nuclei of cancer cells.

- Platella,C., Mazzini,S., **Napolitano,E.**, Mattio,L.M., Beretta,G.L., Zaffaroni,N., Pinto,A. Montesarchio,D. and Dallavalle,S. (2021) Plant-derived stilbenoids as DNA-binding agents: from monomers to dimers. *Chem. - A Eur. J.*, **27**, 8832–8845. https://doi.org/10.1002/chem.202101229

  Abstract
  Stilbenoids are natural compounds endowed with several biological activities, including cardioprotection and cancer prevention. Among them, (±)-*trans*-δ-viniferin, deriv- ing from *trans*-resveratrol dimerization, was investigated in its ability to target DNA duplex and G-quadruplex structures by exploiting NMR spectroscopy, circular dichroism, fluorescence spectroscopy and molecular docking. (±)-*trans*-δ-Viniferin proved to bind both the minor and major grooves of duplexes, whereas it bound the 3'- and 5'-ends of a G- quadruplex by stacking on the outer quartets, accompanied by rearrangement of flanking residues. Specifically, (±)-*trans*- δ-viniferin demonstrated higher affinity for the

investigated DNA targets than its monomeric counterpart. Additionally, the methoxylated derivatives of (±)-*trans*-δ-viniferin and *trans*-resveratrol, i. e. (±)-pterostilbene-*trans*-dihydrodimer and *trans*-pterostilbene, respectively, were evaluated, reveal- ing similar binding modes, affinities and stoichiometries with the DNA targets as their parent analogues. All tested compounds were cytotoxic at μM concentration on several cancer cell lines, showing DNA damaging activity consistent with their ability to tightly interact with duplex and G- quadruplex structures.

- Scognamiglio,P.L., Platella,C., **Napolitano,E.**, Musumeci,D. and Roviello,G.N. (2021) From prebiotic chemistry to supramolecular biomedical materials: Exploring the properties of self-assembling nucleobase-containing peptides. *Molecules*, **26**, 1–16. https://doi.org/10.3390/molecules26123558

Abstract
Peptides and their synthetic analogues are a class of molecules with enormous relevance as therapeutics for their ability to interact with biomacromolecules like nucleic acids and proteins, potentially interfering with biological pathways often involved in the onset and progression of pathologies of high social impact. Nucleobase-bearing peptides (nucleopeptides) and pseudopeptides (PNAs) offer further interesting possibilities related to their nucleobase-decorated nature for diagnostic and therapeutic applications, thanks to their reported ability to target complementary DNA and RNA strands. In addition, these chimeric compounds are endowed with intriguing self-assembling properties, which are at the heart of their investigation as self-replicating materials in prebiotic chemistry, as well as their application as constituents of innovative drug delivery systems and, more generally, as novel nanomaterials to be employed in biomedicine. Herein we describe the properties of nucleopeptides, PNAs and related supramolecular systems, and summarize some of the most relevant applications of these systems.

- Platella,C., **Napolitano,E.**, Riccardi,C., Musumeci,D. and Montesarchio,D. (2021) Disentangling the structure–activity relationships of naphthalene diimides as anticancer G-quadruplex-targeting drugs. *J. Med. Chem.*, **64**, 3578–3603. https://doi.org/10.1021/acs.jmedchem.1c00125

Abstract
In the context of developing efficient anticancer therapies aimed at eradicating any sort of tumors, G-quadruplexes represent excellent targets. Small molecules able to interact with G- quadruplexes can interfere with cell pathways specific of tumors and common to all cancers. Naphthalene diimides (NDIs) are among the most promising, putative anticancer G-quadruplex- targeting drugs, due to their ability to simultaneously target multiple G-quadruplexes and their strong, selective *in vitro* and *in vivo* anticancer activity. Here, all the available biophysical, biological, and structural data concerning NDIs targeting G-quadruplexes were systematically analyzed. Structure−activity correlations were obtained by analyzing biophysical data of their interactions with G-quadruplex targets and control duplex structures, in parallel to biological data concerning the antiproliferative activity of

NDIs on cancer and normal cells. In addition, NDI binding modes to G-quadruplexes were discussed in consideration of the structures and properties of NDIs by in-depth analysis of the available structural models of G-quadruplex/NDI complexes.

- Riccardi,C., **Napolitano,E.**, Musumeci,D. and Montesarchio,D. (2020) Dimeric and multimeric DNA aptamers for highly effective protein recognition. *Molecules*, **25**, 7–15. https://doi.org/10.3390/molecules25225227

Abstract

Multivalent interactions frequently occur in biological systems and typically provide higher binding affinity and selectivity in target recognition than when only monovalent interactions are operative. Thus, taking inspiration by nature, bivalent or multivalent nucleic acid aptamers recognizing a specific biological target have been extensively studied in the last decades. Indeed, oligonucleotide-based aptamers are suitable building blocks for the development of highly efficient multivalent systems since they can be easily modified and assembled exploiting proper connecting linkers of different nature. Thus, substantial research efforts have been put in the construction of dimeric/multimeric versions of effective aptamers with various degrees of success in target binding affinity or therapeutic activity enhancement. The present review summarizes recent advances in the design and development of dimeric and multimeric DNA-based aptamers, including those forming G-quadruplex (G4) structures, recognizing different key proteins in relevant pathological processes. Most of the designed constructs have shown improved performance in terms of binding affinity or therapeutic activity as anti-inflammatory, antiviral, anticoagulant, and anticancer agents and their number is certainly bound to grow in the next future.

- Riccardi,C., **Napolitano,E.**, Platella,C., Musumeci,D. and Montesarchio,D. (2020) G-quadruplex-based aptamers targeting human thrombin: discovery, chemical modifications and antithrombotic effects. *Pharmacol. Ther.*, **217**, 1–52. https://doi.org/10.1016/j.pharmthera.2020.107649

Abstract

First studies on thrombin-inhibiting DNA aptamers were reported in 1992, and since then a large number of an- ticoagulant aptamers has been discovered. TBA – also named HD1, a 15-mer G-quadruplex (G4)-forming oligo- nucleotide – is the best characterized thrombin binding aptamer, able to specifically recognize the protein exosite I, thus inhibiting the conversion of soluble fibrinogen into insoluble fibrin strands. Unmodified nucleic acid-based aptamers, in general, and TBA in particular, exhibit limited pharmacokinetic properties and are rapidly degraded *in vivo* by nucleases. In order to improve the biological performance of aptamers, a widely investigated strategy is the introduction of chemical modifications in their backbone at the level of the nucleobases, sugar moieties or phosphodiester linkages. Besides TBA, also other thrombin binding aptamers, able to adopt a well-defined G4 structure, *e.g.* mixed duplex/quadruplex sequences, as well as homo- and hetero-bivalent constructs, have been identified and

optimized. Considering the growing need of new efficient anticoagulant agents associated with the strong therapeutic potential of these thrombin inhibitors, the research on thrombin binding aptamers is still a very hot and intriguing field. Herein, we comprehensively described the state-of-the-art knowledge on the DNA-based aptamers targeting thrombin, especially focusing on the optimized analogues obtained by chemically modifying the oligonucleotide backbone, and their biological performances in therapeutic applications.

- Riccardi,C., **Napolitano,E.**, Platella,C., Musumeci,D. and Montesarchio,D. (2020) Anti-VEGF DNA-based aptamers in cancer therapeutics and diagnostics. *Med. Res. Rev.*, **41**, 464–506. https://doi.org/10.1002/med.21737

Abstract

The vascular endothelial growth factor (VEGF) family and its receptors play fundamental roles not only in physiological but also in pathological angiogenesis, characteristic of cancer progression. Aiming at finding putative treatments for several malignancies, various small molecules, anti- bodies, or protein-based drugs have been evaluated *in vitro* and *in vivo* as VEGF inhibitors, providing efficient agents approved for clinical use. Due to the high clinical importance of VEGF, also a great number of anti-VEGF nucleic acid-based aptamers—that is, oligonucleotides able to bind with high affinity and specificity a selected biological target—have been developed as promising agents in anticancer strategies. Notable research efforts have been made in optimization processes of the identified aptamers, searching for increased target affinity and/or bioactivity by exploring structural analogues of the lead compounds. This review is focused on recent studies devoted to the development of DNA-based aptamers designed to target VEGF. Their therapeutic potential as well as their significance in the construction of highly selective biosensors is here discussed.